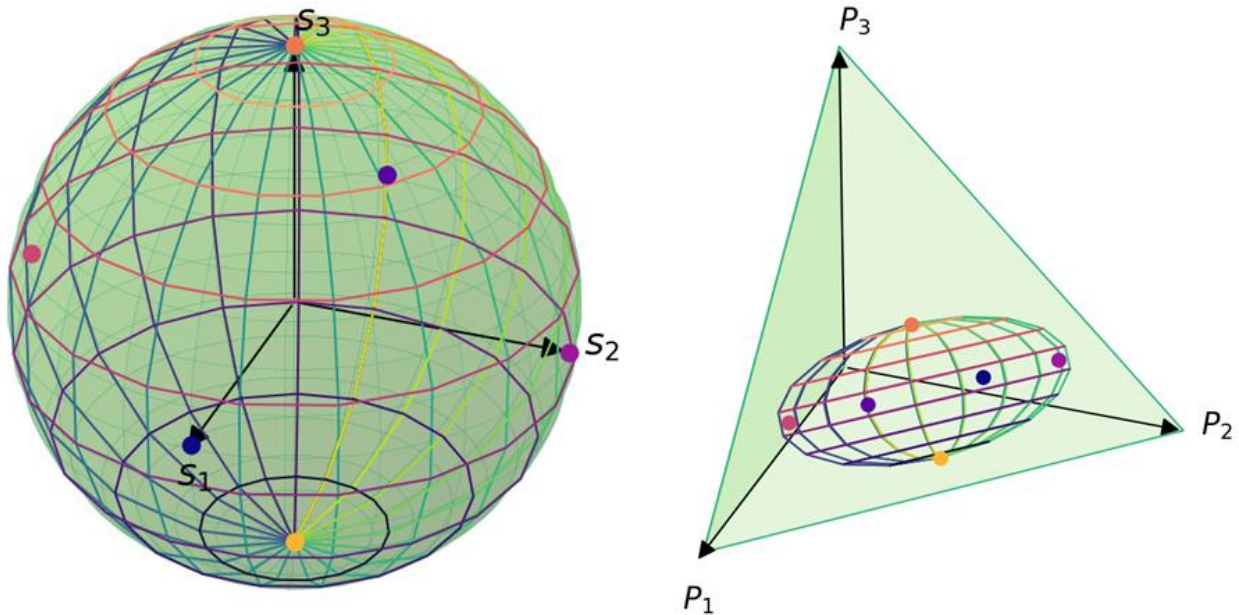


Polarization Multiplexed Photonic Integrated Circuits for 100 Gbit/s and Beyond



vorgelegt von
M.Sc. Moritz Friedrich Baier
geboren in Mannheim, Deutschland

Von der Fakultät II - Mathematik und Naturwissenschaften
der Technischen Universität Berlin
zur Erlangung des akademischen Grades

Doktor der Ingenieurwissenschaften
- Dr.-Ing. -
genehmigte Dissertation

Promotionsausschuss:

Vorsitzende: Prof. Dr. Kathy Lüdge
1. Gutachter: Prof. Dr. Martin Schell
2. Gutachter: Prof. Dr. Kevin Williams

Tag der wissenschaftlichen Aussprache: 23. Juli 2018

Berlin 2018

"Science is imagination in a straitjacket." - Richard P. Feynman

"Der Mensch spielt nur, wo er in voller Bedeutung des Wortes Mensch ist, und er ist nur da ganz Mensch, wo er spielt." - Friedrich Schiller

"It never gets easier, you just go faster." Greg LeMond

Abstract

In this thesis, a fully integrated dual-polarization (DP) optical transmitter is proposed, developed and demonstrated. The transmitter proposed in this work consists of two key building blocks: a polarization rotator (PR) and two electro-absorption modulators (EAM), laid out in a serial configuration. Furthermore, a laser source is monolithically integrated. All devices are realized in the semiconducting material system of indium phosphide (InP) and its related quaternary alloys (InGaAsP). The technology used for fabrication is referred to as generic, meaning that it is not intended for fabrication of a specific device but rather to enable as many different applications as possible, much like modern silicon processes in electronics.

The thesis begins with the theoretical implications of optical polarization in integrated waveguides. Known principles on how to make integrated polarization rotating devices are discussed and it is shown that they prove to be too sensitive on typical fabrication tolerances. It is shown that the Jones formalism, originally intended for free space optics, can be used to describe integrated waveguides on the micro-scale. Based on this formalism, an optimization technique is derived that lowers the sensitivity to fabrication errors by 25% and brings down theoretical optical losses from 0.8 dB to 0.1 dB. The same approach is used to design devices that rotate polarization not by 90° , but by 45° . Next, new device structures are proposed for polarization resolved reception and transmission of optical signals. The iSTOMP (integrated STOKes MaPper) uses an interferometric structure loaded with several PRs and allows the complete characterization of the polarization ellipse of incoming signals. The mathematical groundwork is given as well as a geometric way of understanding the device. For data transmission, a serial DP EAM design is proposed. It consists of two EAMs interconnected by a single 90° PR. The DP EAM makes use of the fact that EAMs in InP typically only modulate one polarization, so that the cascade of devices enables DP modulation. The EAMs make use of multi-quantum well (MQW) layers, thin sheets of semiconductor that break the symmetry of the InP crystal. The electronic and optoelectronic effects in MQW-based EAMs are studied to verify that the proposed DP EAM can indeed be demonstrated with good performance. In particular, a polarization resolved model of the dominating light-matter interaction, the quantum-confined Stark effect (QCSE), is given. Finally, a design of an EAM is derived. System-level simulations of the DP EAM are carried out to conclude the theoretical part of the thesis. It is shown that for an implementation penalty below 1 dB, the PR has to have an extinction ratio above 16 dB.

To carry out detailed analysis of the fabricated devices, a new approach for polarization resolved measurements is given. It makes use of the Müller/Stokes formalism and is implemented in an experimental setup. This setup uses only optical fibers and no free space optics, thus it is suitable for automated measurements of many devices. The polarization in this setup is shown to be accurate within 2° across the entire Poincaré sphere and C-band. This setup allows a fast and stable characterization of the fabricated PRs, EAMs and the DP EAM. It is shown how the polarimetric measurement equation can be solved easily in the fiber-based setup and how decomposition of Müller matrices can give insights into the

various devices. It is shown further that for devices with strong polarization dependence, phase effects like the chirp parameter can be deduced from Müller measurements. Fabricated PRs with polarization extinction ratios of up to 25 dB (rotation within $\pm 4^\circ$ around 90°) and losses below 1 dB are achieved. The fabricated EAMs show a very strong polarization dependence of over 20 dB, just like theory suggests. In the first fabricated generation, electro-optic bandwidths of up to 17 GHz are measured. These devices are capable of transmitting 39 Gbit/s. The new DP EAM is characterized and it is shown that it can indeed modulate two distinct states of polarization. In a system experiment using 28 GBaud PAM-4 signaling, error-free transmission of 100 Gbit/s is shown over 80 km of fiber. Finally, a fully integrated transmitter is demonstrated, comprising a distributed feedback (DFB) laser, a 45° PR and the aforementioned DP EAM. This is the first demonstration of a monolithically integrated transmitter PIC capable of polarization multiplexing in InP.

Zusammenfassung

In der vorliegenden Arbeit wird ein voll integrierter, optisch doppel polarisierter Transmitter vorgeschlagen, entwickelt und demonstriert. Der vorgeschlagene Transmitter besteht aus zwei grundlegenden Bausteinen: einem Polarisationsdreher (PR) und zwei Elektroabsorptionsmodulatoren (EAM), die in einer seriellen Konfiguration aneinandergereiht sind. Weiterhin ist eine Laserquelle monolithisch integriert. Alle Komponenten sind im Halbleitermaterialsystem Indiumphosphid (InP) und seinen verwandten quaternären Verbundmaterialien (InGaAsP) verwirklicht. Die zur Umsetzung genutzte Technologie wird als generisch bezeichnet, da sie nicht für ein spezielles Bauelement, sondern vielmehr für die Verwirklichung einer größtmöglichen Anzahl an verschiedenen Bauelementen vorgesehen ist. Sie ist damit der modernen Siliziumtechnologie für elektronische Komponenten wesensverwandt.

Die Arbeit beginnt mit der Diskussion der theoretischen Aspekte der optischen Polarisation in integrierten Wellenleitern. Bekannte Prinzipien zur Realisierung integrierter polarisationsdrehender Komponenten werden ausgeführt um zu zeigen, dass sie für typische Fertigungstoleranzen zu kritisch sind. Es wird gezeigt dass der Jones-Formalismus, der ursprünglich für die Freistrahloptik konzipiert war, auch für die Beschreibung photonisch integrierter Komponenten dienlich sein kann. Mithilfe dieses Formalismus wird eine Optimierungsstrategie abgeleitet, deren Ergebnisse die Empfindlichkeit gegenüber Fertigungstoleranzen um 25% entspannt und die theoretischen optischen Verluste von 0.8 auf 0.1 dB senkt. Dieselbe Strategie wird genutzt um Komponenten zu berechnen, die die optische Polarisation nicht nur um 90° , sondern auch um 45° drehen. Im Weiteren werden photonisch integrierte Schaltkreise (PICs) vorgeschlagen, die den polarisationsaufgelösten Empfang und die Übertragung von optischen Signalen ermöglichen. Der iSTOMP nutzt ein Interferometer, welches mehrere Arme besitzt, die alle mit Polarisationsdrehern bestückt sind. Die aus dem Interferometer austretenden Signale erlauben die vollständige Bestimmung der Polarisationsellipse des eintretenden Signals. Es wird die mathematische Beschreibung hergeleitet und außerdem eine geometrische Veranschaulichung gegeben. Zur Übertragung polarisationsmultiplexer Signale wird schließlich ein neuer doppel polarisierter EAM (DP EAM) vorgeschlagen. Der DP EAM besteht aus zwei EAMs, die mit einem 90° PR verbunden sind. Das Funktionsprinzip beruht auf der Tatsache, dass EAMs auf InP-Basis typischerweise nur die TE Polarisation modulieren, so dass die EAM-PR-EAM Kaskade einen doppel polarisierten Modulator bildet. Die EAMs basieren auf einer aktiven Schicht aus mehreren Quantentöpfen (MQW), also einer Abfolge aus dünnen Halbleiterschichten die die Symmetrie des InP Kristalls brechen. Die elektronischen und opto-elektronischen Eigenschaften von MQW-basierten EAMs werden untersucht um die Realisierbarkeit des angestrebten DP EAM Konzepts zu bestätigen. Insbesondere wird ein polarisationsaufgelöstes Modell der wichtigen Wechselwirkung zwischen Licht und Materie in den EAMs gegeben, dem quantum-confined Stark Effekt (QCSE). Schließlich wird der EAM selbst entworfen. Zum Abschluss des theoretischen Teils der Arbeit werden Systemsimulationen des DP EAMs durchgeführt. Es wird gezeigt, dass für eine

Implementierungseinbuße des DP EAM von weniger als 1 dB der PR ein Auslöschverhältnis von über 16 dB haben muss.

Zur detaillierten Analyse der hergestellten Bauelemente wird ein neuer Ansatz für polarisationsaufgelöste Messungen aufgezeigt. Der Ansatz beruht auf dem Müller/Stokes Formalismus und wird in einem experimentellen Messaufbau verwirklicht. Der Messaufbau basiert dabei vollständig auf einmodigen Glasfasern und verzichtet für die Bauteilcharakterisierung vollständig auf Freistrahloptik. Die optische Polarisation kann in diesem Aufbau mit einer Genauigkeit von 2° über die gesamte Poincaré Sphäre und das gesamte C-Band eingestellt und ausgelesen werden. Es wird eine schnelle und stabile Vermessung der hergestellten PRs, EAMs und des DP EAM ermöglicht. Dafür wird gezeigt, wie die polarimetrische Messgleichung gelöst werden kann und wie die Zerlegung der gewonnenen Müller Matrizen auf die verschiedenen Bauelementeigenschaften schließen lässt. So kann im Grenzfall der starken Polarisationsabhängigkeit zum Beispiel sogar der Chirp Parameter durch Müller Messungen gewonnen werden. Die hergestellten Polarisationsdreher weisen Auslöschverhältnisse von bis zu 25 dB (äquivalent zu $\pm 4^\circ$ Genauigkeit um 90°) und Einfügeverluste von unter 1 dB auf. Die hergestellten EAMs zeigen in Übereinstimmung mit theoretischen Überlegungen eine starke Polarisationsabhängigkeit von über 20 dB. Die erste Generation von EAMs weist elektrooptische Bandbreiten von bis zu 17 GHz auf. Mit ihnen wird Datenübertragung von 39 Gbit/s gezeigt. Schließlich wird anhand des hergestellten DP EAM experimentell gezeigt, dass er die unabhängige Modulation von zwei getrennten Polarisationszuständen erlaubt. In einem Systemexperiment wird er verwendet um mit 28 GBaud PAM-4 Signalen eine fehlerfreie Datenübertragung von 100 Gbit/s über 80 km Glasfaser zu zeigen. Schließlich wird ein vollständig monolithisch integrierter Transmitter gezeigt, der aus einem DFB Laser, einem 45° PR und dem bereits erwähnten DP EAM besteht. Damit liegt das erste vollintegrierte Transmitter PIC für Polarisationsmultiplexing in InP vor.

Table of Contents

1	Introduction.....	10
1.1	Motivation.....	10
1.2	Objectives.....	11
1.3	Structure of the Thesis	11
2	Polarization in Photonic Integrated Circuits.....	12
2.1	Optical Anisotropy and Birefringence	12
2.2	The Jones Formalism	13
2.2.1	Jones Vector and Polarization Ellipse	13
2.2.2	Jones Matrix.....	16
2.3	The Müller/Stokes Formalism.....	16
2.3.1	Stokes Vectors and the Poincaré Sphere	16
2.3.2	Distance on a Sphere.....	18
2.3.3	Müller Matrices	19
2.4	Optical Waveguides	22
2.4.1	Analogy between plane waves and guided waves.....	22
2.4.2	Symmetric Waveguides	22
2.4.3	Asymmetric Waveguides.....	23
2.5	Integrated Polarization Converters.....	26
2.5.1	Basic Principle and Single Section Device.....	26
2.5.2	Two Section Device	27
2.5.3	Transitions between Waveguides.....	28
2.5.4	Design Optimization	32
2.5.5	Discussion of Final Design.....	38
2.5.6	45° Polarization Rotators	39
3	Transmitters and Receivers for PDM	41
3.1	iSTOMP: Stokes Space Receiver	41
3.1.1	Mathematical Description	41
3.1.2	Numerical Analysis	43
3.1.3	Geometrical Analysis	44
3.2	Dual Polarization Electro-Absorption Modulators.....	47
3.2.1	A New DP Modulation Scheme.....	47

3.2.2	Theoretical Background of EAMs	48
3.2.3	EAM Design	58
3.2.4	DP EAM Simulations.....	64
4	Experiments.....	68
4.1	Experimental Methodology – Fiber Based Stokes Measurements.....	68
4.1.1	Experimental Setup	68
4.1.2	Solving the Polarimetric Measurement Equation.....	76
4.1.3	Müller Matrix Decomposition.....	78
4.1.4	Software Implementation	79
4.2	Polarization Rotator Results.....	80
4.2.1	90° Polarization Rotators	81
4.2.2	45° Polarization Rotators	84
4.3	EAM Results	85
4.3.1	DC Measurements.....	85
4.3.2	Small Signal Measurements	89
4.3.3	Large Signal Measurements.....	91
4.4	DP EAM Results	92
4.4.1	DC Measurements.....	93
4.4.2	Transmission Experiments.....	94
4.5	DPEML Results	97
4.5.1	DC Measurements.....	98
4.5.2	Large Signal Measurements.....	101
5	Conclusion & Outlook.....	103
5.1	Conclusion	103
5.2	Outlook	103
5.3	Acknowledgements	104
6	Appendices.....	106

1 Introduction

1.1 Motivation

The tremendous technological leaps made by mankind in the 20th century can be traced back to two main innovations: the transistor in 1948 and the laser in 1960 [1], [2]. Within a few decades, the interplay of both lead to the information society as we know it today. Sophisticated lithographic techniques enable mass production of transistor-based devices on a scale that seemed unthinkable before. On the other hand, these devices are capable of generating, processing and storing the gargantuan amount of data that is transmitted through optical fiber links that span the globe. Up to 21 billion transistors are integrated on an area of less than 10 cm² [3] in today's commercially available devices. Integration density still grows exponentially, as was already observed by Moore in 1965 [4]. Global internet traffic in 2016 reached 1.2 ZB (10²¹ bytes) over the whole year, or an average 3.7 TB per second (10¹²), with a projected annual growth of 22% until 2021 [5].

For the exponential growth of optical communications to continue, the components also have to obey a Moore-like law. If the integration density of communication capacity does not keep up with the total capacity, the systems will become impractical. Not only the size, also power dissipation prohibits an approach of "just adding more boxes". Therefore, photonic integration needs to scale. Smit et al. established the photonic Moore's law in [6], observing around 20% annual growth in integration density.

Modern optical communication systems typically make use of all five physical dimensions that photons exhibit: time, space, frequency, quadrature and polarization [7], [8]. Usually, the latter four parameters are thought of as varying with time. Space division multiplexing (SDM) is usually achieved via arrays of components [9], but mode multiplexing is also getting explored [10]. Wavelength division multiplexing (WDM) makes use of the frequency parameter. The oldest and simplest modulation scheme just switches the carrier intensity in an on-off keying (OOK) scheme. To make use of both quadratures components, IQ modulation can be employed. Finally, polarization division multiplexing (PDM) makes use of the two orthogonal directions that are perpendicular to the carrier propagation direction. At least in indium phosphide (InP) platforms, PDM schemes have evaded full integration so far [11]–[13]. Silicon photonics (SiP) devices can make use of 2D grating couplers [14], [15] or non-standard platforms [16] to achieve PDM, but most demonstrated SiP transceivers also lack PDM functionality.

Classically, PDM schemes in optical communications were attributed to coherent detection schemes [11], [13], [17]–[19]. In the last decade, however, PDM was also explored in direct detection (DD) systems [20]–[25]. The PDM devices in this thesis all fall into the DD category. It has been shown [20] that DD PDM schemes can operate using four-dimensional modulation, just like coherent PDM schemes. The transmitter and receiver structures in DD schemes tend to be much simpler, however. This makes them an attractive alternative for fully integrated solutions, offering a potentially smaller footprint and cost.

1.2 Objectives

The first goal of this work is bringing PDM functionality to generic photonic integrated circuits (PICs) in InP. This is enabled by bringing manufacturable polarization rotators (PR) into the platform. As will be seen in chapter 3, a PR building block is all that is needed to enable both Tx- and Rx-type PDM functionality.

Second, to demonstrate the capabilities that a PR brings to integrated devices, a fully integrated PDM transmitter shall be designed, implemented and tested.

1.3 Structure of the Thesis

After this introduction, chapter 2 discusses optical polarization in PICs in general and particularly important aspects of PRs. Furthermore, a new design methodology for designing PRs is presented. Chapter 3 introduces new PDM-capable receiver- and transmitter designs. They make direct use of the PRs of the chapter before. Finally, chapter 4 presents experimental results of fabricated PRs, EAMs, and PDM transmitters. For this, a new measurement methodology is presented that characterizes devices in terms of their full Müller matrix. Further, high-frequency experiments and full system measurements are carried out.

2 Polarization in Photonic Integrated Circuits

The purpose of this chapter is to design integrated PRs in HHI's generic photonic integration technology. The theory used is the Jones formalism. The Jones formalism in turn requires understanding of the principles of optical anisotropy and birefringence. The Müller/Stokes formalism is also discussed in this chapter since it follows naturally from the Jones calculus and it will be needed for experiments.

2.1 Optical Anisotropy and Birefringence

The refractive index experienced by an electromagnetic wave is an effect of the wave interaction with the medium it propagates in ([26], chapter 5). When a crystalline medium is anisotropic, the refractive index will therefore also be anisotropic. In the most general case of biaxial crystals, the refractive index is different along all three spatial dimensions. Uniaxial crystals can be described by two different indices, and isotropic materials by just one. We will focus on the uniaxial case in the following. This is because in waveguide optics the longitudinal field components are often negligible, effectively rendering the refractive index along this direction negligible.

In uniaxial systems with two different indices n_x and n_y along the x- and y-axis, birefringence Δn is defined as:

$$\Delta n = n_x - n_y \quad (2.1)$$

It can be shown that in an anisotropic crystal, only waves oscillating along the crystal axes can propagate ([27], p. 8f). Polarizations entering the crystal which are not aligned with its principal axes should therefore be decomposed into the two polarizations which can propagate. This is useful to understand the working principle of wave plates, which are used to retard one polarization with respect to another. For a wave plate of thickness t , the retardation δ can be expressed as:

$$\delta = \frac{\Delta n t}{\lambda} \quad (2.2)$$

where λ is the wavelength of the incident light. Wave plates with $\delta = 0.5$ are commonly referred to as half-wave plates, whereas $\delta = 0.25$ signifies a quarter-wave plate.

The practical aspects of this thesis revolve around the InP/InGaAsP material system, which forms a Zinc blende crystal. Due to the cubic symmetry of this crystal, the material system is optically isotropic. Any optical anisotropy that is present is due to a symmetry breaking of either the waveguide geometry (this chapter) or the electronic structure of the material (e.g. in hetero structures, see chapter 3).

There are other material systems, however, in which the definition for birefringence as in eq. (2.1) does not work. Most famously in sugar solutions, but also many other liquids and organic solids, the index of refraction depends on the helicity of a light wave, rather than the direction along a linear axis. In those systems, the birefringence becomes:

$$\Delta n = n_{RHC} - n_{LHC} \quad (2.3)$$

with RHC and LHC denoting right-handed and left-handed circularly polarized light. The effect is sometimes referred to as optical activity or circular anisotropy in literature [28], [29]. As will be seen later in chapter 4, circular anisotropy can also be observed as an emergent phenomenon when arranging linearly anisotropic materials at different angles.

2.2 The Jones Formalism

2.2.1 Jones Vector and Polarization Ellipse

A common way of describing the polarization of light is the Jones Formalism [29]–[33]. Let polarized light propagate along the z-direction, with transverse components as follows:

$$E_x = E_x e^{k_x z - \omega t}; E_y = E_y e^{k_y z - \omega t} \quad (2.4)$$

In this notation, the two amplitudes $E_{x,0}$ and $E_{y,0}$ are complex, i.e. they carry a phase and an amplitude. Combining the two in a 2-vector yields the Jones vector of the wave:

$$\vec{J} = \begin{pmatrix} E_x \\ E_y \end{pmatrix} = \begin{pmatrix} |E_x| e^{i\phi_x} \\ |E_y| e^{i\phi_y} \end{pmatrix} \quad (2.5)$$

In literature, the Jones vector can also be referred to as Maxwell column [31]. The electric field vector oscillates on a trajectory in the xy-plane depending on the Jones vector. In general, it follows an elliptic trajectory. Hence, the trajectory covered after one full optical oscillation $T = \frac{\lambda}{c}$ is called the polarization ellipse. Its shape only depends on the lengths of the two components and the relative phase in between – not on the absolute phase. The oscillation of the electric field in the xy-plane for different Jones vectors is shown in figure 2-1.

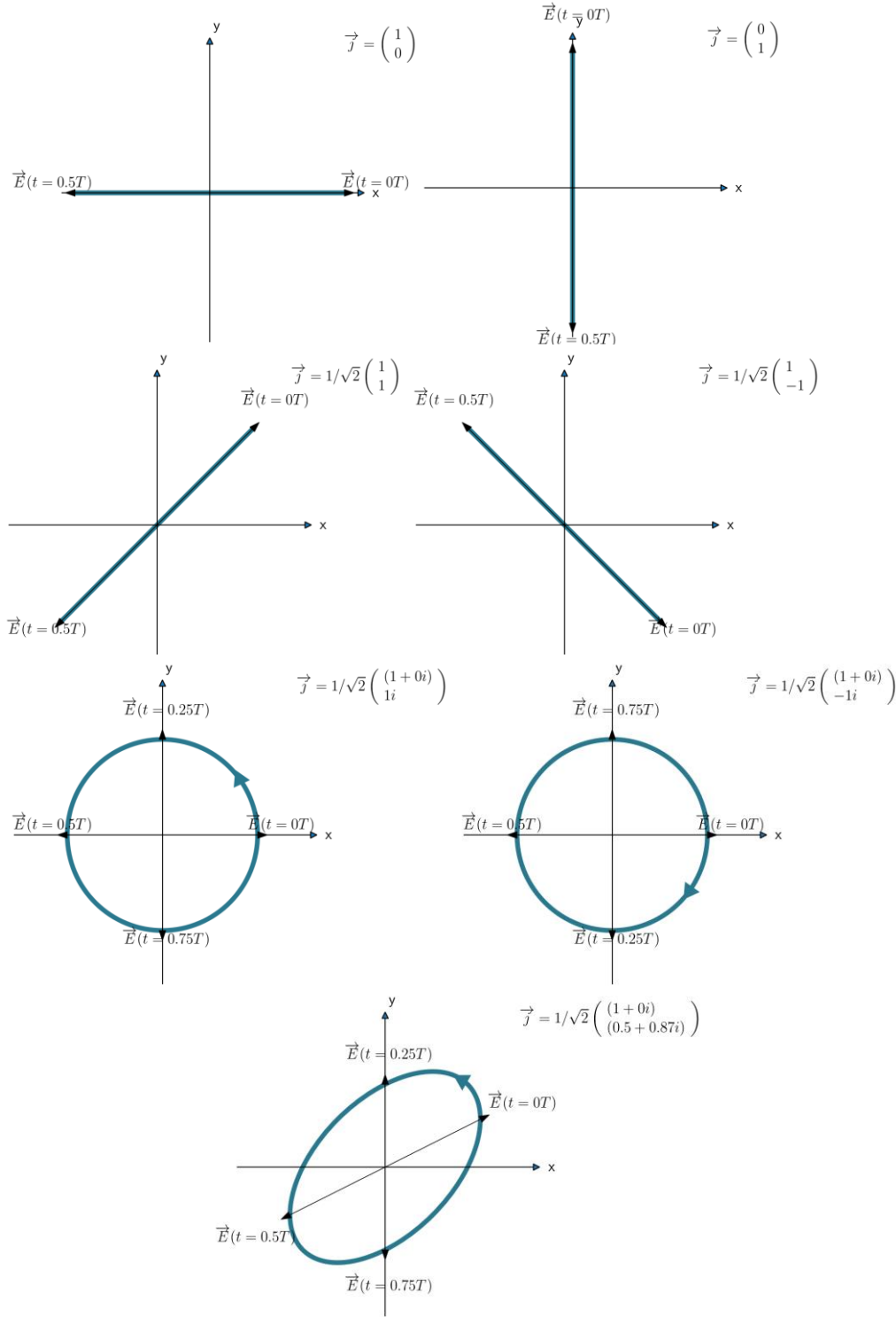


Figure 2-1. Examples for different Jones vectors and the corresponding trajectories (blue) of the electric field in the xy -plane. The field vector for different times within one optical period $T = \frac{1}{f} = \frac{\lambda}{c}$ is shown. In the case of the first four Jones vectors, the electric field vector oscillates along a straight line, hence the polarization is called to be linear. Circular polarization can oscillate left handedly or right handedly (fifth and sixth Jones vector). The most general case is elliptical polarization (bottom), of which the others can be regarded as special case.

The general polarization ellipse is shown in figure 2-2. It is constituted by two angles: ψ and χ . The former describes the rotation of the principal axes with respect to the x-axis. The latter describes the ellipticity. They can both be calculated directly from the Jones vector via (see p.8 in [29]):

$$\tan 2\psi = \frac{2|E_x||E_y|}{|E_x|^2 - |E_y|^2} \cos(\phi_x - \phi_y) \quad (2.6)$$

The two radii of the ellipse are

$$\begin{aligned} a^2 &= |E_x|^2 \cos^2 \psi + |E_y|^2 \sin^2 \psi + 2|E_x||E_y| \cos \psi \sin \psi \cos(\phi_x - \phi_y) \\ b^2 &= |E_x|^2 \sin^2 \psi + |E_y|^2 \cos^2 \psi - 2|E_x||E_y| \cos \psi \sin \psi \cos(\phi_x - \phi_y) \end{aligned} \quad (2.7)$$

From this, the ellipticity becomes:

$$\tan(\chi) = \pm \frac{b}{a} \quad (2.8)$$

With the sign in (2.8) being the sign of $\phi_x - \phi_y$. The sign of χ gives the helicity or handedness of the ellipse. For positive χ , the electric field vector rotates in the xy-plane in the mathematically positive sense (right handed).

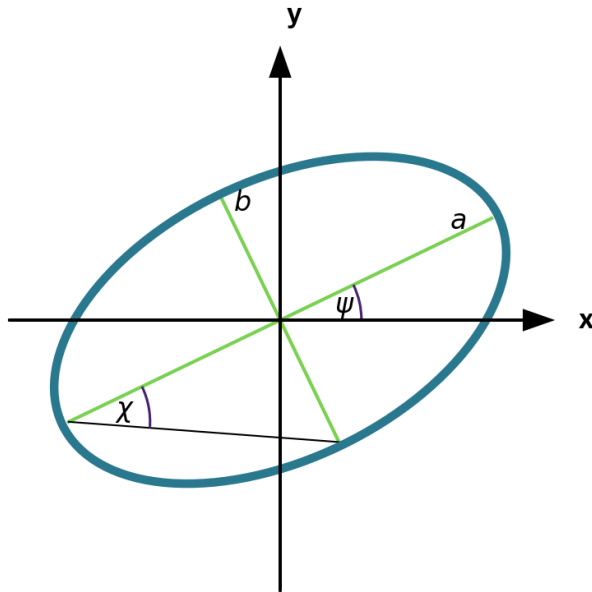


Figure 2-2. The general polarization ellipse and its parameters. The semi-major and -minor axes are a and b , respectively. The axes are rotated by ψ . The ellipticity is characterized by χ . The helicity (i.e. the sense of rotation of the electric field vector) is given by the sign of χ . If one of the axes has vanishing length, the polarization is linear. If their lengths are equal, the polarization is circular.

Since Jones vectors are coherent representations of light, they can describe interference. The Jones vector of two light beams being superimposed can be obtained by calculating the superposition of the two initial Jones vectors.

2.2.2 Jones Matrix

Light propagating through a medium will in general change its Jones vector. In the regime of linear optics, this change is described by a matrix multiplication. The matrix operator mapping one Jones vector onto another usually is referred to as Jones matrix [29]–[31]. Since Jones vectors are complex 2-vectors, Jones matrices are complex 2x2 matrices. With the thoughts and notations from 2.1, the Jones matrix of a birefringent crystal becomes:

$$\underline{J}_\delta = \begin{pmatrix} e^{i\pi\delta} & 0 \\ 0 & e^{-i\pi\delta} \end{pmatrix} \quad (2.9)$$

Rotating the crystal around the optical axis by an angle θ amounts to the transformation

$$\underline{J}_{\delta,\theta} = \underline{R}(\theta) \cdot \underline{J}_\delta \cdot \underline{R}(-\theta) \quad (2.10)$$

With $\underline{R}(\theta)$ being the rotation matrix:

$$\underline{R}(\theta) = \begin{pmatrix} \cos \theta & -\sin \theta \\ \sin \theta & \cos \theta \end{pmatrix} \quad (2.11)$$

In this framework, matrices of the following wave plates can readily be understood:

$$\underline{J}_{\frac{\lambda}{2}, 0^\circ} = \begin{pmatrix} -i & 0 \\ 0 & i \end{pmatrix}; \underline{J}_{\frac{\lambda}{2}, 45^\circ} = \begin{pmatrix} 0 & -i \\ -i & 0 \end{pmatrix}; \underline{J}_{\frac{\lambda}{4}, 0^\circ} = \frac{1}{\sqrt{2}} \begin{pmatrix} 1-i & 0 \\ 0 & 1+i \end{pmatrix}; \underline{J}_{\frac{\lambda}{4}, 45^\circ} = \frac{1}{\sqrt{2}} \begin{pmatrix} 1 & -i \\ -i & 1 \end{pmatrix} \quad (2.12)$$

Hence, a half-wave plate rotated by 45° can be regarded as a polarization converter, as it exchanges the elements of the Jones vector (apart from adding a 90° phase term to both).

2.3 The Müller/Stokes Formalism

2.3.1 Stokes Vectors and the Poincaré Sphere

The Stokes formalism is based on two mathematical objects: Stokes vectors and Müller matrices, which act on Stokes vectors [26], [29], [31], [34], [35]. The former describe the state of polarization (SOP) of a given signal, the latter a medium and how it acts on the SOP. The Stokes vector of a given optical signal can be measured with a photodetector, a linear polarizer and a circular polarizer. Six measurements are carried out with the polarizers in front of the detector: four with the linear polarizer and two with the circular polarizer. The first four measurements are done with different rotations of the linear polarizer around the optical axes: 0° , 90° , 45° and 135° . The last two measurements are done with the circular polarizer transmitting left-handed and then right-handed polarized light. Switching from one to the other can be achieved by flipping the circular polarizer. The six measured powers then comprise the Stokes vector as follows:

$$\vec{s} = \begin{pmatrix} s_0 \\ s_1 \\ s_2 \\ s_3 \end{pmatrix} = \begin{pmatrix} P_{0^\circ} + P_{90^\circ} \\ P_{0^\circ} - P_{90^\circ} \\ P_{45^\circ} - P_{135^\circ} \\ P_{RHC} - P_{LHC} \end{pmatrix} \quad (2.13)$$

Because no phase measurements need to be done, the Stokes vector is much more convenient experimentally. Definitions with different signs for s_3 also exist. We use the present definition because it orients the polarization ellipse in the mathematically positive

sense for positive s_3 . It can easily be shown (p.23 in [29]) that with the definition for the Jones vector (2.5) and $\phi = \phi_x - \phi_y$, \vec{s} and \vec{j} are related by:

$$\vec{s} = \begin{pmatrix} s_0 \\ s_1 \\ s_2 \\ s_3 \end{pmatrix} = \begin{pmatrix} |E_x|^2 + |E_y|^2 \\ |E_x|^2 - |E_y|^2 \\ 2|E_x||E_y|\cos\phi \\ 2|E_x||E_y|\sin\phi \end{pmatrix} \quad (2.14)$$

Since s_0 only gives the total power of a signal, it makes sense to normalize the Stokes vector via \vec{s}/s_0 . Then, it can be shown that:

$$s_1^2 + s_2^2 + s_3^2 \leq 1 \quad (2.15)$$

In the limit of fully polarized light, the inequality becomes an equality. In this case, the triple (s_1, s_2, s_3) exists on a sphere with unity radius, the Poincaré sphere [36]. Each point on the Poincaré sphere uniquely determines the polarization ellipse and vice versa. With (2.14) and the equations for the polarization ellipse (2.6)-(2.8), it can easily be shown that the angles defining the polarization ellipse, ψ and χ , are twice the spherical coordinates of the Stokes vector on the Poincaré sphere:

$$\vec{s} = \begin{pmatrix} s_0 \\ s_1 \\ s_2 \\ s_3 \end{pmatrix} = \begin{pmatrix} s_0 \\ \cos 2\psi \cos 2\chi \\ \sin 2\psi \cos 2\chi \\ \sin 2\chi \end{pmatrix} \quad (2.16)$$

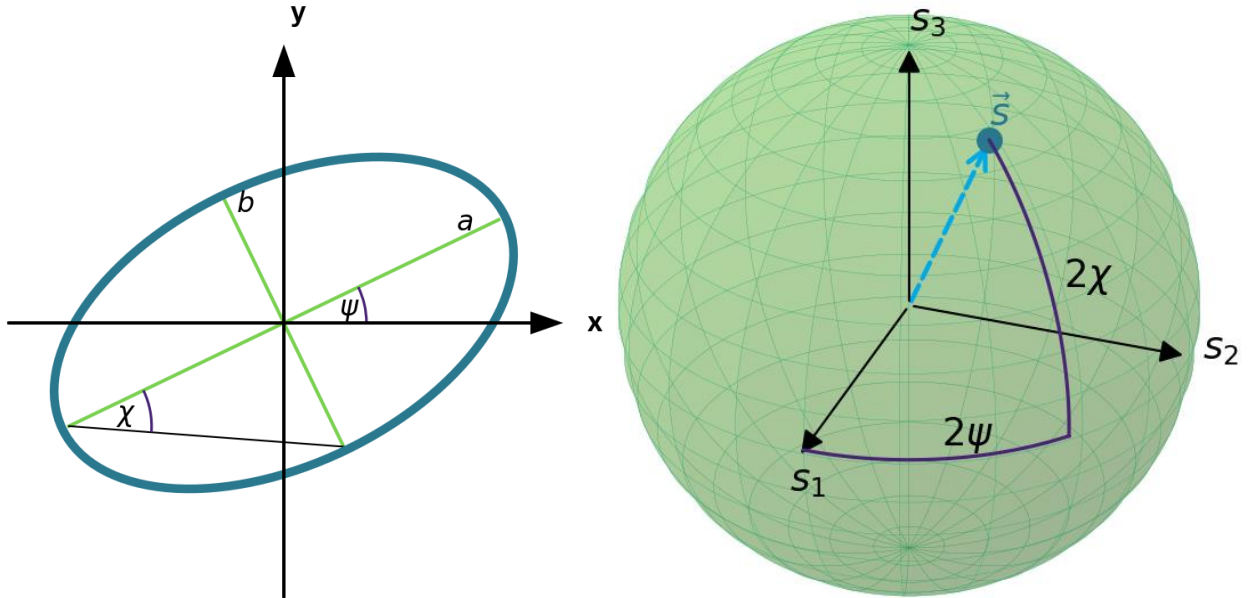


Figure 2-3. Correspondence between polarization ellipse (left) and Poincaré sphere (right). The Stokes vector is a point on the Poincaré sphere, with the spherical coordinates $(2\psi, 2\chi)$, so twice the angles that define the polarization ellipse. The numerical values used for the plots are $\psi = \frac{\pi}{7}$ and $\chi = \frac{\pi}{6}$, giving $\vec{s} \approx (1, 0.31, 0.39, 0.87)$ or $\vec{j} \approx (0.81, 0.24 + 0.53i)$.

To complement the SOPs visualized in figure 2-1, the Stokes vectors of linear polarized light along 0° , 90° , 45° and 135° , as well as left-handed and right-handed circular polarized light are¹:

$$\vec{s}_{0^\circ} = \begin{pmatrix} 1 \\ 1 \\ 0 \\ 0 \end{pmatrix}; \vec{s}_{90^\circ} = \begin{pmatrix} 1 \\ -1 \\ 0 \\ 0 \end{pmatrix}; \vec{s}_{45^\circ} = \begin{pmatrix} 1 \\ 0 \\ 1 \\ 0 \end{pmatrix}; \vec{s}_{135^\circ} = \begin{pmatrix} 1 \\ 0 \\ -1 \\ 0 \end{pmatrix}; \vec{s}_{RHC} = \begin{pmatrix} 1 \\ 0 \\ 0 \\ 1 \end{pmatrix}; \vec{s}_{LHC} = \begin{pmatrix} 1 \\ 0 \\ 0 \\ -1 \end{pmatrix} \quad (2.17)$$

The correspondence between Poincaré sphere, polarization ellipse and Stokes vector is illustrated in figure 2-3. As opposed to Jones vectors, superimposing Stokes vectors does not represent the polarization that emerges by superimposing two polarizations. The Stokes Vector of x-polarized light is $(1 \ 1 \ 0 \ 0)$, that of y-polarized light is $(1 \ -1 \ 0 \ 0)$. The superposition yields $(2 \ 0 \ 0 \ 0)$, which corresponds to unpolarized light of twice the power. This can be intuitively understood since the Stokes vector does not contain information on the absolute phase and therefore cannot describe interference. The superposition of Stokes vectors does hold, however, if the two beams are mutually incoherent [31].

As has been pointed out by Feynman and Vernon in 1956 [37], a geometrical representation like the Stokes vector on the Poincaré sphere is useful not just in optics but also throughout quantum mechanics. It can be used to describe any two level system with two complex amplitudes (like the two elements of the Jones vector). In this case, the geometrical representation works the same but is commonly referred to as Bloch sphere (p. 15 in [38]). A Bloch sphere then represents a so-called qubit.

2.3.2 Distance on a Sphere

In both theory and experiment, it is useful to have a metric that quantifies the difference between two SOPs – we need such a metric in chapter 4. One can think of various ways of quantifying the difference between two SOPs. The Euclidean metric between two Stokes vectors does not reflect the spherical nature of the problem. It would represent “short cuts” through the sphere, where only curved lines along the sphere exist. Another possibility might be a metric using the differences between the two spherical angles, e.g. $\sqrt{\Delta\psi^2 + \Delta\chi^2}$. But it is not a physically useful measure, as can be understood at the poles of the Poincaré sphere, i.e. at $\chi = \pm 45^\circ$. At this latitude, all longitudes ψ give the same point, namely the upper (lower) pole of the sphere. Then, $\sqrt{\Delta\psi^2 + \Delta\chi^2}$ might be large even when the SOPs to be compared almost coincide. Therefore, the metric used throughout this thesis is the central angle.

It can be shown (see appendix D1)) that the central angle $\Delta\xi$ between two points on a sphere with spherical coordinates $(2\psi_1, 2\chi_1)$ and $(2\psi_2, 2\chi_2)$ is given by:

$$\Delta\xi = \arccos(\sin 2\chi_1 \sin 2\chi_2 + \cos 2\chi_1 \cos 2\chi_2 \cos(2\psi_1 - 2\psi_2)) \quad (2.18)$$

¹ The total power s_0 is normalized to unity

The factor 2 in front of the angles is used here so two points represent a polarization ellipse with angles ψ_i and χ_i as in chapter 2.3.1. $\Delta\xi$ can be thought as the geodesic between two points on a sphere of unity radius. The geodesic generally is an arc segment of a great circle around that sphere. The relationship is illustrated in figure 2-4.

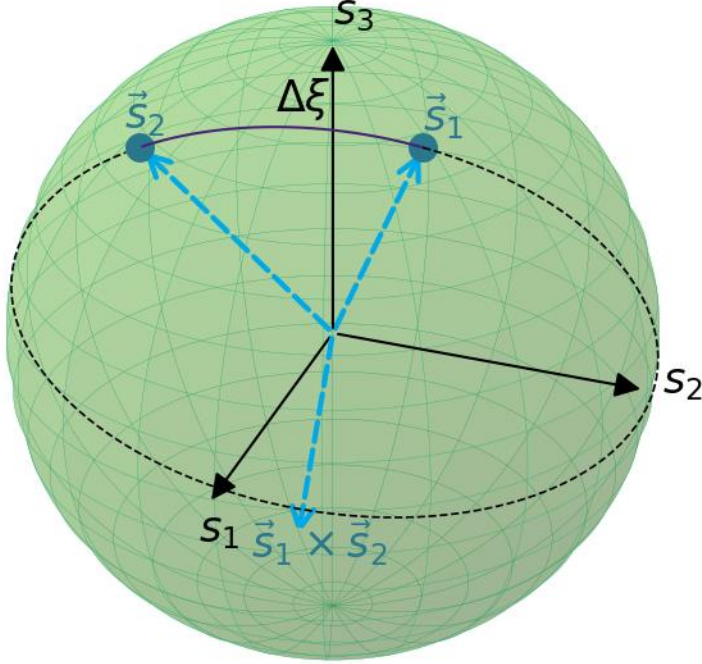


Figure 2-4. Illustration of the central angle $\Delta\xi$ between two polarization states \vec{s}_1 and \vec{s}_2 on the Poincaré sphere. The angle can be calculated with (2.18). The measure is also referred to as great circle distance or geodesic. This is because the central angle $\Delta\xi$ is the arc connecting the two vectors along their common great circle on the sphere. The great circle (dashed black circle) is defined as the circle around the axis $\vec{s}_1 \times \vec{s}_2$. The central angle is a mathematically well-behaved measure of the difference between two polarization states.

2.3.3 Müller Matrices

The Müller matrix acts on \vec{s} as follows:

$$\underline{M}\vec{s} = \begin{pmatrix} m_{00} & m_{01} & m_{02} & m_{03} \\ m_{10} & m_{11} & m_{12} & m_{13} \\ m_{20} & m_{21} & m_{22} & m_{23} \\ m_{30} & m_{31} & m_{32} & m_{33} \end{pmatrix} \begin{pmatrix} s_0 \\ s_1 \\ s_2 \\ s_3 \end{pmatrix} \quad (2.19)$$

Just like Stokes vectors, Müller matrices are real-valued. R. C. Jones himself called the calculus using these matrices “more powerful” than Jones matrices [35]. Even though they are generally attributed to Hans Müller for his contributions in the 1940s [39], they were already considered by Paul Soleillet in 1929 [40]. A Müller matrix does not necessarily have to be unitary, as in the case of (di-) attenuation or depolarization. Diattenuation describes a process of polarization dependent attenuation. The name stems from the fact that such an element generally has two eigenvectors of physical significance². These eigenpolarizations

² Only eigenpolarizations with positive real eigenvalues have physical significance in the Stokes formalism. Negative or complex eigenvalues would correspond to negative or complex power and energy.

remain unchanged by the element except for an attenuating factor, the corresponding eigenvalue. For instance, a linear diattenuator with attenuations q and r acts on linear polarized light as:

$$\underline{M}_D = \frac{1}{2} \begin{pmatrix} q+r & q-r & 0 & 0 \\ q-r & q+r & 0 & 0 \\ 0 & 0 & 2\sqrt{qr}\cos(\delta) & 2\sqrt{qr}\sin(\delta) \\ 0 & 0 & -2\sqrt{qr}\sin(\delta) & 2\sqrt{qr}\cos(\delta) \end{pmatrix}; \quad \underline{M}_D \cdot \begin{pmatrix} 1 \\ 1 \\ 0 \\ 0 \end{pmatrix} = \begin{pmatrix} q \\ q \\ 0 \\ 0 \end{pmatrix}; \quad \underline{M}_D \cdot \begin{pmatrix} 1 \\ -1 \\ 0 \\ 0 \end{pmatrix} = \begin{pmatrix} r \\ -r \\ 0 \\ 0 \end{pmatrix} \quad (2.20)$$

Retarding elements are represented by unitary matrices. The eigenvectors of retarders are generally elliptical states of polarization. If these eigenpolarizations are linear or circular, the corresponding element is referred to as a linear or circular retarder, respectively. Linear retarders are by far the most common retarders, as birefringent crystals with their birefringent axes introduce phase retardation to linear states of polarization. Elliptical retardation can, however, emerge from the combination of several linear retarders which are rotated with respect to one another. The matrix of a linear retarder aligned with the xy coordinate system is (chapter 22, [26]):

$$\underline{M}_\delta = \begin{pmatrix} 1 & 0 & 0 & 0 \\ 0 & 1 & 0 & 0 \\ 0 & 0 & \cos(\delta) & \sin(\delta) \\ 0 & 0 & -\sin(\delta) & \cos(\delta) \end{pmatrix} \quad (2.21)$$

Rotation of an element around the optical axis is represented by

$$\underline{M}_{\delta,\theta} = \underline{R}(\theta) \cdot \underline{M}_\delta \cdot \underline{R}(-\theta) \quad (2.22)$$

The rotational matrix for Müller matrices is

$$\underline{R}(\theta) = \begin{pmatrix} 1 & 0 & 0 & 0 \\ 0 & \cos(2\theta) & \sin(2\theta) & 0 \\ 0 & -\sin(2\theta) & \cos(2\theta) & 0 \\ 0 & 0 & 0 & 1 \end{pmatrix} \quad (2.23)$$

Just like for Jones matrices, this framework of linear retardation and rotation is enough to write down the matrices of waveplates, e.g.:

$$\underline{M}_{\frac{\lambda}{2},0^\circ} = \begin{pmatrix} 1 & 0 & 0 & 0 \\ 0 & 1 & 0 & 0 \\ 0 & 0 & -1 & 0 \\ 0 & 0 & 0 & 1 \end{pmatrix}; \quad \underline{M}_{\frac{\lambda}{2},45^\circ} = \begin{pmatrix} 1 & 0 & 0 & 0 \\ 0 & -1 & 0 & 0 \\ 0 & 0 & 1 & 0 \\ 0 & 0 & 0 & -1 \end{pmatrix}; \quad \underline{M}_{\frac{\lambda}{4},45^\circ} = \begin{pmatrix} 1 & 0 & 0 & 0 \\ 0 & 0 & 0 & -1 \\ 0 & 0 & 1 & 0 \\ 0 & 1 & 0 & 0 \end{pmatrix} \quad (2.24)$$

Since waveplates are unitary operators, they can be thought of as rotational operators on the Poincaré sphere. A comparison of the lower right 3x3 kernel of $\underline{M}_{\delta,\theta}$ with the matrix rotating a 3D vector around an axis \vec{R} by α yields:

$$\vec{R} = \begin{pmatrix} \cos(2\theta) \\ \sin(2\theta) \\ 0 \end{pmatrix} \quad (2.25)$$

$$\alpha = -\delta \quad (2.26)$$

These relations are useful to understand a linear retarder on the Poincaré sphere. They are visually summarized in figure 2-5. The axis around which the element rotates the state of polarization is in the s_1s_2 -plane. It is impossible to rotate the state of polarization around the s_3 -axis. The axis' angle is given directly by the rotation of the retarder around the optical axis. The angle of rotation on the Poincaré sphere is given by the element's phase retardation.

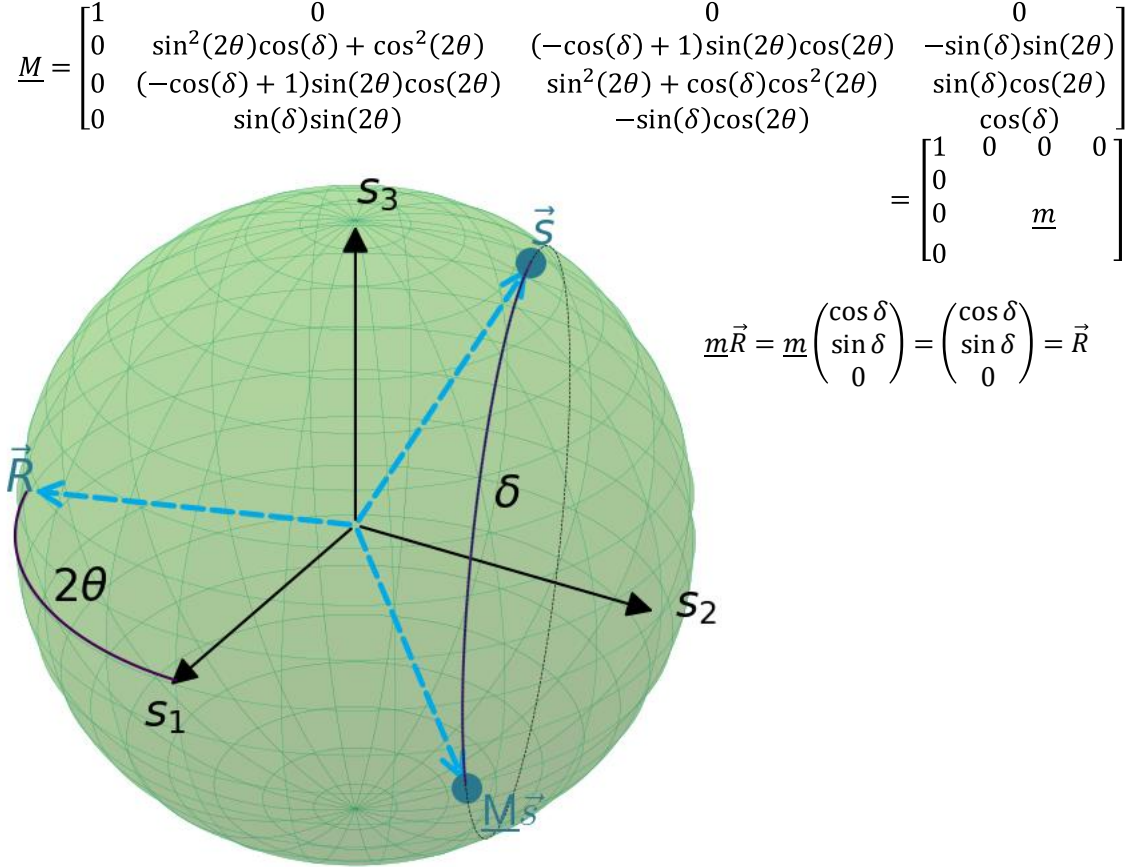


Figure 2-5. Operation principle of a linear retarder on the Poincaré sphere. A general linear retarder Müller matrix is given at the top. The retardation is δ and the element is rotated around the optical axis by θ . The only real-valued eigenvector of the retarder is \vec{R} . It is a linear polarization state and hence lies on the s_1s_2 -circle. The polarization \vec{R} is not affected by the element represented by \underline{M} . Rather, \vec{R} is the axis around which the retarder rotates. It encloses an angle of 2θ with the s_1 -axis. The angle by polarization is rotated is δ .

Another way of looking at the rotation on the Poincaré sphere is as follows: since the lower-right 3x3 kernel $\underline{m}_{\delta,\theta}$ of $\underline{M}_{\delta,\theta}$ rotates Stokes vectors around an axis \vec{R} , applying $\underline{m}_{\delta,\theta}$ to \vec{R} itself must have no effect:

$$\underline{m}_{\delta,\theta}\vec{R} = \vec{R} \quad (2.27)$$

In other words, \vec{R} is an eigenvector to $\underline{m}_{\delta,\theta}$ with eigenvalue 1. But since the eigenvectors (or eigenpolarizations) of linear retarders are linear polarizations, they cannot have a s_3 -component. So generally, rotation around the s_3 -axis requires circular or elliptical retarders.

In this general case, \vec{R} can have any direction in Stokes space. Therefore, the eigenpolarizations of the corresponding retarders are elliptical. Their eigenpolarizations consequently have a latitude on the Poincaré sphere $2\chi \neq 0$. Together with elliptical diattenuators, their mathematics are summarized in appendix A).

The connection between Jones and Müller matrices has been derived by Gerrard and Burch in appendix F of [31]. The derivation of the Müller matrix from a Jones matrix is exact, whereas the opposite only exists for non-depolarizing elements and has arbitrary phase. The analogous statement is true for Jones and Stokes vectors.

2.4 Optical Waveguides

This section outlines how optical waveguides and their polarization properties can be understood with matrix methods. Since waveguide design and simulation usually makes use of complex amplitudes for each mode involved, the Jones formalism is a natural choice. It will be used for the remainder of the entire chapter.

2.4.1 Analogy between plane waves and guided waves

Although the Jones formalism is intended for plane waves, it can also be used as an approximation for guided waves. The quality of this approximation will be discussed in chapter 2.5. There are clear analogies between plane waves in anisotropic crystals and guided modes in optical waveguides: the principal axes in the crystal correspond to the polarizations of the guided modes. Birefringence in the crystal corresponds to the difference of effective indices of the guided modes.

The polarization of a guided mode can be expressed in terms of its relative energy polarized along the x- and y-axes:

$$Pol_x = \frac{\int |E_x|^2 dx dy}{\int (|E_x|^2 + |E_y|^2) dx dy}; Pol_y = \frac{\int |E_y|^2 dx dy}{\int (|E_x|^2 + |E_y|^2) dx dy} \quad (2.28)$$

The angle θ relative to the x-axis of the guided mode then writes as:

$$\theta = \arccos(\sqrt{Pol_x}) \quad (2.29)$$

With this definition of a mode angle, the orthogonal modes of a waveguide (like TE- and TM-modes) also have orthogonal angles. So, just like in an anisotropic crystal, incoming waves should be thought of as getting decomposed into the two modes, which then propagate. Jones matrices as in 2.2.2 can be used as propagators. All simulations of mode profiles are performed by the commercial software package MODE that is supplied by Lumerical Solutions Inc. [41]. It uses an FDE solver. The detailed solver parameters are given in Table 3.

2.4.2 Symmetric Waveguides

Waveguides with a symmetric cross section generally support modes that are polarized parallel or perpendicular to the plane of symmetry. For typical integrated planar waveguides, this means that they are polarized parallel and perpendicular to the substrate.

In literature, the mode parallel to the substrate is typically called the (quasi-) TE mode, while the perpendicular mode is referred to as (quasi-) TM mode³ [42]–[44]. So, if we define the x -axis to be parallel to the substrate, the TE mode has $\theta = 0^\circ$, while the TM mode has $\theta = 90^\circ$.

Figure 2-6 shows the index distribution and the mode profile of the deeply etched waveguide used in this work. Its guiding core consists of an iron doped quaternary InGaAsP layer with a photoluminescence (PL) peak at $1.06\ \mu\text{m}$. We will refer to the PL peak wavelength of a material simply as PL in the following. Since the core is fully etched, it is referred to as a deeply etched waveguide. The details of the material models used in this chapter are in appendix B). It can be seen that although the material system InP is optically isotropic, guided modes exhibit birefringence. This birefringence is only due to the geometry of the waveguide and is therefore called geometric or waveguide birefringence, as opposed to material birefringence. The birefringence in this example amounts to $\Delta n = 1.7 \times 10^{-3}$.

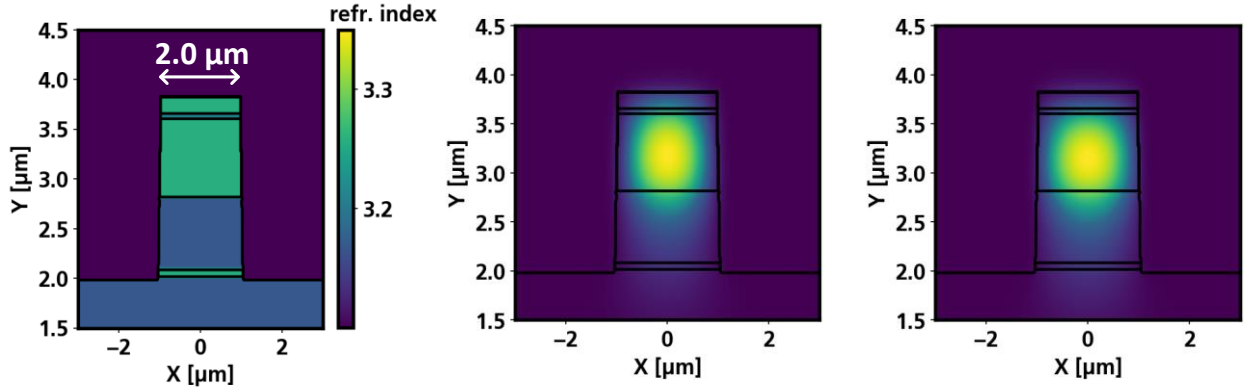


Figure 2-6. Left: Refractive index profile of a deeply etched waveguide on InP substrate. The guiding core is InGaAsP with a PL of $1.06\ \mu\text{m}$. The waveguide is $2\ \mu\text{m}$ wide and supports two modes. Middle: profile of the total electric field of the guided mode with $\theta = 0^\circ$, i.e. the TE mode. Right: same profile of the TM-mode ($\theta = 90^\circ$). The TE mode has an effective index of 3.2006, while the TM mode has an effective index of 3.1989.

2.4.3 Asymmetric Waveguides

If a waveguide has no distinct symmetry, it may still support two orthogonal modes, i.e. their angle relative to each other is still 90° . Their absolute angles, however, can take on any value and depend on the waveguide geometry. To exploit this behavior, a waveguide etch in the generic platform that is based on HBr wet chemistry is used. Figure 2-7 shows the cross section of this waveguide. In the case of a waveguide width of $1.4\ \mu\text{m}$ as shown, the modal coordinate system is tilted by 38° with respect to the substrate coordinate system. The birefringence is $\Delta n = 1.8 \times 10^{-3}$.

An asymmetric waveguide with a modal basis tilted by an angle θ can be thought of as a symmetric waveguide rotated around the optical axis by this angle. This enables a clear

³In real dielectric waveguides, there is always some non-vanishing longitudinal component of both the electric and the magnetic fields. The convention comes from the solutions of infinite slab waveguides, which really have vanishing longitudinal E-field for one mode, and vanishing longitudinal H-field for the other.

path of engineering any desired Jones matrix in an integrated planar device: the retardation is determined by the waveguide geometry (giving the birefringence) and length. Inducing an asymmetry then enables rotation of the retarder by in principle any arbitrary angle. One way of altering both birefringence and rotation is to change the width of the waveguide. Since this parameter is technologically easily accessible (via the mask), all devices will be designed using the waveguide width as the design parameter. The dependence of birefringence and rotation on waveguide width are shown in figure 2-8.

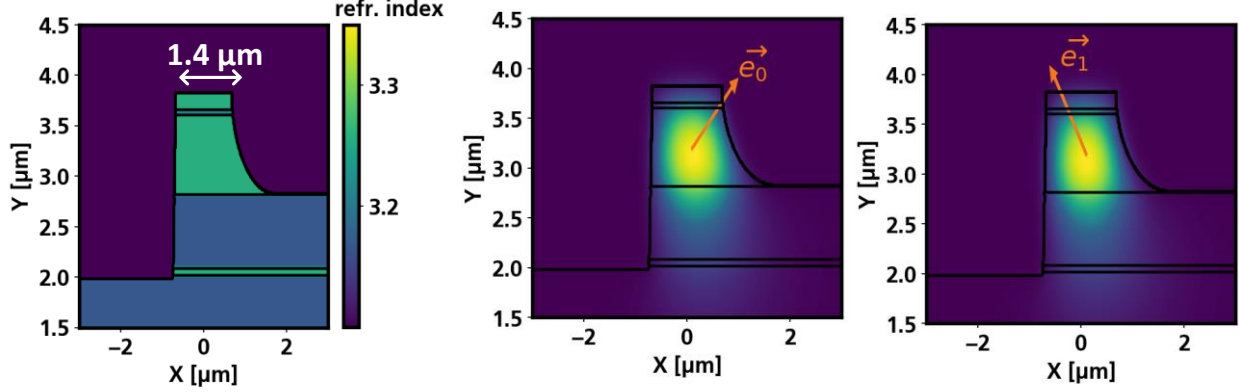


Figure 2-7. Left: Refractive index profile of an asymmetric waveguide on InP substrate. The waveguide has a core material with a peak photoluminescence of 1.06 μm (green) and is surrounded by air (purple). The top width is 1.4 μm. Middle: electric field profile of the "slow mode", with an effective index of 3.1847 and $\theta = 38^\circ$. Right: electric field profile of the "fast mode", with an effective index of 3.1829 and $\theta = -52^\circ$.

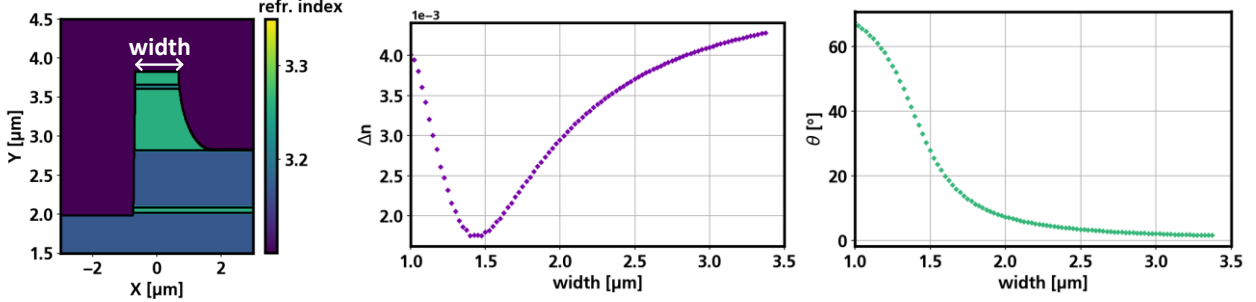


Figure 2-8. Simulations of the properties of an asymmetric waveguide (left) as a function of its width. Both the birefringence (middle) and mode rotation (right) are shown. The rotation is shown for the mode that approaches the TE-regime ($\theta = 0$) for $\text{width} \rightarrow \infty$. The other guided mode always stays orthogonal to this mode.

To facilitate the design of the asymmetric waveguide devices, fitting formulas are used. For the birefringence, the fit as a function of the waveguide width w writes as:

$$\Delta n = aw^3 + bw^2 + cw + \frac{d}{w} + \frac{e}{w^2} + \frac{f}{w^3} + g \quad (2.30)$$

For the mode rotation θ , the fit is:

$$\theta = \alpha \arctan(\beta w + \gamma) - \epsilon \quad (2.31)$$

The quality of these fits and the values of the parameters are shown in figure 2-9. With these fits, writing down the Jones Matrix of a given piece of waveguide of length L and

width w becomes just a matter of inserting equations (2.30) and (2.31) into (2.10), using $\delta = \frac{\Delta n L}{\lambda}$. The result is of the form:

$$\underline{J}_{WG}(w) = \begin{pmatrix} e^{i\pi\delta(w)} \sin^2(\theta(w)) + e^{-i\pi\delta(w)} \cos^2(\theta(w)) & \frac{1}{2}(1 - e^{2i\pi\delta(w)})e^{-i\pi\delta(w)} \sin(2\theta(w)) \\ \frac{1}{2}(1 - e^{2i\pi\delta(w)})e^{-i\pi\delta} \sin(2\theta(w)) & e^{-i\pi\delta(w)} \sin^2(\theta(w)) + e^{i\pi\delta(w)} \cos^2(\theta(w)) \end{pmatrix} \quad (2.32)$$

So, the Jones Matrix of any waveguide can be written down in closed form, at least in principle. If the waveguide is mirrored along the y-axis, θ changes sign. In the following, we write the Jones matrix of a waveguide as in figure 2-7 as \underline{J}_{WG} , while we write the matrix of the waveguide mirrored along the y-axis as \underline{J}'_{WG} (i.e. \underline{J}_{WG} with θ of opposite sign). The complexity of (2.32) makes it impractical to be handled by hand. A modern computer, however, can compute the numerical value of the matrix for any given waveguide width with relative ease. In particular, this calculation is in general much faster than a full simulation in a commercial beam propagation tool like MODE, as will be shown in the next chapter.

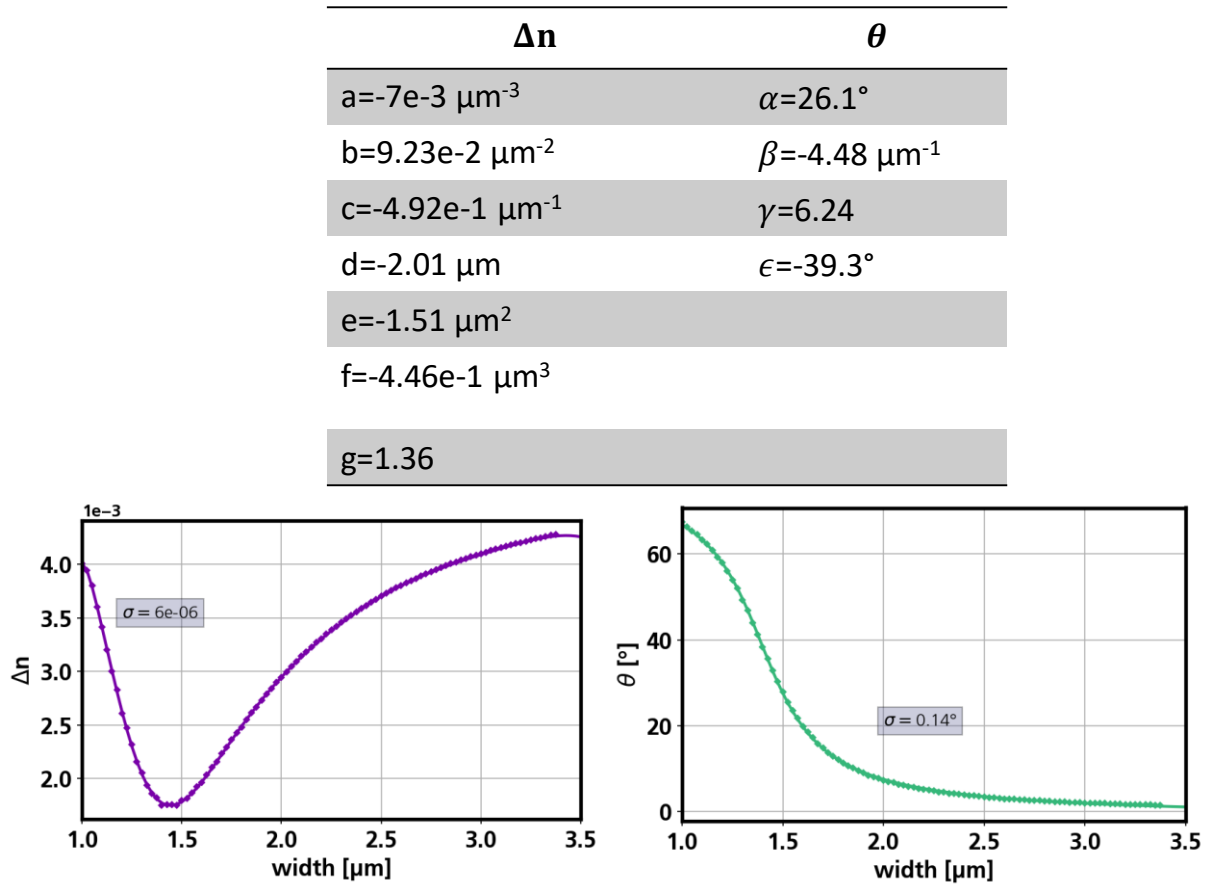


Figure 2-9. Top: Tabulated values for the fitting parameters of the asymmetric waveguide from Figure 2-7. The analytic fits for birefringence (left) and mode rotation (right) are in good agreement for waveguide widths from 1 to 3.5 μm . The average errors of the fits for birefringence and modal tilt are 6×10^{-6} and 0.14° , respectively.

2.5 Integrated Polarization Converters

2.5.1 Basic Principle and Single Section Device

To recall the result from chapter 2.2.2, polarization conversion is achieved with a device with $\delta = 0.5$ and $\theta = 45^\circ$. With the results from figure 2-9, it is found that $\theta(1.34 \mu\text{m}) \approx 45^\circ$. This in turn means $\Delta n = 1.914 \times 10^{-3}$. With $\delta = \frac{\Delta n L}{\lambda} \stackrel{!}{=} 0.5$, this forces $L \stackrel{!}{=} L_\pi = 409.2 \mu\text{m}$ at a wavelength of $1.55 \mu\text{m}$. To verify this design, simulations are carried out using the eigenmode expansion (EME) method in Lumerical's MODE. Since the modes have to be propagated, the EME package is used. The figure of merit is the polarization extinction ratio (PER) at the output:

$$PER = \frac{Pol_Y}{Pol_X} = \frac{\int |E_y|^2 dx dy}{\int |E_x|^2 dx dy} \quad (2.33)$$

The desired PER is ∞ when the input is purely x-polarized and 0 when the input is purely y-polarized. In MODE simulations, the PER can easily be calculated by calculating the field profile at the output for the corresponding input field. In Jones calculus, we can probe the device matrix \underline{J}_{WG} with an x-polarized input vector and calculate the output:

$$\vec{J}_{out} = \underline{J}_{WG} \cdot \vec{J}_X = \underline{J}_{WG} \cdot \begin{pmatrix} 1 \\ 0 \end{pmatrix} \quad (2.34)$$

The PER then writes as:

$$PER = \frac{|j_{out,1}|^2}{|j_{out,0}|^2} \quad (2.35)$$

The comparison of both calculations for the $1.34 \mu\text{m}$ wide and $405 \mu\text{m}$ long device is shown in figure 2-10, together with a cartoon of the device. The Jones calculations match the EME simulations excellently. The results makes it evident, however, how sensitive this device would be to fabrication errors. Even if the compositions and thicknesses of the epitaxial layers are matched perfectly, 20 dB of PER are hard to achieve. The waveguide width has to be exact to $\sim 50 \text{ nm}$. For a PER above 10 dB, the accuracy still has to be better than $\sim 150 \text{ nm}$. For the processes used in HHI's generic InP technology, this accuracy is impractical. The following sections will therefore explore options to relax the requirements

on the process technology.

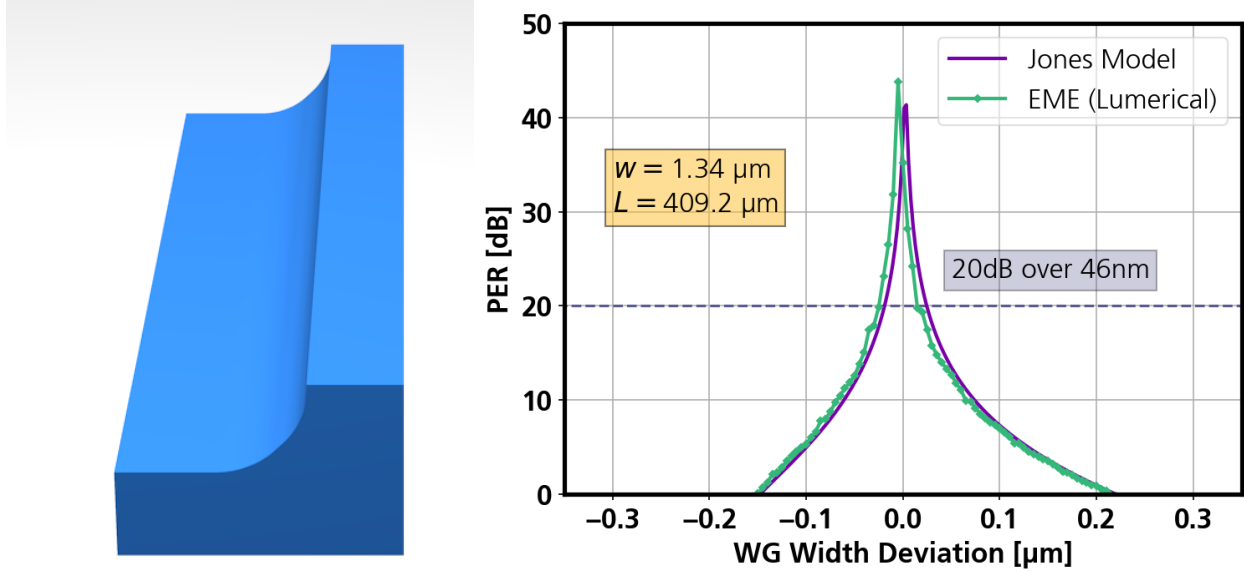


Figure 2-10. Left: Rendered 3D cartoon of the polarization converter based on the asymmetric waveguide as discussed in chapter 2.4.3. Right: dependence of the PER on the waveguide width deviation from the ideal width of $1.34 \mu\text{m}$. The dependence is calculated using Lumerical's EME solver as well as the Jones model. For 20 dB of PER, the width deviation has to be below 56 nm.

2.5.2 Two Section Device

One way of relaxing the fabrication accuracy has been proposed by Dzibrou et al. at the Technical University of Eindhoven [45], [46]. The idea is also filed as an US patent [47]. The core idea is to use two asymmetric waveguides instead of one. The geometry of both should be the same, but the cross sections are mirror images of one another. As a result, the mode rotations of the two sections become $\theta_1 = -\theta_2 = 45^\circ$. Further, it is proposed to use $\delta_1 = 0.25$ and $\delta_2 = 0.75$. Since the total retardation then amounts to 1, the proposed device is twice as long as the device in chapter 2.5.1. The advantage of this two section design is its decreased sensitivity to fabrication errors, as shown in figure 2-11. Again, the device is simulated in MODE as well as using the Jones model. In the Jones model, the total device matrix writes as:

$$\underline{J}_{PC} = \underline{J}_{WG} \left(w, \frac{L_\pi}{2} \right) \cdot \underline{J}'_{WG} \left(w, \frac{3L_\pi}{2} \right) \quad (2.36)$$

with $w = 1.34 \mu\text{m}$ and $L_\pi = 409.2 \mu\text{m}$ as before. The two section design can sustain around 130 nm of waveguide width deviation to operate above 20 dB PER. This is a more than twofold improvement over the one section design (56 nm), but still impractical for contact lithography, which can deviate from the design by up to $\pm 100 \text{ nm}$ (including etch variations). Another issue that has not been tackled yet is the insertion loss of the device.

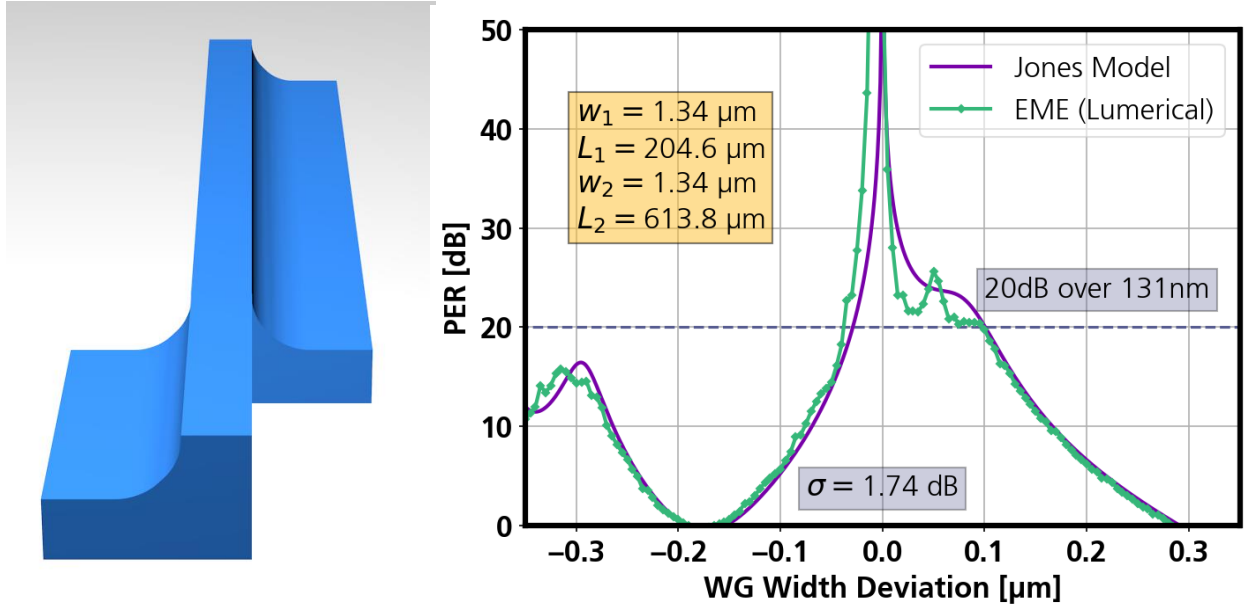


Figure 2-11. Left: Rendered 3D cartoon of the two-section polarization converter based on the asymmetric waveguide as discussed in chapter 2.4.3. Right: dependence of the PER on the waveguide width deviation from the ideal width of 1.34 μm . The dependence is calculated using Lumerical's EME solver as well as the Jones model. For 20 dB of PER, the width deviation has to be below 131 nm. The average deviation between the two curves is 1.7 dB. The insertion loss in Lumerical is 0.8 dB.

2.5.3 Transitions between Waveguides

2.5.3.1 Interface between Asymmetric and Symmetric Waveguides

For application of the device in a PIC, it has to be connected to regular (symmetric) waveguides, in particular the one from chapter 2.4.2. Due to the different mode profiles and the resulting non-ideal mode overlaps, this interface is associated with optical loss. A correct lateral offset has to be used at the interface in order to optimize mode overlap. In addition, the modes in the two mirrored sections have mirrored profiles. Since the mode profiles are asymmetric (even if just slightly, see figure 2-7), they will also not perfectly overlap. Hence, the interface between the two asymmetric sections will exhibit loss too. Again, the correct lateral offset is necessary for optimum coupling between the two asymmetric sections.

First, the interface between symmetric and asymmetric waveguide is considered. The key parameter is the mode overlap, since it determines the transmission from one mode into the other. The transmissions S_{21} from the symmetric waveguide modes into the asymmetric waveguide modes are defined such that they reflect the transmission for the TE and TM polarizations:

$$\begin{aligned} S_{21,TE} &= \text{overlap}(\text{symmetric}_{TE}, \text{asymmetric}_0) + \text{overlap}(\text{symmetric}_{TE}, \text{asymmetric}_1) \\ S_{21,TM} &= \text{overlap}(\text{symmetric}_{TM}, \text{asymmetric}_0) + \text{overlap}(\text{symmetric}_{TM}, \text{asymmetric}_1) \end{aligned} \quad (2.37)$$

This quantity can be computed in MODE using pre-built functions that write as:

$$\text{overlap}(WG1_{i\text{-th mode}}, WG2_{j\text{-th mode}}) = \left| \frac{\text{Re} \left[\frac{(\int E_{WG1,i\text{-th mode}} \times H_{WG2,j\text{-th mode}}^*) (\int E_{WG2,j\text{-th mode}} \times H_{WG1,i\text{-th mode}}^*)}{\int E_{WG1,i\text{-th mode}} \times H_{WG1,i\text{-th mode}}^*} \right]}{\text{Re}[\int E_{WG2,j\text{-th mode}} \times H_{WG2,j\text{-th mode}}^*]} \right| \quad (2.38)$$

The results of the mode overlap calculations are summarized in figure 2-12. We find that optimum coupling is given when the widths at the interface obey $\text{width}_{\text{asymm}} = 0.96\text{width}_{\text{symm}} - 20 \text{ nm}$ with a lateral offset of -100 nm. We choose widths of the symmetric and asymmetric waveguides of 3.5 μm and 3.34 μm , respectively. This then gives $S_{21}=0.015 \text{ dB}$, with negligible polarization dependence.

With the results from figure 2-12, it becomes clear that the simple designs from chapters 2.5.1 and 2.5.2 will be non-ideal with respect to loss. Wider asymmetric waveguides, however, lose their modal tilt θ . To make use of the more advantageous wider waveguide interfaces, while still exploiting the asymmetric waveguide in a strongly tilted regime, tapers become necessary. On the other hand, tapers break the design flow for the one- and two-section devices that were discussed so far. Since tapers introduce a modal tilt $\theta(z)$ that is not constant and certainly not 45° , the operation principle becomes problematic. We discuss how to design working devices with $\theta \neq 45^\circ$ and even $\theta(z) \neq \text{const}$ in chapter 2.5.4. First, the actual tapers have to be simulated and designed.

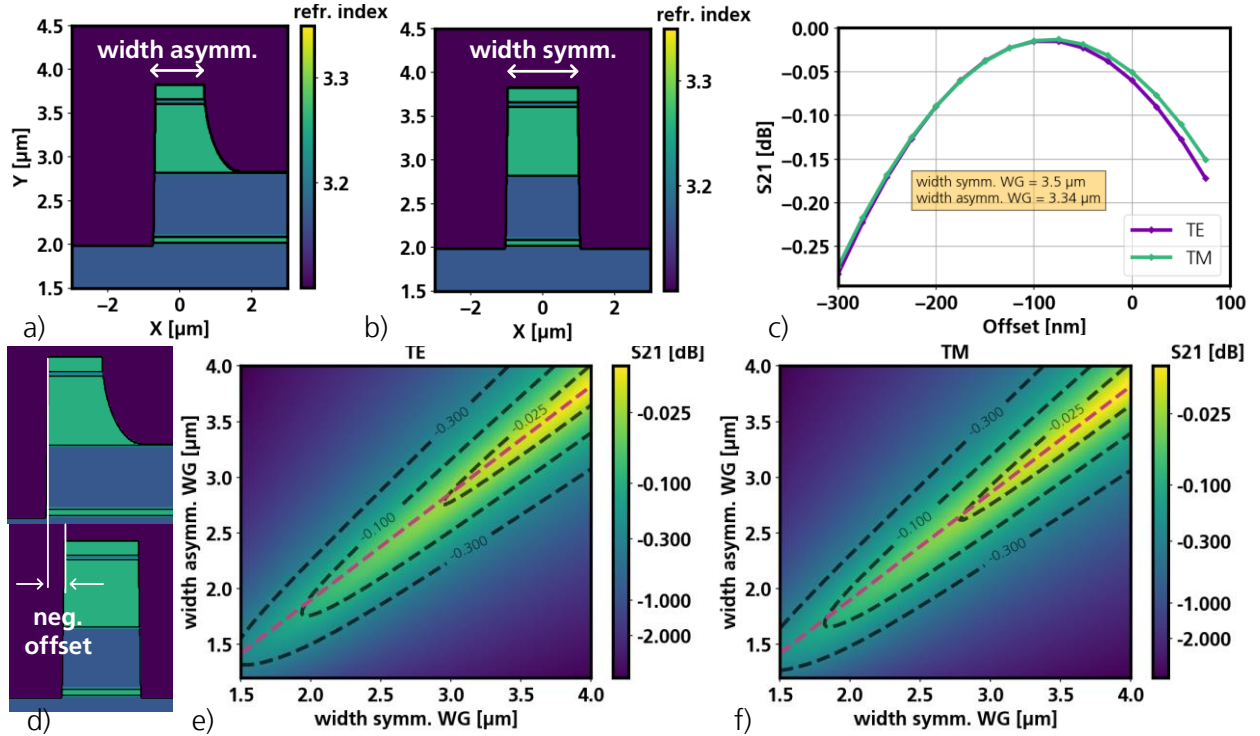


Figure 2-12. Investigation of the coupling efficiency from the asymmetric (a) to the symmetric (b) waveguide. S_{21} is calculated for widths ranging from 1.5 μm to 4.0 μm in 20 nm increments for both waveguides. At each combination of the two widths, lateral offsets along the x-axis ranging from -300 nm to 100 nm are computed in 25 nm increments (c) for a particular combination of widths. An exaggerated illustration of a negative offset is shown in d). S_{21} is maximum for an offset of -100 nm for all width combinations that are along the pink line in the two bottom colormaps. e) and f) show the dependence of S_{21} versus the two

waveguides' width. The inset pink line is a linear fit through the width combinations that yield the highest S_{21} . It is the same for TE and TM and follows $width_{asymm} = 0.96width_{symm} - 20 \text{ nm}$.

Since simulating the tapers requires accurate modelling of the light propagation, Lumerical's FDTD [41] package is used. The results are shown in figure 2-13. With this, a choice for the taper parameters is made: 100 μm long tapers on both sides of the interface leading up to it the transition. On the symmetric side, the interface width is 3.34 μm , on the asymmetric side it is 3.5 μm .

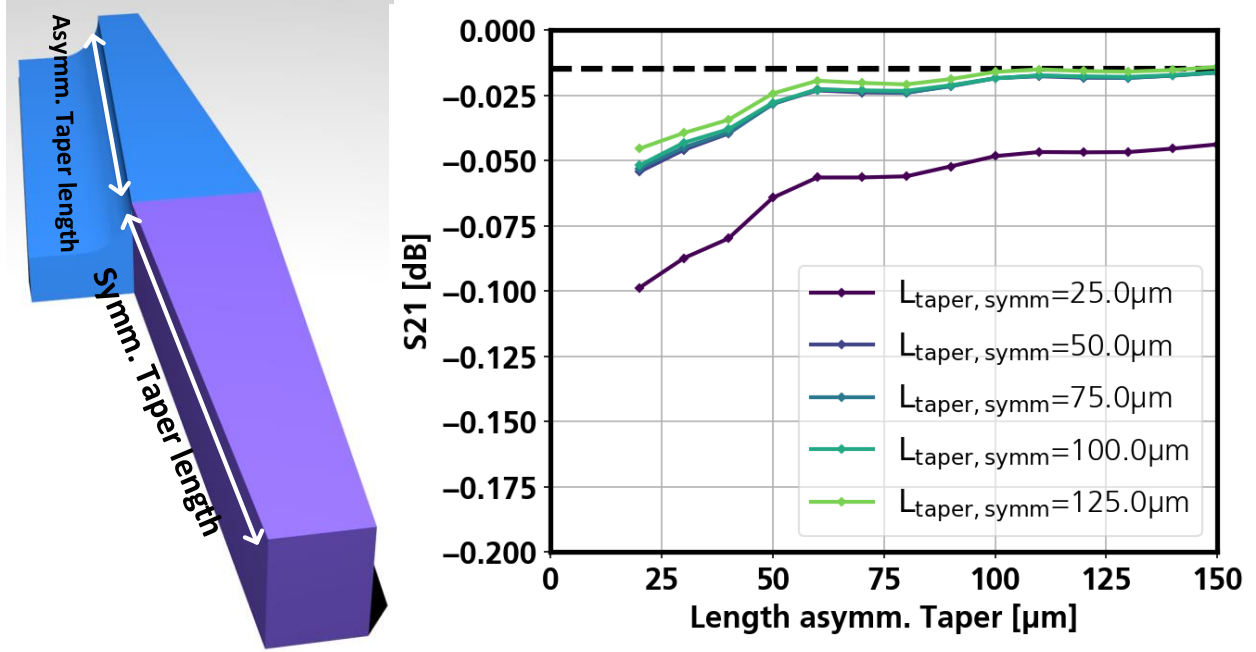


Figure 2-13. FDTD simulations of the tapered transition between symmetric and asymmetric waveguide (see cartoon on the left). The transmission is plotted (right) for a wavelength of 1.55 μm . The widths at the interface are 3.5 μm for the symmetric and 3.34 μm for the asymmetric waveguide, respectively. The starting widths are 1.3 μm for the asymmetric and 2.0 μm for the symmetric waveguide, respectively. The dashed line at 0.015 dB indicates the pure mode overlap at the interface, which is the upper limit for the taper transmission. Making either of the sections longer than 100 μm has negligible impact on the overall transmission.

2.5.3.2 Interface Between two Mirrored Asymmetric Sections

For a two-section design, the interface between the two asymmetric waveguides is also important. Like in the previous chapter, tapered transitions reduce the loss significantly. This adds more flexibility to the polarization converter design: when the two sections are joined by tapered transitions, they do not necessarily have to be of the same width. Without tapers, unequal widths would increase the loss due to mode mismatch. Using the same methodology as previously in 2.5.3.1, a summary of the simulations of the asymmetric-asymmetric interface is presented in figure 2-14. The optimal lateral offset is exactly twice the offset of the symmetric-asymmetric case, i.e. 200 nm.

It can be seen that in the absence of a tapered transition and an asymmetric waveguide width of 1.3 μm , the interface gives around 0.3 dB loss even at optimum offset. When moving to tapered transitions, however, the choice of parameters is constrained by the

overall performance of the polarization converter. As will be seen in the next chapter, a taper that is too long degrades the performance of the overall design. Therefore, the length of the transitions is limited to two tapers with 25 μm each. With figure 2-15, the width at the interface is then chosen to be 2.5 μm , giving around 0.05 dB total loss for this transition.

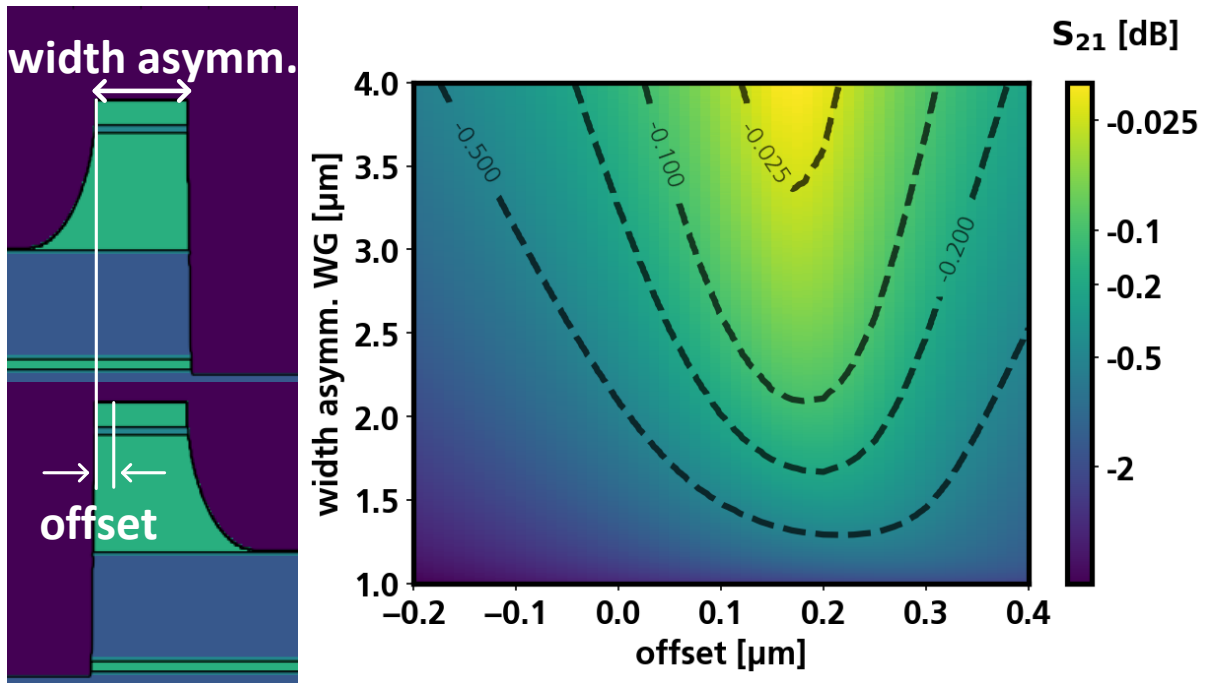


Figure 2-14. Investigation of the coupling efficiency between two mirrored asymmetric waveguides (as shown on the left). The colormap (right) shows S_{21} for different waveguide widths and lateral offsets. The two mirrored waveguides always have the same width.

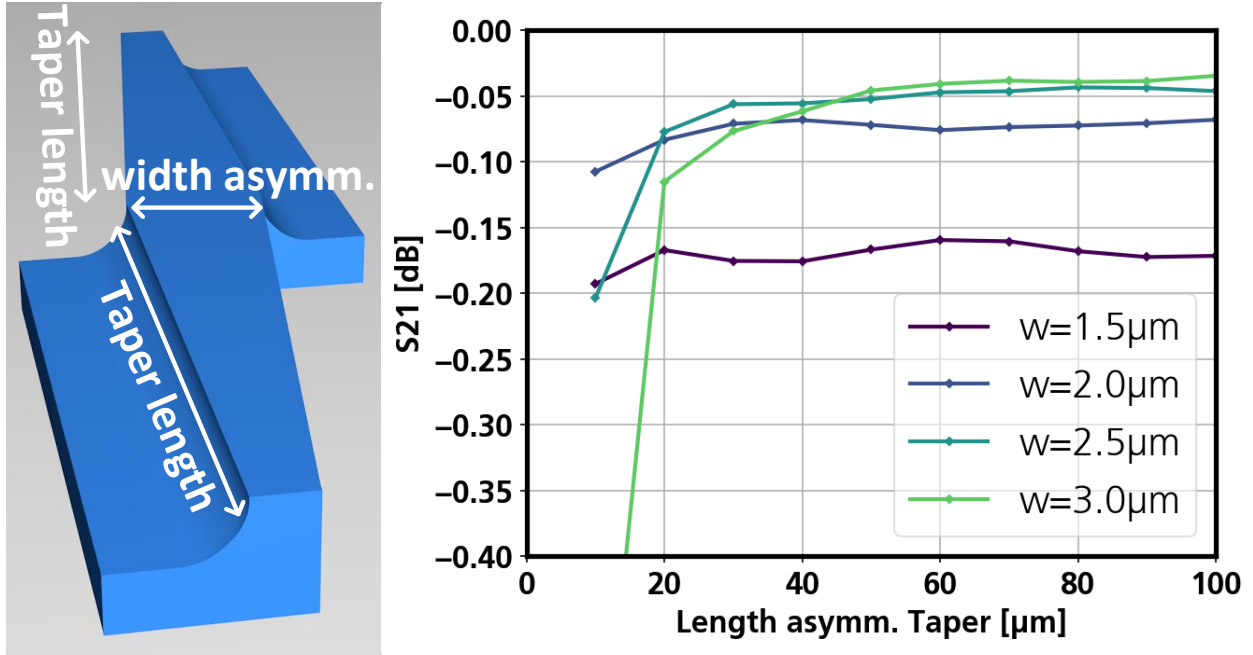


Figure 2-15. FDTD Simulations of the transmission from one tapered asymmetric waveguide into its mirrored counterpart. For different lengths, there are different optimum interface widths. Lowest loss is given by long tapers with wide interfaces. If one wishes to constrain the taper length, however, the interface width should not be too wide.

2.5.4 Design Optimization

2.5.4.1 Two Section Design without Tapers

With the results of the chapters 2.5.3.1 and 2.5.3.2, the goal is to design a polarization converter that has minimal excess loss. This requires waveguides much wider than what gives $\theta = 45^\circ$. At the same time, even the two-section design from 2.5.2 is very hard to fabricate with the process variations that occur in HHI's photonic integration technology. A new concept is therefore needed, to achieve polarization conversion with $\theta(z) \neq \text{const}$ and in particular $\theta(z) \neq 45^\circ$. A first step is to consider a two-section device with different waveguide widths $w_1 \neq w_2$ in the two sections (each of lengths $L_1 \neq L_2$). If we further neglect any tapered transitions and loss, the Jones Matrix of the complete device writes as:

$$\underline{J}_{PC} = \underline{J}_{WG}(w_1, L_1) \cdot \underline{J}'_{WG}(w_2, L_2) \stackrel{!}{=} \begin{pmatrix} 0 & 1 \\ 1 & 0 \end{pmatrix} \quad (2.39)$$

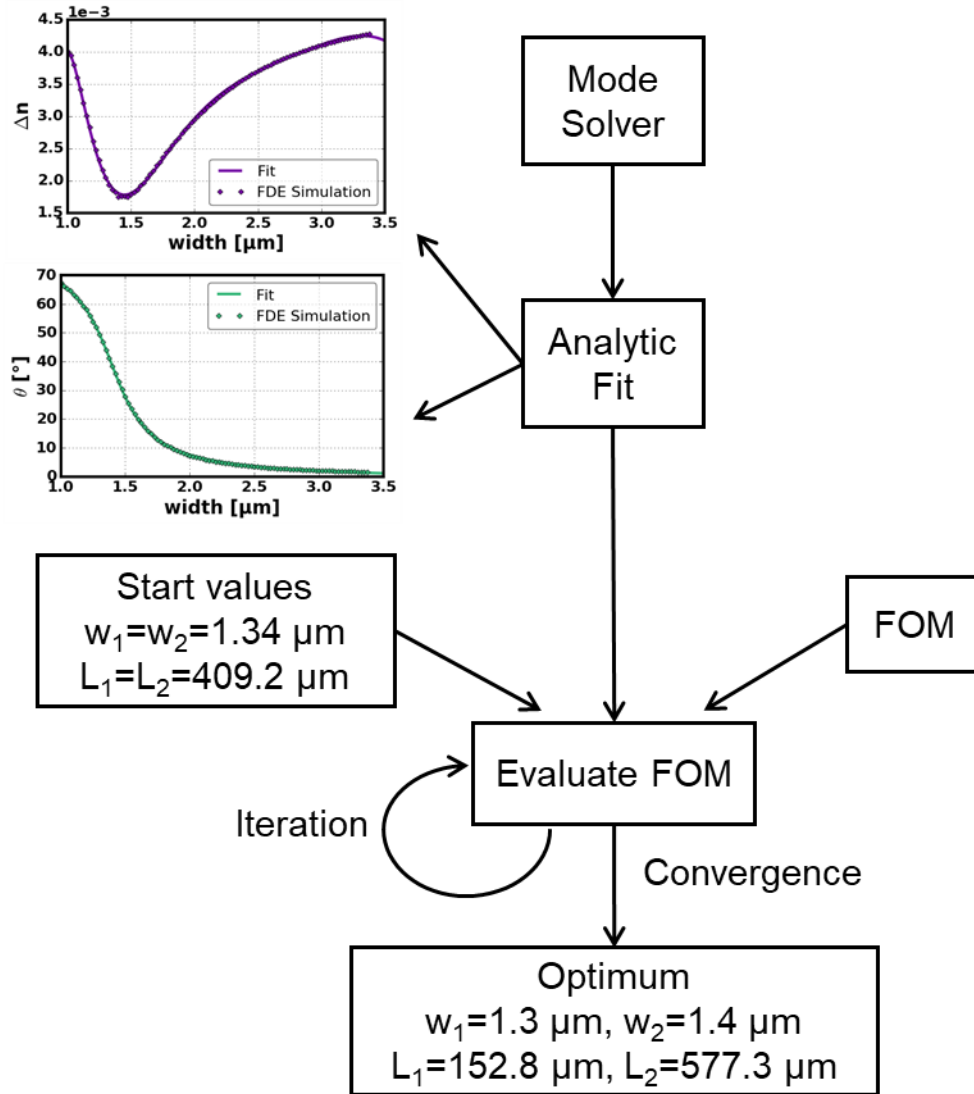


Figure 2-16. Flow diagram of the numerical design optimization. The fit formulas (2.30) and (2.31) for Δn and θ versus width together with $\delta = \frac{\Delta n L}{\lambda}$ define the behavior of a device in terms of its section widths and lengths. A python script runs an optimization of this dependency to find the device with the highest PER across a given width deviation $2\Delta w$. The output are the numerical values of the two widths and two lengths of the respective sections.

To find an (approximate) solution to (2.39), it is numerically implemented in python [48]. Python is a scripting language that comes with many extensions that are useful for scientific computing [49]. A flow diagram of the functionality of the python model is in figure 2-16. In this model, all the relevant dependencies like (2.30) and (2.31) are included. The result is a function that computes $J_{PC}(w_1, L_1, w_2, L_2)$. To perform optimization of the process tolerance, a target function is defined that should be minimized. The target function f of a given device $J_{PC}(w_1, L_1, w_2, L_2)$ is defined as:

$$f(w_1, L_1, w_2, L_2) = \sum_{\Delta w = -\Delta w_{max}}^{\Delta w_{max}} Err(w_1 + \Delta w, L_1, w_2 + \Delta w, L_2) \quad (2.40)$$

The error function Err gives a quantitative measure of how much polarization is converted by the device:

$$Err(w_1 + \Delta w, L_1, w_2 + \Delta w, L_2) = |j_{out,2}| \quad (2.41)$$

with

$$\vec{J}_{out} = \underline{J}_{PC} \cdot \vec{J}_X = \underline{J}_{PC} \cdot \begin{pmatrix} 1 \\ 0 \end{pmatrix} \quad (2.42)$$

An ideal polarization converter will transfer all energy from the first Jones' element to the second. Then, if the converter does not exhibit any fabrication error, $\Delta w = 0$ and $Err = 0$. For $\Delta w \neq 0$, Err will generally grow. The faster it grows, the less fabrication errors can be sustained before the PER suffers. This is expressed in large values for f . So, the goal becomes to find the minimum value for f in the (w_1, L_1, w_2, L_2) space.

Python's SciPy package offers a whole library to tackle minimization problems of scalar functions like f . For the following calculations, the Nelder-Mead method is used [50]. The result of the optimization when optimizing across $2\Delta w = 250$ nm is given in figure 2-17. The entire optimization takes less than seven seconds. During the optimization process, 801 different device designs are calculated. For each design, 20 different width deviations are evaluated to calculate the tolerance. With the EME solver on the other hand, just calculating the tolerance of the single optimal design takes over two hours with a granularity of 140 different width deviations. Hence, the Jones model is almost 10,000 times faster. figure 2-18 shows how well the design matches EME simulations.

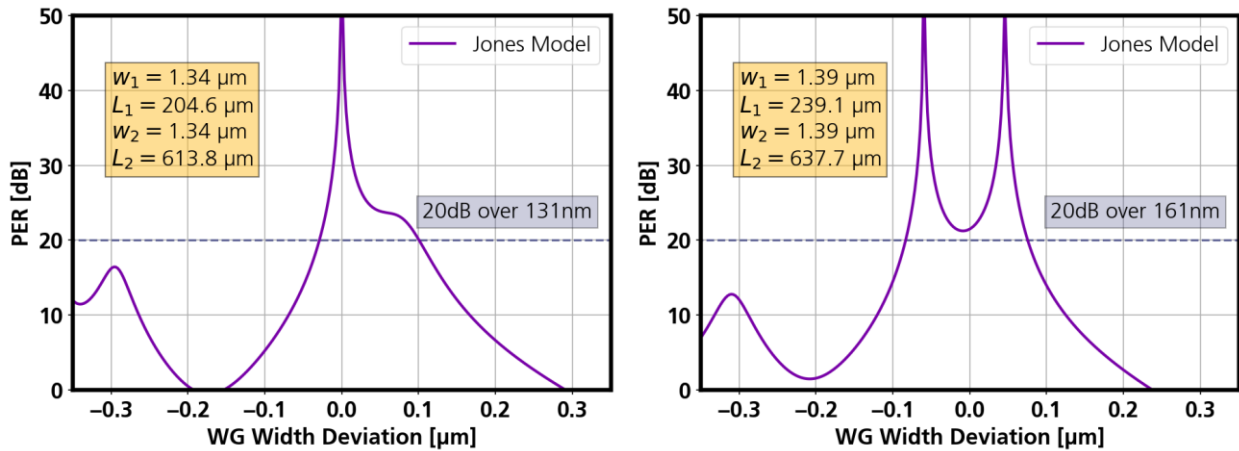


Figure 2-17. Left: Result of the optimization implemented using scipy. The target function (2.40) is evaluated up to $\Delta w_{max} = 125$ nm. The optimized parameters are in the yellow inset. 20 dB PER are maintained across width deviations of up to 177 nm. The widths of the short and long sections correspond to $\theta_1 = 38^\circ$ and $\theta_2 = 40^\circ$, respectively. On the right is the two-section design from 2.5.2 that can sustain 135 nm of width deviation. For the optimized design, the two sections are not of equal width and also some 50 nm wider than in the design that uses $\theta_1 = \theta_2 = 45^\circ$. It has 0.7 dB loss (the un-optimized design has 0.8 dB).

A direct comparison between the two designs ($\theta \neq 45^\circ$ and $\theta = 45^\circ$) shows clear advantages for the optimized design. Across ± 100 nm of width deviation, the optimized design has 4 dB higher average PER (25.2 versus 21.4 dB). Because the waveguides are wider and the mode overlaps are higher for wider waveguides, the loss is also slightly lower (0.7 versus 0.8 dB). Most importantly, the optimized design is the proof that designs with $\theta \neq 45^\circ$ exist at all. It should therefore be possible to achieve similar PER values with tapered designs. As was shown in section 2.5.3, this can severely reduce the insertion loss.

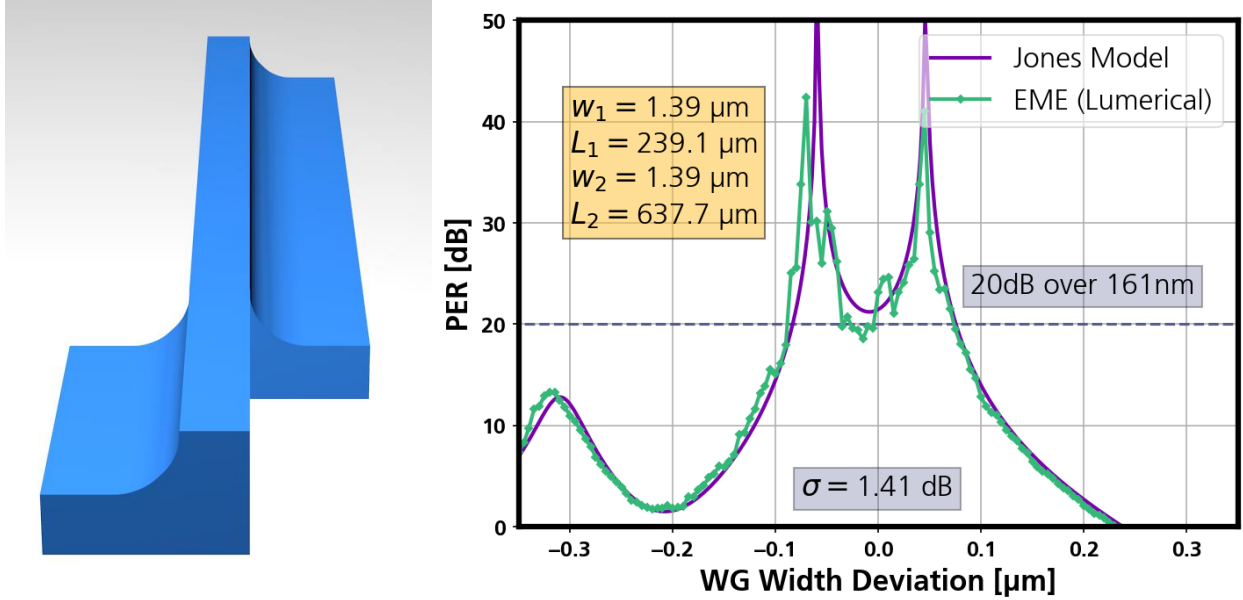


Figure 2-18. Comparison of the predictions of the Jones Model and the EME solver. The standard deviation of around 1.4 dB in PER indicates that the Jones Model also works for devices operating with $\theta \neq 45^\circ$. The calculation of the 300 points in the Jones curve takes 200 msec on a personal computer. The 140 EME simulations for the other curve take over around 140 minutes on the same machine.

The deviations between Jones model and eigenmode expansion in figure 2-18 amount to an average of around 1.5 dB PER. This can be explained by the fact that the x- and y-components of the mode fields are not homogeneously distributed. In particular, the quantities $\frac{E_x}{E_x + E_y}$ and $\frac{E_y}{E_x + E_y}$ are not constant across the mode. This will generally lead to coupling between the modes at waveguide interfaces that differs from the case of completely homogenous mode distributions. But since Jones matrices rely on plane waves, they can not reflect this inhomogeneity.

2.5.4.2 Two Section Design with Tapers

To take advantage of the considerations in 2.5.3, the Jones model needs adaptation. It is clear that the overall loss can be significantly reduced by using tapers. The impact on the actual polarization conversion is unclear, though. Since both δ and θ change along z , they cannot be described by a simple matrix as (2.32). To analyze the achievable conversion with tapered sections, they are modelled as a series of discrete elements as (2.32), and then the matrix product of all elements gives the taper matrix. Figure 2-19 shows the

convergence of the effective taper matrix versus the number of discretization steps. We will use five discrete sections in the following to model the tapers.

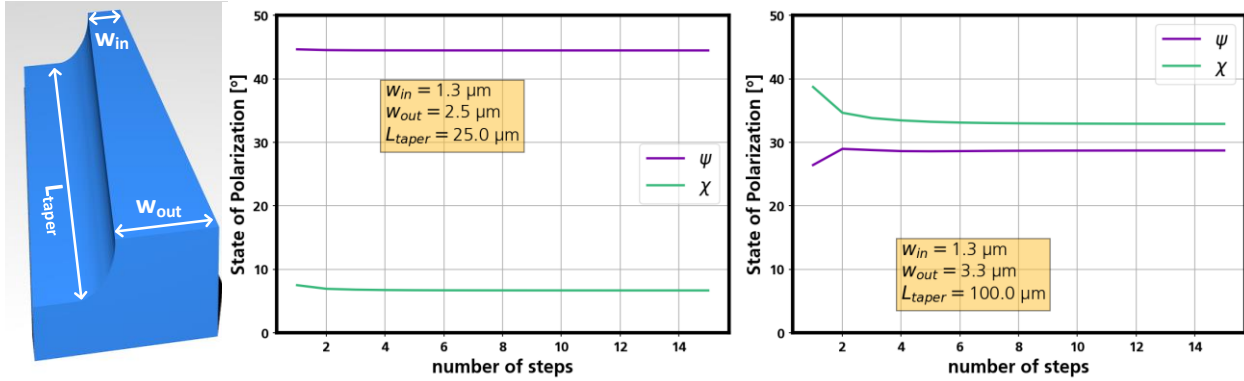


Figure 2-19. Convergence of polarization evolution versus taper discretization. The input polarization is linearly polarized at 45° , i.e. $\psi = 45^\circ$ and $\chi = 0^\circ$. The two taper variants are the ones that are relevant for the tapered polarization converter design. The predicted output polarization converges for both variants.

With the results from chapter 2.5.3, a set of taper parameters at the in- and outputs of the PR is chosen: widths of $3.34 \mu\text{m}$ and $3.5 \mu\text{m}$ for the asymmetric and symmetric waveguide, respectively. The length for each tapered waveguide is $100 \mu\text{m}$. With these parameters fixed, the length of the middle interface (asymmetric-asymmetric) is investigated. For low loss, a longer taper is desirable. As can be seen in figure 2-20, however, the length of this taper impacts the PER performance of the optimum design. Therefore, the middle taper length is restricted to $25 \mu\text{m}$ in length. For this length, the lowest loss is achieved with an interface width of $2.5 \mu\text{m}$. This choice acts as a boundary condition for the optimization of the actual design and the values are summarized and illustrated in figure 2-20. These parameters will give $2 \times 0.015 \text{ dB}$ loss for the asymmetric-symmetric interfaces and 0.07 dB for the symmetric-symmetric interface, so 0.1 dB total loss due to the transitions. This is a eight-fold reduction compared to the $2 \times 0.25 \text{ dB}$ plus 0.3 dB in the absence of tapers.

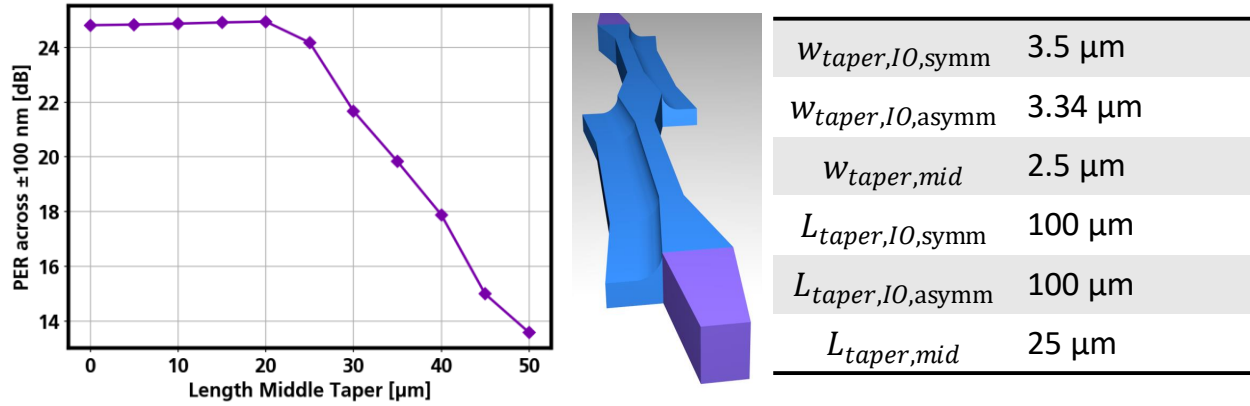


Figure 2-20. Left: dependence of the PER of the optimal PR versus the middle taper length. Beyond 25 μm taper length, the PR performance becomes worse than a non-tapered design. The tapered PR is rendered in the center (not to scale). The parameters for the tapered PR design are summarized in the right table.

With the choice of taper parameters, an optimal rotator design is derived. The optimization takes some 10 seconds on a personal computer, i.e. around one order of magnitude longer than the non-tapered optimizations. This is a natural consequence from the additional Jones matrices that are computed for each discretized taper element. The final design and its tolerance are given in figure 2-21.

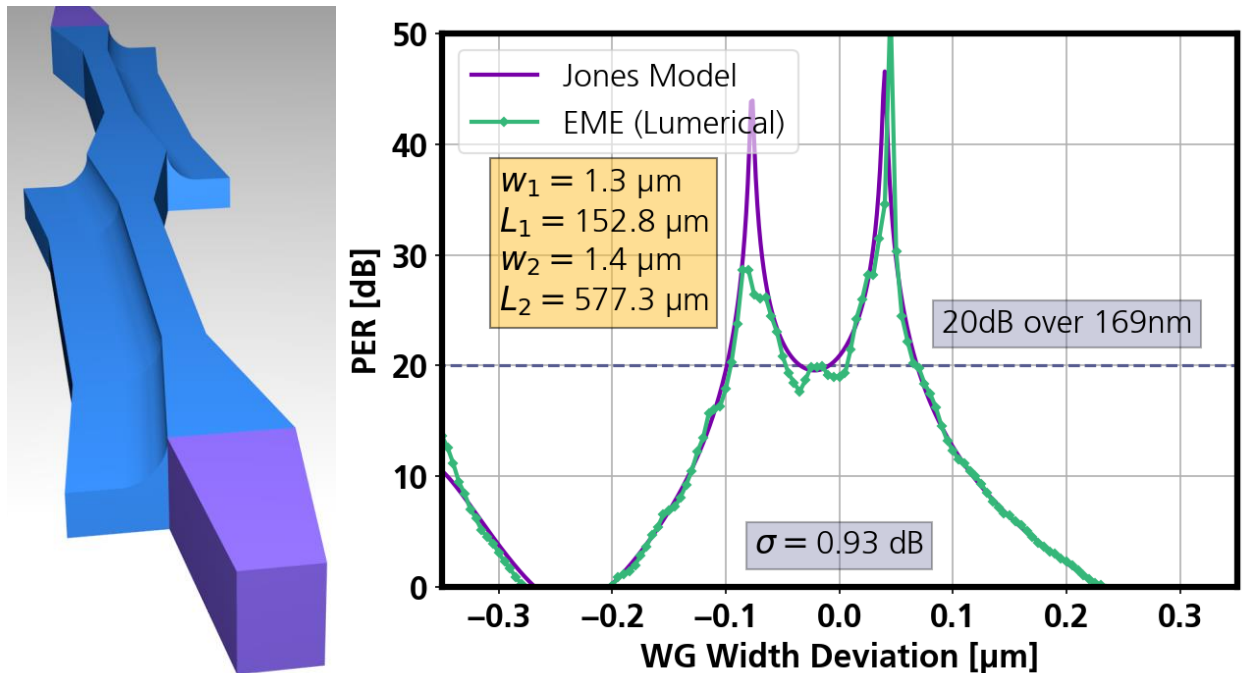


Figure 2-21. Comparison of the predictions of the Jones Model and the EME solver. The design is numerically optimized and comprises tapered transitions at all junctions. The average deviation between Jones Model and Lumerical is less than 1 dB. The calculation of the 300 points in the Jones curve takes 200 msec on a personal computer. The 140 EME simulations for the other curve take over around 140 minutes on the same machine. The device exhibits 0.1 dB loss.

2.5.5 Discussion of Final Design

The performance of the final design from section 2.5.4.2 is summarized in Table 1. To easily compare it with the other designs, a figure of merit (FOM) is defined. For each design, the average PER_{av} across a width deviation of ± 100 nm is calculated. Together with the insertion loss, we then define:

$$FOM = \frac{PER_{av}}{loss} \quad (2.43)$$

Using this measure, the untapered design operating at $\theta \neq 45^\circ$ gives a 30% improvement over the $\theta = 45^\circ$ design from literature. The final tapered design gives a 800% improvement, mostly due to the achieved loss reduction.

Design	20 dB tolerance [nm]	Mean PER for ± 100 nm [dB]	Loss [dB]	Mean PER / Loss
1 Section reference (see 2.5.1)	56	15.5	0.6	26
2 Section reference (see 2.5.2)	131	21.4	0.8	27
2 Section Jones-Optimized (see 2.5.4.1)	161	25.2	0.7	35
2 Section Tapered Jones-Optimized (see 2.5.4.2)	168	24.3	0.1	243

Table 1. Performance comparison of different PR designs. The figure of merit is the average PER across ± 100 nm of width deviation over insertion loss. The Jones-based optimization gives a 30% improvement for a 2-section design without tapered transitions. With tapered transitions, another 590% are achieved, or 800% in total. The tapered design is the final PR design.

To further estimate the manufacturability of the final design, its dependence on parameters other than waveguide width is analyzed: waveguide core thickness, waveguide core composition and photon wavelength.

HHI's epitaxial layers are specified with ± 10 nm error for the photoluminescence, which is an effective measure for the accuracy of the layers' composition. The thickness variation is around $\pm 5\%$. As can be seen in figure 2-22, the PER stays above 15 dB within the epitaxial accuracy in the case of no width deviation.

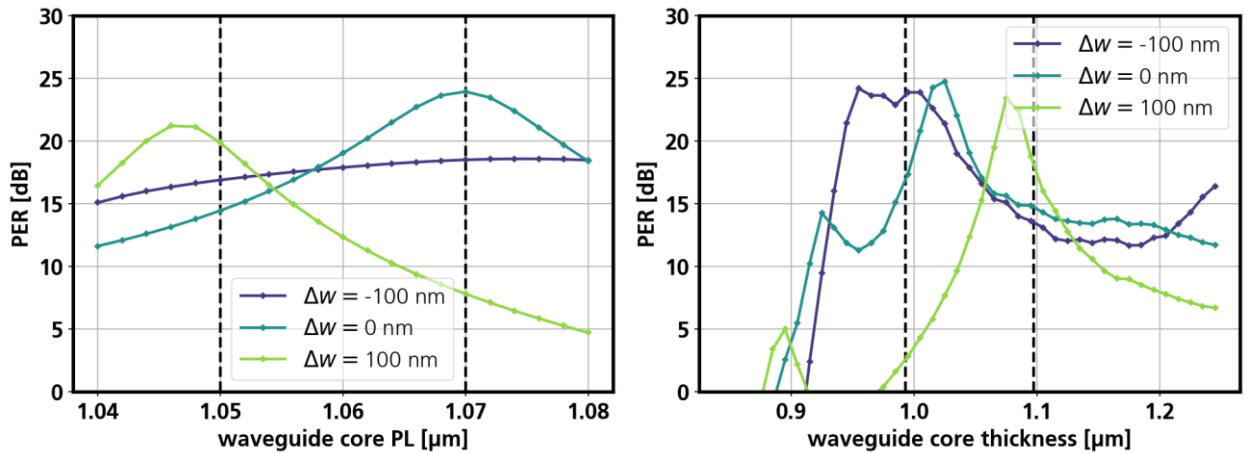


Figure 2-22. PER dependence on epitaxial errors of the waveguide core. Left: dependence on photoluminescence (PL). The core PL is specified by $1.06 \mu\text{m} \pm 10 \text{ nm}$. The specified deviation is indicated as dashed lines. Right: dependence on the core thickness, which is specified by $1.045 \mu\text{m} \pm 5\%$, again indicated by the dashed lines. Both plots show the behavior for width deviations of -100, 0 and 100 nm.

All previous calculations are done for a wavelength of $1.55 \mu\text{m}$. The mode solver model, however, includes proper material dispersion. Also, even in the absence of material dispersion, the modes' shape and therefore tilt and birefringence depend on wavelength. The impact of those circumstances is summarized in figure 2-23.

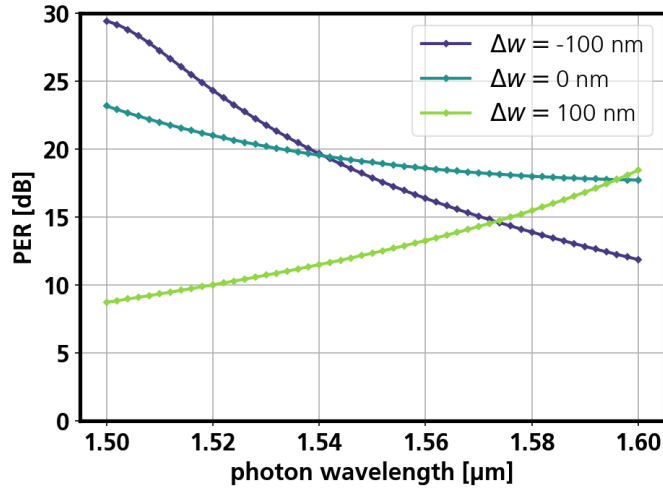


Figure 2-23. Wavelength dependence of the final design PER. The dependence is shown for width deviations of -100, 0 and 100 nm.

2.5.6 45° Polarization Rotators

So far, only devices that fully convert between TE and TM are considered. Because they rotate the respective polarizations by 90° , they are referred to as 90° PRs. For some applications however, it may be desirable to rotate polarization by only 45° . Effectively, this converts half the power from TE to TM and vice versa. Just as a 90° rotator can be thought of as a half waveplate under a 45° angle, a 45° rotator can be thought as a quarter waveplate under the same angle. We use the same design methodology as for the 90° rotators, but aim for 0 dB PER instead of maximum PER. Using the same taper configuration as in figure 2-20, a design is derived and shown in figure 2-24.

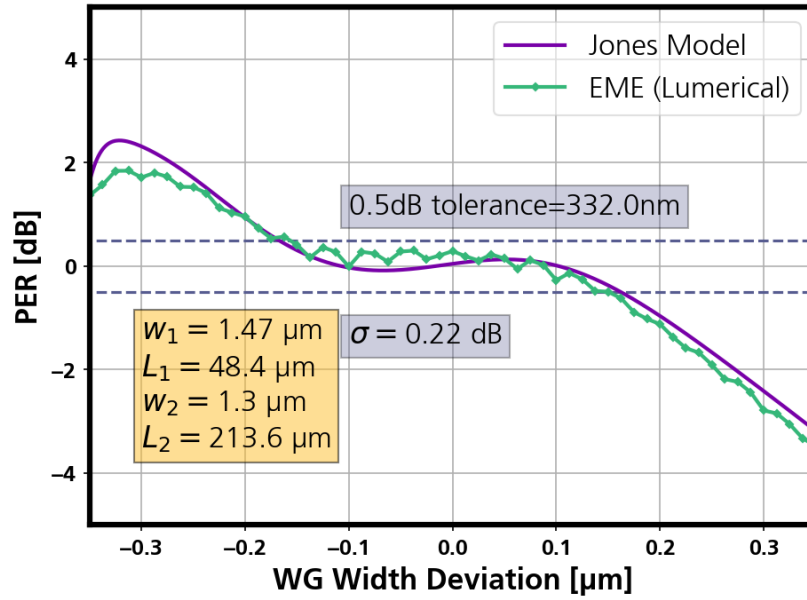


Figure 2-24. PER of a 45° polarization rotator according to the Jones model (purple) and Lumerical's MODE (green). It is a tapered design with the same taper parameters as the 90° rotator. The widths and lengths are given in the yellow inset. The average deviation between Jones and EME is 0.22 dB, the device operates within ± 0.5 dB PER across width deviations of 330 nm. The simulated insertion loss in MODE is 0.1 dB.

3 Transmitters and Receivers for PDM

3.1 iSTOMP: Stokes Space Receiver

With the previous chapter, a complete design methodology for arbitrary polarization rotators in planar integrated circuits is given. In this chapter, an application example that makes use of the rotators is discussed: iSTOMP (integrated STOKes MaPper). It is a PIC designed for the measurement of Stokes vectors.

As pointed out by Augustin in [51], polarization rotators can be placed in Mach-Zehnder interferometers (MZI) to yield polarization beam splitters (PBS). The basic concept is illustrated in figure 3-1. In a DD scheme, however, a PBS does not enable the retrieval of the input state of polarization. The information on the relative phase between X and Y polarization is lost. To overcome this limitation, the classical 2-arm MZI configuration is expanded to an N-arm configuration in this chapter. The device also has N outputs, each of which the power is to be measured. The following will show how the Stokes vector of incident light can be deduced from the powers exiting the device and what N needs to be.



Figure 3-1. 2-way Mach-Zehnder configuration for polarization beam splitting as proposed by Augustin [51]. The blue waveguides in the MZI are birefringent, so that the relative position of the two PRs changes the overall interference condition for TE and TM light. By choosing the right position, the two output powers are proportional to the powers in the two input polarizations, respectively.

3.1.1 Mathematical Description

Since the device to be discussed is based on interference, it cannot be understood in the Stokes formalism but only in Jones terminology. To describe the interference of polarized waves, one may simply add the two corresponding Jones vectors. Consider a configuration as in figure 3-2, with light incident to the top waveguide on the left.

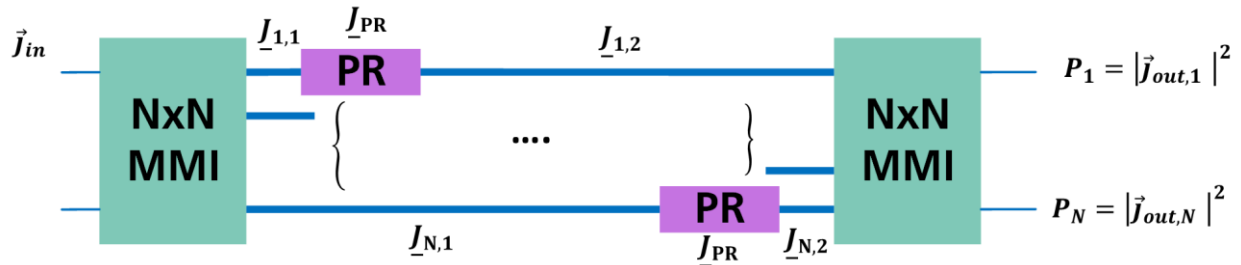


Figure 3-2. Schematic of the proposed receiver structure. An N-arm MZI is loaded with polarization rotators (PR) at different relative positions in each arm. Each arm has the same total length and each PR is equal. The N output powers can be described as the norms of the respective Jones vectors. The powers depend on the polarization at the input, i.e. \vec{J}_{in} .

The Jones vector at the i -th output is then given by:

$$\vec{J}_{out,i} = \left(\underline{J}_{MMI,1 \rightarrow i} \cdot \underline{J}_{1,2} \cdot \underline{J}_{PR} \cdot \underline{J}_{1,1} \cdot \underline{J}_{MMI,1 \rightarrow 1} + \dots + \underline{J}_{MMI,N \rightarrow i} \cdot \underline{J}_{N,2} \cdot \underline{J}_{PR} \cdot \underline{J}_{N,1} \cdot \underline{J}_{MMI,1 \rightarrow N} \right) \cdot \vec{J}_{in} \quad (3.1)$$

where $\underline{J}_{MMI,i \rightarrow j}$ denotes the Jones matrix describing the transfer from the i -th input to the j -th output of an MMI. The general phase relations ϕ_{ij} of a $N \times N$ MMI between i and j are given by Paiam et al. in [52]:

$$\phi_{ij} = \phi_1 - \frac{\pi}{2}(-1)^{i+j+N} + \frac{\pi}{4N} \left(i + j - i^2 - j^2 + (-1)^{i+j+N} \left(2ij - i - j + \frac{1}{2} \right) \right) \quad (3.2)$$

with some offset phase ϕ_1 which is given in [52]. Then, one can write:

$$\underline{J}_{MMI,i \rightarrow j} = \frac{e^{i\phi_{ij}}}{\sqrt{N}} \begin{pmatrix} 1 & 0 \\ 0 & 1 \end{pmatrix} \quad (3.3)$$

The $\underline{J}_{k,1}$ and $\underline{J}_{k,2}$ in the k -th arm are simple birefringent elements and therefore write as:

$$\underline{J}_{k,l} = \begin{pmatrix} e^{i\pi\delta_{k,l}} & 0 \\ 0 & e^{-i\pi\delta_{k,l}} \end{pmatrix} \quad (3.4)$$

We note that $\delta_{k,1} + \delta_{k,2} = \text{const}$ for all k . This is true because the total length of all arms is equal. Finally, the polarization rotator is

$$\underline{J}_{PR} = \underline{R}(\theta_{PR}) \cdot \underline{J}_{\delta_{PR}} \cdot \underline{R}(-\theta_{PR}) \quad (3.5)$$

with the definition for rotation as in section 2.2.2. We may write the total Jones matrix from the input to the i -th output as

$$\vec{J}_{out,i} = \underline{J}_i \cdot \vec{J}_{in}; \quad \underline{J}_i = \sum_{k=1}^N \underline{J}_{MMI,k \rightarrow i} \cdot \underline{J}_{k,2} \cdot \underline{J}_{PR} \cdot \underline{J}_{k,1} \cdot \underline{J}_{MMI,1 \rightarrow k} \quad (3.6)$$

So, we can write the powers exiting the device as

$$P_i = \left| \underline{J}_i \cdot \vec{J}_{in} \right|^2 \quad (3.7)$$

To continue, we encapsulate the elements of \underline{J}_i in parameters defined as

$$\begin{pmatrix} a_i & b_i \\ c_i & d_i \end{pmatrix} := \underline{J}_i \quad (3.8)$$

We can now analyze the powers further:

$$\begin{aligned} P_i &= \left| \underline{J}_i \cdot \vec{J}_{in} \right|^2 = |a_i E_x + b_i E_y|^2 + |c_i E_x + d_i E_y|^2 = |a_i E_x|^2 + |b_i E_y|^2 + a_i E_x \overline{b_i E_y} + \overline{a_i E_x} b_i E_y + \dots \\ &= |a_i E_x|^2 + |b_i E_y|^2 + 2\text{Re}\{a_i E_x \overline{b_i E_y}\} + |c_i E_x|^2 + |d_i E_y|^2 + 2\text{Re}\{c_i E_x \overline{d_i E_y}\} \end{aligned} \quad (3.9)$$

We define $\epsilon_{i,1} := \arg\{a_i \overline{b_i}\}$ and $\epsilon_{i,2} := \arg\{c_i \overline{d_i}\}$ and recall $\text{Re}\{z\} = |z|\cos(\arg\{z\})$ as well as $\arg\{z + w\} = \arg\{z\} + \arg\{w\}$. The relative phase of the input polarization $\arg\left\{\frac{E_y}{E_x}\right\} = \phi$ is defined as before. Then:

$$P_i = |a_i E_x|^2 + |b_i E_y|^2 + 2|E_x E_y| |a_i b_i| \cos(\epsilon_1 - \phi) + |c_i E_x|^2 + |d_i E_y|^2 + 2|E_x E_y| |c_i d_i| \cos(\epsilon_2 - \phi) \quad (3.10)$$

We use $\cos(\alpha - \beta) = \cos(\alpha)\cos(\beta) + \sin(\alpha)\sin(\beta)$ and start regrouping:

$$\begin{aligned} P_i &= |a_i E_x|^2 + |b_i E_y|^2 + |c_i E_x|^2 + |d_i E_y|^2 + \\ &2|a_i b_i| |E_x E_y| (\cos(\epsilon_{i,1}) \cos(\phi) + \sin(\epsilon_{i,1}) \sin(\phi)) + 2|c_i d_i| |E_x E_y| (\cos(\epsilon_{i,2}) \cos(\phi) + \sin(\epsilon_{i,2}) \sin(\phi)) \\ &= (|E_x|^2 + |E_y|^2) \frac{(|a_i|^2 + |b_i|^2 + |c_i|^2 + |d_i|^2)}{2} + (|E_x|^2 - |E_y|^2) \frac{(|a_i|^2 - |b_i|^2 + |c_i|^2 - |d_i|^2)}{2} \\ &\quad + 2|E_x E_y| \cos(\phi) (|a_i b_i| \cos(\epsilon_{i,1}) + |c_i d_i| \cos(\epsilon_{i,2})) + 2|E_x E_y| \sin(\phi) (|a_i b_i| \sin(\epsilon_{i,1}) + |c_i d_i| \sin(\epsilon_{i,2})) \end{aligned} \quad (3.11)$$

This is the form needed to substitute the Stokes elements using (2.14):

$$\begin{aligned} P_i &= s_0 \frac{(|a_i|^2 + |b_i|^2 + |c_i|^2 + |d_i|^2)}{2} + s_1 \frac{(|a_i|^2 - |b_i|^2 + |c_i|^2 - |d_i|^2)}{2} + \\ &s_2 (|a_i b_i| \cos(\epsilon_{i,1}) + |c_i d_i| \cos(\epsilon_{i,2})) + s_3 (|a_i b_i| \sin(\epsilon_{i,1}) + |c_i d_i| \sin(\epsilon_{i,2})) \end{aligned} \quad (3.12)$$

So, we find that the output powers are linear in the incident Stokes vector. We may write the output powers in an N-vector that results from some linear operation \underline{Z} on the Stokes vector. The operation can be represented by an Nx4 matrix:

$$\begin{aligned} z_{i0} &= \frac{(|a_i|^2 + |b_i|^2 + |c_i|^2 + |d_i|^2)}{2}; \quad z_{i1} = \frac{(|a_i|^2 - |b_i|^2 + |c_i|^2 - |d_i|^2)}{2} \\ z_{i2} &= |a_i b_i| \cos(\epsilon_{i,1}) + |c_i d_i| \cos(\epsilon_{i,2}); \quad z_{i3} = |a_i b_i| \sin(\epsilon_{i,1}) + |c_i d_i| \sin(\epsilon_{i,2}) \\ \underline{Z} &= [z_{ij}] \end{aligned} \quad (3.13)$$

Then we may simply write:

$$\begin{pmatrix} P_1 \\ \dots \\ P_N \end{pmatrix} = \vec{P} = \underline{Z} \vec{s} \quad (3.14)$$

Finally, we take the (pseudo-) inverse \underline{Z}^{-1} :

$$\vec{s} = \underline{Z}^{-1} \vec{P} \quad (3.15)$$

If \underline{Z} is of rank 4, this equation opens the path to using the device as a polarimeter and/or Stokes space receiver. It enables the determination of any arbitrary input polarization by measuring the output powers. By measuring all four Stokes parameters, the device also measures the total power of the incident signal.

3.1.2 Numerical Analysis

A closed analytical description of the equations involved in the proposed polarimeter scheme is hardly possible. Numerically, however, \underline{Z} can be calculated. This is useful to study the conditions under which \underline{Z} is of rank 4 and the device is therefore fully functional and linear.

First, N has to be determined. Since \underline{Z} needs to be of rank 4, we immediately note that N should be at least 4. The equations of the previous chapter are implemented in python and parametrized as follows: the polarization rotator is characterized by its retardance δ_{PR} and rotation θ_{PR} . The total retardance in each arm of the MZI is denoted δ_{MZ} . The retardances

before and after the PR in the i -th arm are $\delta_{i,1}$ and $\delta_{i,2}$, respectively. They are written as $\delta_{i,1} = R_i \delta_{MZ}$ and $\delta_{i,2} = (1 - R_i) \delta_{MZ}$, so that each arm is fully characterized by only the ratio R_i of the lengths.

No set of parameters is found for $N < 5$ that yields a \underline{Z} of rank 4. For $N \geq 5$, however, many solutions exist. It is found that the rank of \underline{Z} only depends on the ratios R_i , not on the total birefringence δ_{MZ} or the polarization rotator parameters δ_{PR} and θ_{PR} . This is a rather striking result because the ratio of the length of two waveguides can be controlled with high accuracy. We find that for $N \geq 5$, the set of R_i needs to contain at least three different values, so that \underline{Z} is of rank 4. θ_{PR} must not be an integer multiple of $\frac{\pi}{2}$, i.e. the PR axes should not be aligned with the device substrate.

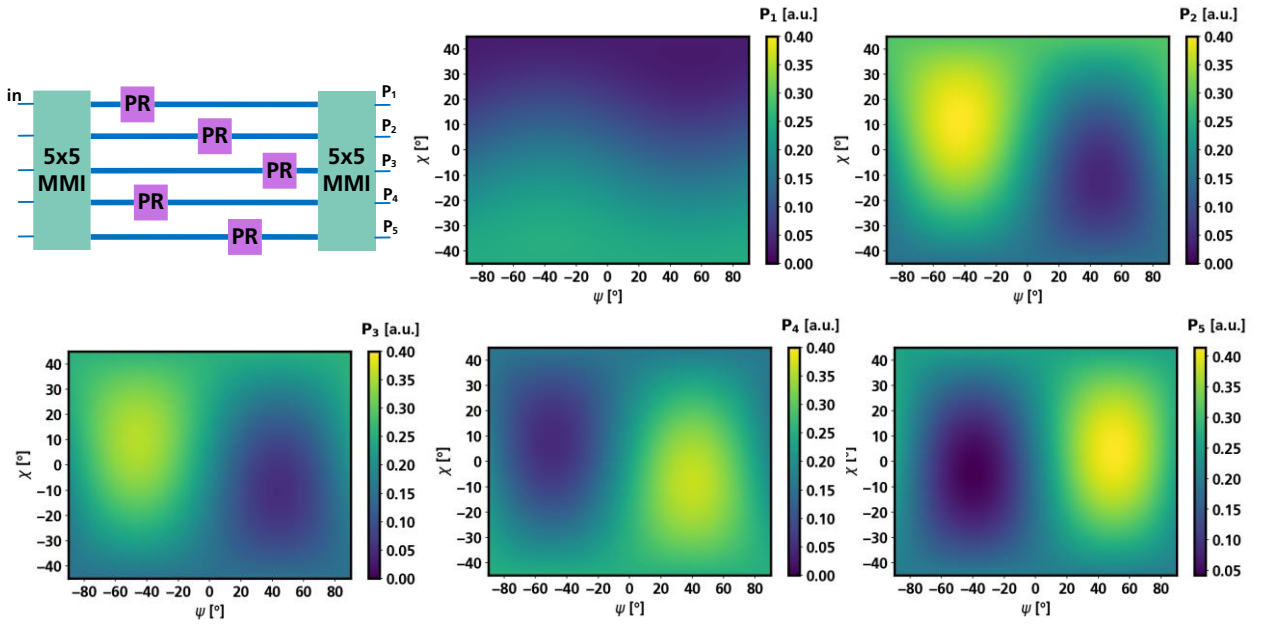


Figure 3-3. Working principle of the proposed Stokes receiver in the case $N=5$. The top left shows a cartoon of the receiver arrangement. The five plots show the dependence of the five output powers on the input polarization.

3.1.3 Geometrical Analysis

3.1.3.1 $N=3$

Even though for $N=3$ \underline{Z} is not of rank 4, there is still an interesting mapping between \vec{s} and \vec{P} that can be understood geometrically. Because $P_1 + P_2 + P_3 = \text{const}$ and $P_i > 0$, \vec{P} exists on an eighth of the surface of an octahedron, i.e. a triangle. Curiously, we find that the set of all \vec{P} is a smaller set than the triangle spanned by the octahedron. Rather, it exists on an ellipse within that triangle. The mapping for a particular MZI configuration is illustrated in figure 3-3. The mapping can be thought of as a projection of a 3D sphere onto a 2D plane. Since the depth information is lost this way, one cannot tell if the measured point corresponds to the front of the sphere or the back. Hence, each measurable point corresponds to two distinct polarizations. This is why \underline{Z} is not rank 4.

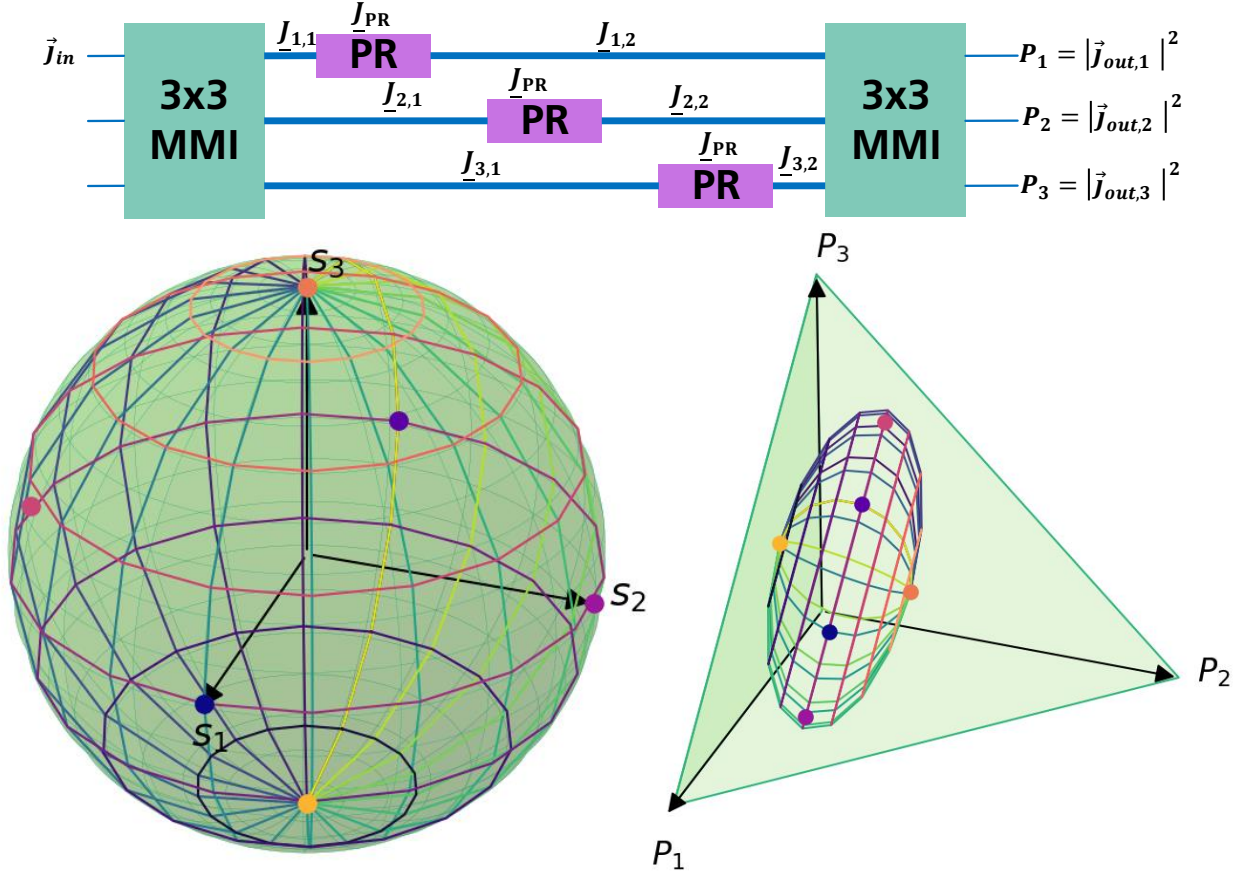


Figure 3-4. Geometrical interpretation of the working principle of a 3-arm iSTOMP. The PRs in each arm have $\delta_{PR} = \theta_{PR} = \pi/8$, the ratios are 0.25, 0.5, 0.75. The surface of the Poincaré sphere gets mapped to an ellipse in the space spanned by the three output powers. The ellipse itself exists on the triangular plane defined by $P_1 + P_2 + P_3 = 1$, i.e. the energy conservation condition (the input power is 1). The ellipse corresponds to the projection of the Poincaré sphere onto the triangle, viewed under some angle. Therefore, the 3-arm iSTOMP does not yield a bijection.

3.1.3.2 $N > 3$

To be able to visualize iSTOMP of full rank as the one in figure 3-3, the space of \vec{P} is inconvenient since it has five dimensions. To get around this, we take inspiration from the original definition for the Stokes vector. We recall that six powers define a Stokes vector \vec{s} , but the SOP can still be understood as a three dimensional point. We can define an analogous vector $\vec{\tilde{s}}$, whose elements are differences between the N powers P_i . A completely analogous example would be an iSTOMP with $N=6$ and the definition:

$$\vec{\tilde{s}} = \begin{pmatrix} \tilde{s}_0 \\ \tilde{s}_1 \\ \tilde{s}_2 \\ \tilde{s}_3 \end{pmatrix} = \begin{pmatrix} P_1 + P_2 + P_3 + P_4 + P_5 + P_6 \\ P_1 - P_2 \\ P_3 - P_4 \\ P_5 - P_6 \end{pmatrix} \quad (3.16)$$

We can generalize this expression using some $q_{k,i} \in [-1,1]$

$$\vec{s} = \begin{pmatrix} \sum_{i=1}^N P_i \\ \sum_{i=1}^N q_{1,i} P_i \\ \sum_{i=1}^N q_{2,i} P_i \\ \sum_{i=1}^N q_{3,i} P_i \end{pmatrix} \quad (3.17)$$

So, we can write this in matrix form using $\underline{Q} = [q_{k,i}]$, and we get:

$$\vec{s} = \underline{Q} \cdot \underline{Z} \vec{s} = \underline{\tilde{Z}} \vec{s} \quad (3.18)$$

Note that the first row of \underline{Q} only consists of ones. Further note that \underline{Q} is a 4xN matrix, while \underline{Z} is Nx4, so eq (3.18) can be written with a simple 4x4 matrix $\underline{\tilde{Z}} = \underline{Q} \cdot \underline{Z}$. The first row of $\underline{\tilde{Z}}$ is always $[1 \ 0 \ 0 \ 0]^T$. Because $\tilde{s}_0 = s_0$ is independent of the input SOP, the vector $[\tilde{s}_1 \ \tilde{s}_2 \ \tilde{s}_3]^T$ completely characterizes the incident SOP. In fact, $\underline{\tilde{Z}}$ is an affine map (p.38 in [53]). So, \vec{s} can be graphically understood in a similar way that SOPs can be understood as a point on a sphere. There are two major differences, however: the mapped affine surface is not a sphere but the surface of an ellipsoid. Second, the ellipsoid is generally not centered on the origin. \vec{s} is illustrated with the example of a 5-way iSTOMP in figure 3-5.

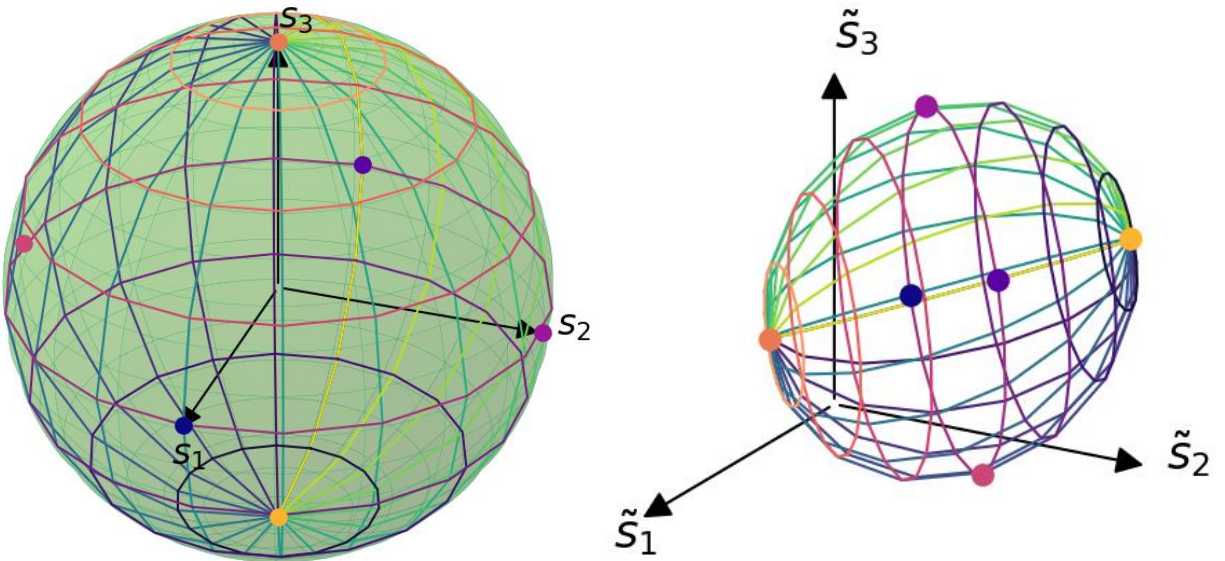


Figure 3-5. Illustration of the mapping between the Poincaré sphere (left) to the affine \vec{s} -space (right). The conjugate ellipsoid is centered around $[0.4 \ 0.6 \ 0.57]$ and has a volume that is 0.5% of that of the unity sphere (i.e. its axes are on average around 6.5 times shorter).

The \underline{Q} used for figure 3-5 is:

$$\underline{Q} = \begin{bmatrix} 1 & 1 & 1 & 1 & 1 \\ 1 & -1 & -1 & 1 & 1 \\ 1 & 1 & -1 & -1 & 1 \\ 1 & 1 & 1 & -1 & -1 \end{bmatrix} \quad (3.19)$$

To summarize, iSTOMPs with $N \geq 5$ enable the measurement of a Stokes vector. To maximize the signal-to-noise ratio (SNR), the volume of the mapping $\vec{s} = \underline{\tilde{Z}}\vec{s}$ should be as big as possible. The variable parameters to achieve this are: the total retardance in the MZI δ_{MZ} , the retardance and angle of the PR δ_{PR} and θ_{PR} and the ratios R_i . To implement iSTOMP designs in HHI's generic platform, MMI building blocks are still missing, as only 1x2 and 2x2 MMIs are available right now. Due to time constraints this has not been done.

3.2 Dual Polarization Electro-Absorption Modulators

3.2.1 A New DP Modulation Scheme

Since many practical electro-optical modulators have a strong polarization dependence, they are only operated with one particular polarization. For most devices in InP, TE polarization is used [9], [13], [54]. Almost all dual-polarization modulators found in literature use a configuration as in figure 3-6 ([13], [16], [19]). Incident light is split into two branches with a modulator in each. One of the modulated signals then is rotated in polarization, and the two paths are merged by a polarization beam combiner. Since in most cases only the two modulators are integrated and the other elements are implemented in bulk optics, the chips are often referred to twin-modulators ([19]). A fully integrated device has not been demonstrated in InP yet. Silicon-on-insulator (SOI) demonstrations exist, however ([16]).

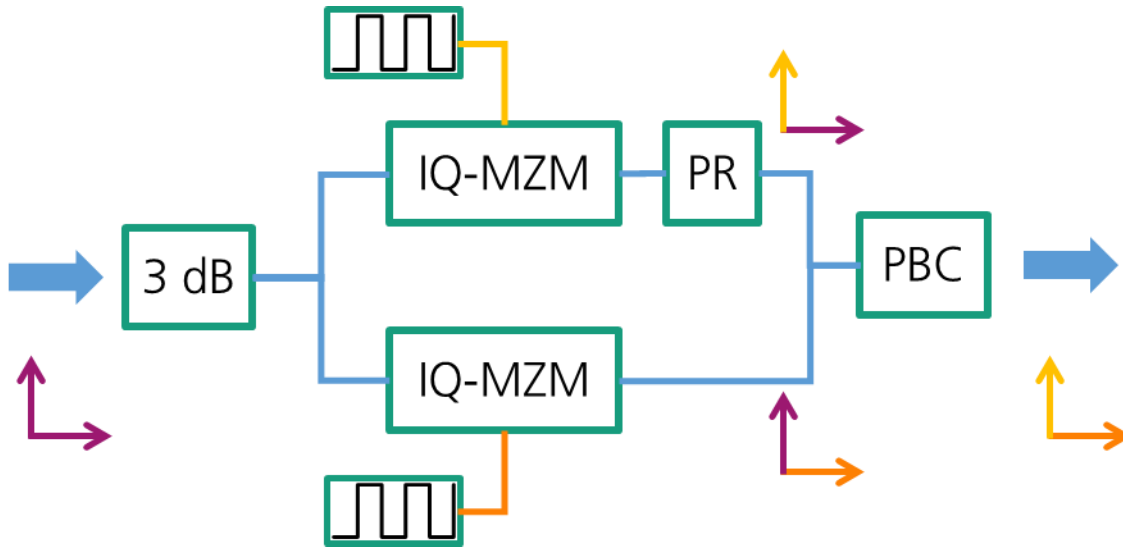


Figure 3-6. Classical scheme for dual-polarization modulation: the polarization diversity approach. Normally, it is implemented for coherent applications with two nested IQ modulators.

Even though normally implemented with IQ modulators, the polarization diversity scheme can also be used in direct detection systems. In those systems, however, modulation is often done by the laser directly (DML), or by electro-absorption modulators (EAM). These devices typically have a footprint one order of magnitude smaller than IQ modulators in the

same technology (compare e.g. [9] and [12]). This size advantage would at least partially be counteracted by the parallel nature of the polarization diversity scheme. Therefore, a new PDM scheme is proposed in figure 3-7. It makes use of the typically strong polarization dependence of electro-absorption modulators (EAM). Given that both EAMs only modulate TE and the PR rotates polarization by 90° , the working principle is as follows: light with both TE- and TM-components is launched into the device. The first EAM modulates only the TE component. The PR rotates the modulated signal into the TM state, while the unmodulated signal is rotated into the TE state. The second EAM will not affect the previously modulated signal, as it cannot interact with TM. Rather, its modulation is imprinted onto what is now TE. As a result, the optical signal leaving the second EAM is intensity modulated in both polarizations.

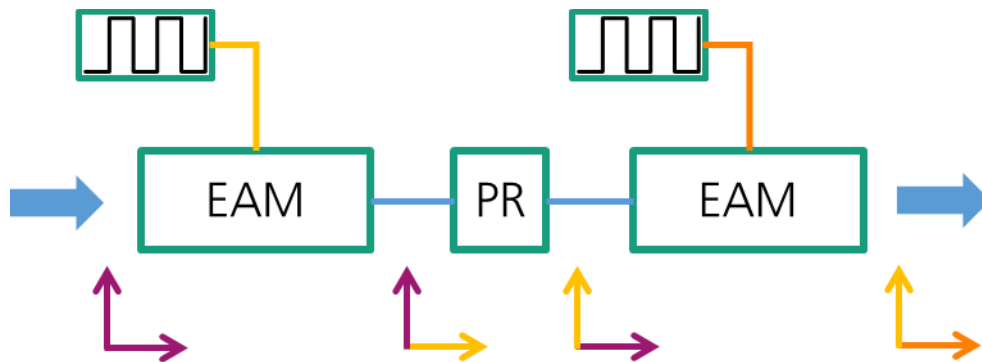


Figure 3-7. Alternative scheme for dual-polarization modulation.

The proposed scheme can in principle also be used with MZMs or even IQ modulators, as they normally also have strong polarization dependence. In this thesis, however, we will focus on EAMs for short reach applications. The following sections discuss the theoretical details and implementation of an EAM Building Block (BB) in HHI's generic photonic integration technology. Together with the PR from the previous chapter, the EAM will enable the implementation of the entire dual-polarization modulator.

3.2.2 Theoretical Background of EAMs

To implement these modulators, multi-quantum well- (MQW) based EAMs shall be used. MQW-based EAMs are typically compressively strained. As will be discussed in this chapter, this makes them strongly polarization dependent, which is exactly what is required for a device as in figure 3-7.

3.2.2.1 Electronic Properties of Multi-Quantum Wells

The valence states in covalently bound crystals exist in three distinct subbands: heavy hole, light hole and spin orbit split-off bands. Unlike unbound states with their s-like orbitals, bound states are p-like, i.e. they have three distinct symmetry planes.

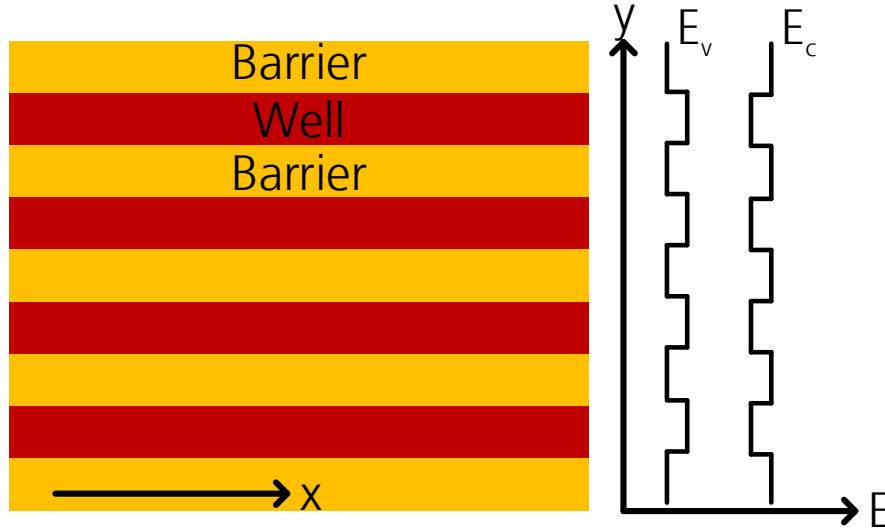


Figure 3-8. Schematic of the band diagram across four quantum wells. We use y as the normal coordinate to the MQW layers, to be consistent with previous definitions.

In unstrained bulk InGaAsP, the heavy hole (HH) and light hole (LH) bands are degenerate, i.e. at the Γ point their energies are equal. When electrons and holes are confined in quantum wells, however, the degeneracy no longer holds. To see this, the electronic states in a finite quantum well are considered. Following the derivation in [42], chapter 3, we first define m_w^* and m_b^* the effective electron masses in the well and barrier, respectively. ΔE is the potential depth. Further:

$$k = \frac{\sqrt{2m_w^*E}}{\hbar} \quad (3.20)$$

and

$$\alpha = \frac{\sqrt{2m_b^*(\Delta E - E)}}{\hbar} \quad (3.21)$$

The well is of thickness t_w . Then, the states can be found by finding the eigenenergies E of

$$\alpha = \frac{m_b^*k}{m_w^*} \tan\left(\frac{kt_w}{2}\right) \quad (3.22)$$

for even wave functions and

$$\alpha = -\frac{m_b^*k}{m_w^*} \cot\left(\frac{kt_w}{2}\right) \quad (3.23)$$

for uneven wave functions.

Due to their different effective masses, the energies of heavy and light holes generally are different. Hence, the band gap energy in a quantum well is not the same for heavy and light holes, even in the absence of strain. This fact is illustrated in figure 3-9.

In the presence of strain, the degeneracy of HH and LH bands is lifted even in bulk InGaAsP [55], [56]. In an epitaxial layer with lattice constant a_e grown on a substrate with lattice constant a_s , we call the epitaxial layer strain $\epsilon = (a_e - a_s)/a_s$. Two contributions lead to an energy shift of the two bands: hydrostatic strain ΔE_{Hy} and uniaxial strain ΔE_{Sh} [42], [57].

$$\Delta E_{Hy} = -2a \frac{C_{11} - C_{12}}{C_{11}} \epsilon \quad (3.24)$$

$$\Delta E_{Sh} = -2b \frac{C_{11} + 2C_{12}}{C_{11}} \epsilon \quad (3.25)$$

Consequently, a is referred to as hydrostatic deformation potential and b as shear deformation potential. C_{11} and C_{12} are the elements of the material elastic constant tensor. All four parameters generally depend on material composition and can be interpolated between the respective binary values as explained in appendix B) or chapter 2 in [42]. Using these values, figure 3-10 shows how compressive strain separates the HH band PLs and the LH band PL. Tensile strain can lead to a crossing. The unstrained case reveals the pure splitting induced by the different effective masses.

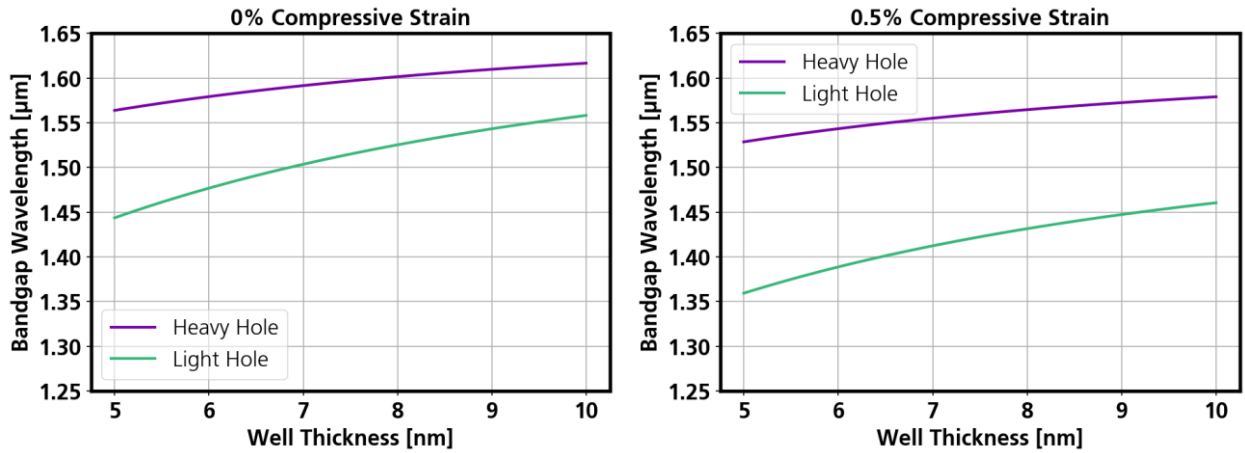


Figure 3-9. Splitting of heavy and light hole bands in the absence of strain (left) and 0.5% compressive strain (right). The splitting generally increases with decreasing well thickness.

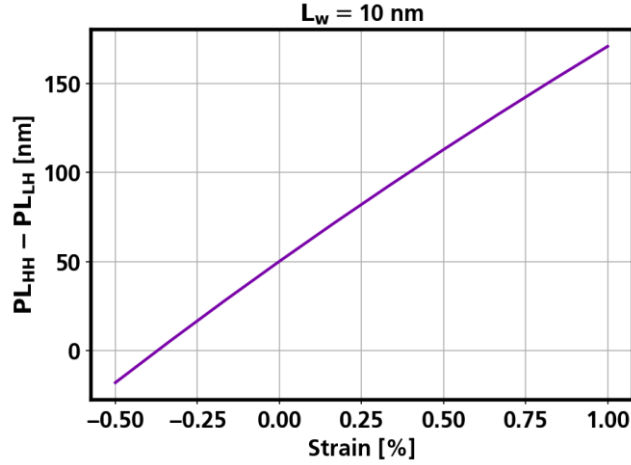


Figure 3-10. Difference of the HH and LH PLs versus strain for a MQW stack with 10 nm thick wells. The HH PL is kept constant to $1.55 \mu\text{m}$ for all strain values by adjusting the material composition. For tensile strain around -0.4% , the bands cross and the resulting PLs become equal.

3.2.2.2 Optical Absorption in Multi-Quantum Wells

Using Fermi's golden rule (p.351, [55]), the absorption coefficient of bulk semiconductor is found to be:

$$\alpha(E_{ph}) = \frac{2C_0}{V} \sum_a \sum_b |\hat{e} \cdot \vec{p}_{cv}|^2 \delta(E_c - E_v - E_{ph})(f_v - f_c) \quad (3.26)$$

where C_0 contains natural constants and the optical angular frequency ω :

$$C_0 = \frac{\pi e^2}{nc\epsilon_0 m_0^2 \omega} \quad (3.27)$$

$|\hat{e} \cdot \vec{p}_{cv}|^2$ is the momentum matrix element. \hat{e} is the unit vector along the optical field and \vec{p}_{cv} is the linear momentum associated with an electronic transition from the conduction to the valence band. The momentum matrix element can be derived in closed form for quantum wells [55]:

$$|\hat{x} \cdot \vec{p}_{cv}|^2 = \begin{cases} \frac{3}{2} & \text{heavy holes} \\ \frac{1}{2} & \text{light holes} \end{cases} \quad (3.28)$$

$$|\hat{y} \cdot \vec{p}_{cv}|^2 = \begin{cases} 0 & \text{heavy holes} \\ 2 & \text{light holes} \end{cases} \quad (3.29)$$

These matrix elements determine the polarization dependence of electro-absorption in MQWs. Even in the case of energetically degenerate heavy- and light hole bands (e.g. in bulk material), heavy hole transitions contribute three times as much to optical absorption of TE polarized light (\hat{x}). But because the two subbands are typically split in MQWs (see previous section), light hole transitions can be neglected all together (their band gap energy is much bigger). For TM-polarized (\hat{y}) light, however, heavy hole transitions are completely forbidden. This polarization can only interact with the light hole band. As a result, in MQWs

with any compressive strain in the wells, the edge of the absorption spectrum of TE light is red-shifted with respect to TM light. This is because the heavy hole band gap is smaller than the light hole band gap.

It should be stressed that (3.28) and (3.29) only hold for quantum wells. For quantum dots, the polarization dependence disappears in principle due to their isotropic nature. Real quantum dots are always strained due to the involved wetting layers, however, leading to a polarization dependence. Quantum wires are interesting because the polarization selectivity depends on which of the wire sidewalls is shorter [58]. Hence, precise control of the wire dimensions enables engineering of the polarization dependent gain.

3.2.2.3 Refractive Index of Multi-Quantum Wells

While most models for the refractive index of InGaAsP work reliably far away from the band edge, they normally diverge close to it. EAMs naturally are operated at wavelengths close to the active layer's band edge. A different model than in chapter 2 is therefore needed. Theoretically, the dispersion of the refractive index' real part can be calculated by the well know Kramers Kronig relation for linear, causal systems [59]–[62]. In general, it gives a closed form relationship of the real and imaginary part of the system response in the frequency domain. With it, the refractive index can be written as a function of the absorption spectrum $\alpha(\omega)$:

$$n(\omega) - 1 = \frac{c_0}{\pi} P \int_0^\infty \frac{\alpha(\omega')}{\omega'^2 - \omega^2} d\omega' \quad (3.30)$$

P denotes that the Cauchy principal value must be taken at the integrand singularity, i.e. $\omega' = \omega$. A similar relation can be deduced to calculate the absorption coefficient from the refractive index.

Besides computational complexity, (3.30) requires knowledge of α over an infinite spectral range, or at least a very wide range. Tanguy proposed a model in [63] that approximates (3.30) in closed form using a decomposition of α into various physical effects. It writes as:

$$n^2(\omega) - 1 = \frac{a}{b - E} + \frac{A\sqrt{R}}{E^2} \left(\ln \frac{E_g^2}{E_g^2 - E^2} + \pi \left(2 \cot \left(\pi \sqrt{\frac{R}{E_g}} \right) - \cot \left(\pi \sqrt{\frac{R}{E_g - E}} \right) - \cot \left(\pi \sqrt{\frac{R}{E_g + E}} \right) \right) \right) \quad (3.31)$$

, where $E = \hbar\omega + i\Gamma$, i.e. the photon energy with an imaginary broadening factor. a, b, A and R are fitting parameters. It has been shown experimentally by Seifert et al. in [64] that for InGaAsP, all open parameters can be fitted linearly versus the band gap. The resulting dispersion curves for the real and imaginary parts of bulk unstrained InGaAsP with a PL of

1.55 μm are shown in figure 3-11.

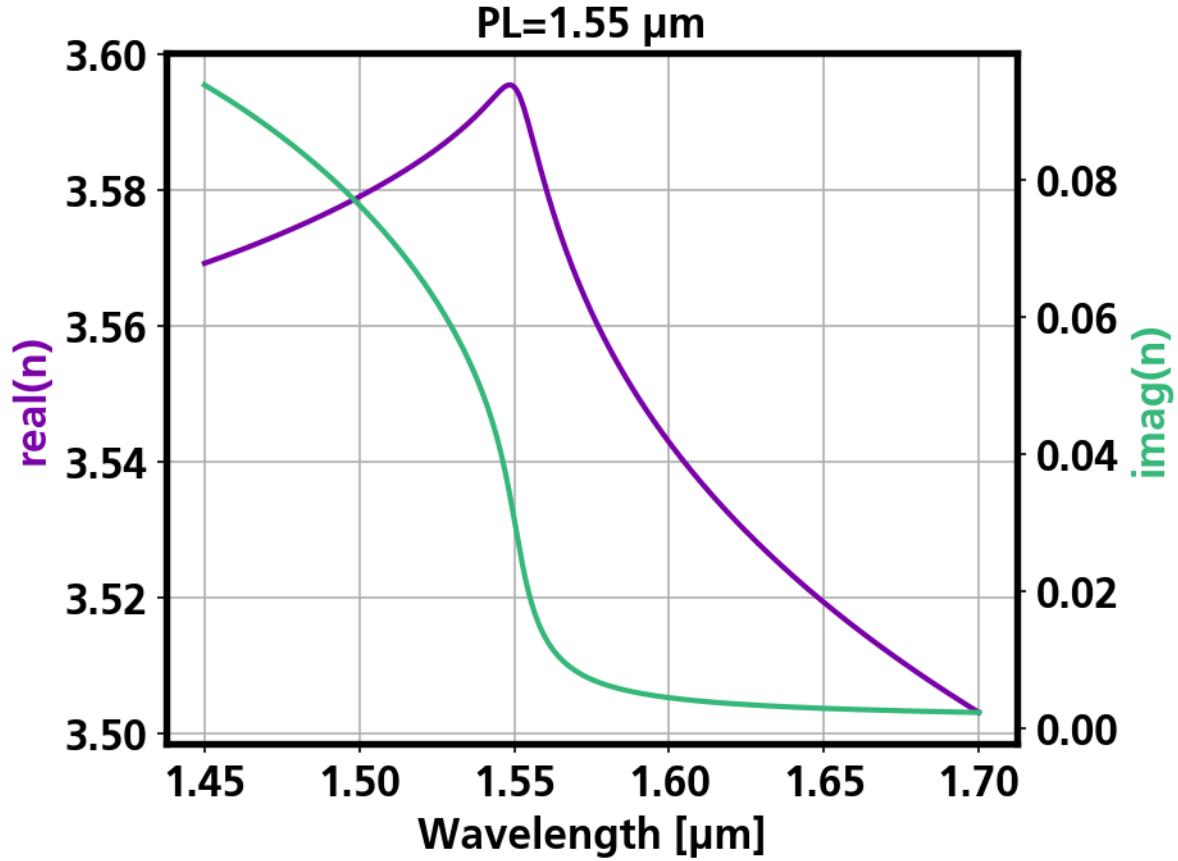


Figure 3-11. Dispersion of the real (purple) and imaginary (green) parts of the refractive index of bulk InGaAsP with no strain and a PL of 1.55 μm . Since bulk material is isotropic, the indices are equal for TE and TM.

As pointed out by v.d. Ziel et al. in [65], MQW layer stacks can be described by an effective index that is composed of the indices of the wells and barriers. The effective description depends on polarization, as follows:

$$n_{TE,eff}^2 = \frac{n_{TE,w}^2 \cdot t_w + n_{TE,b}^2 \cdot t_b}{t_w + t_b} \quad (3.32)$$

$$n_{TM,eff}^2 = \frac{t_w + t_b}{\frac{t_w}{n_{TM,w}^2} + \frac{t_b}{n_{TM,b}^2}} \quad (3.33)$$

The indices of the wells and barriers for the two polarizations can be calculated from the indices resulting from the different band edges for heavy- and light holes, taking into account the momentum matrix elements from the previous chapter. As a result, the anisotropic dispersion curves for an entire MQW stack can be calculated. An example is shown in figure 3-12. This index model can then be used in a mode solver to calculate the indices of the modes propagating in an MQW-loaded waveguide.

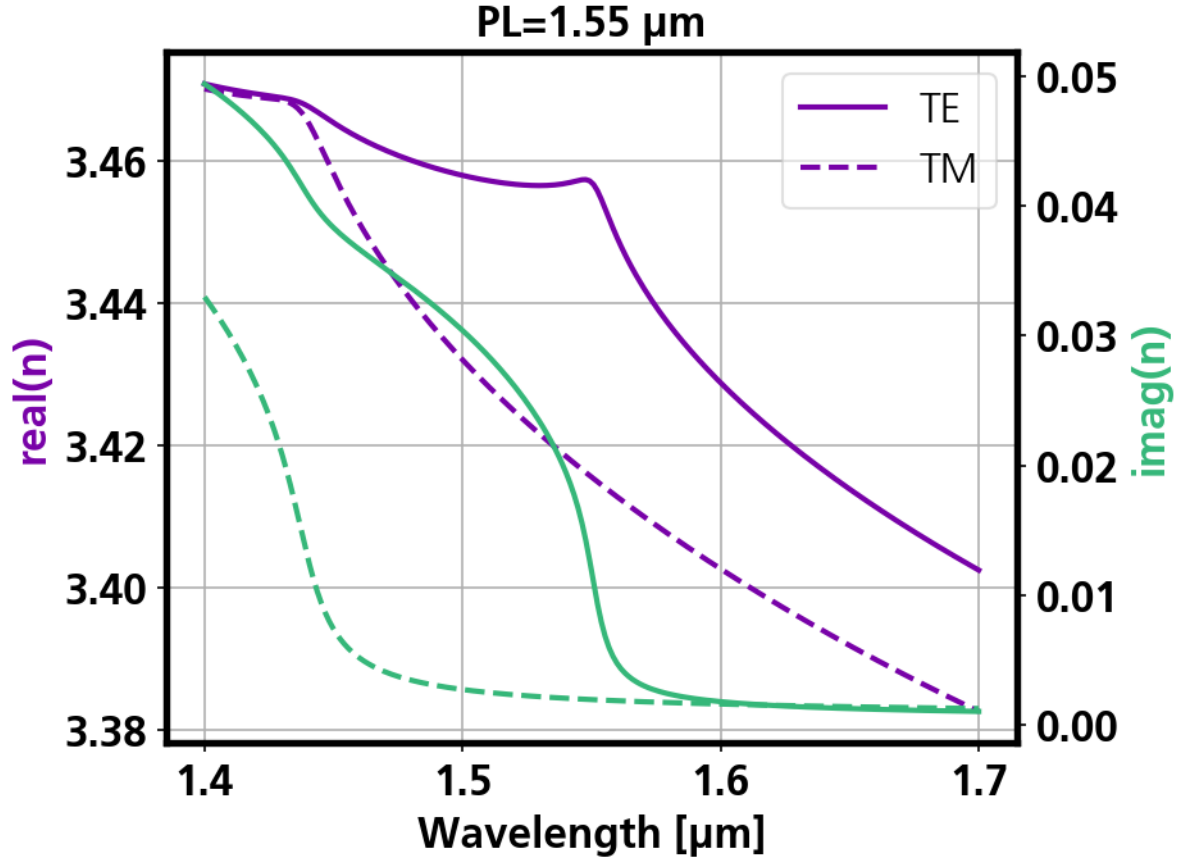


Figure 3-12. Anisotropic index dispersion of an MQW stack after eq. (3.32) and (3.33). The individual indices of wells and barriers are calculated according to the selection rules in section 3.2.2.2. The MQW stack shown here as 10 nm thick wells that are compressively strained by 0.5%.

3.2.2.4 The Quantum Confined Stark Effect

The dominating effect leading to electro-absorption in MQWs is the quantum-confined Stark effect (QCSE). The QCSE was first experimentally reported 1984 by Wood et al. in [66] and was then theoretically explained by the same group in the same year (Miller et al., [67]). It is a field effect that decreases the band gap energy in the wells. This leads to a shift of the entire absorption spectrum towards lower photon energies or larger photon wavelengths. The effect is illustrated in figure 3-13. The applied electric fields tilts the band structure, which in turn changes the shape of the wave functions for electrons and holes. This leads to a preference of electrons for positions inside the well that have lower energies, while holes will prefer larger energy positions. Thus, the gap between the two energies is reduced. Although the field separates electrons and holes, their separation is in the order of the well width, which typically is smaller than the size of the excitonic wave function. Hence, the electron-hole separation has no significant impact on the electron-hole interaction, e.g. electro-optic transitions. For large fields, however, this does not hold anymore and the absorption quenches.

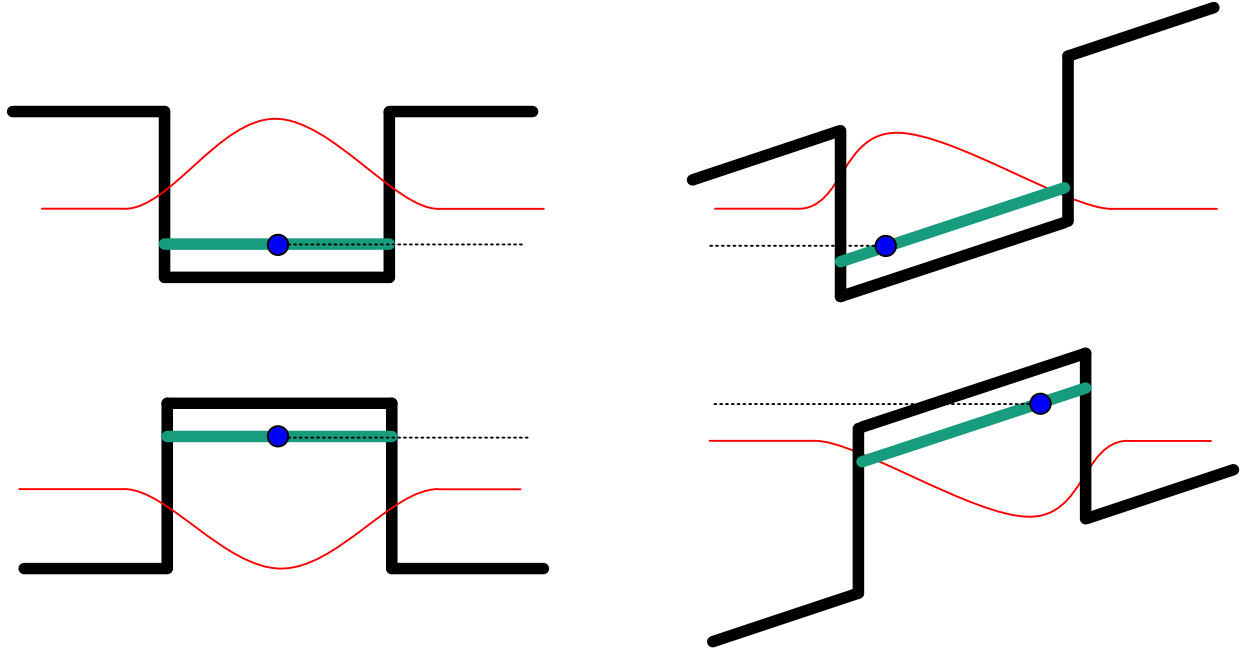


Figure 3-13. Visualization of the band structure giving rise to the quantum-confined Stark effect (QCSE). With no potential applied to the double heterostructure (left), the wavefunctions of electron and hole overlap strongly. Their energetic gap is homogeneous across the well. However, the electronic states get tilted along the y -axis when a potential drops across the structure (right). The respective wavefunctions of electron and hole are displaced such that the energetic difference between the states becomes smaller. This gives rise to a shift of the optical absorption spectrum.

Due to the strong polarization sensitivity of the momentum matrix elements associated with the heavy hole- and light hole transitions, the QCSE is generally also strongly polarization dependent. We saw that for compressively strained wells, the heavy hole transition has the lowest energy. But since the associated momentum matrix element vanishes for TM polarized light, it only contributes to absorption of TE-polarized light. A quantitative analysis of the shift of the bands ΔE due to an electric field F was given by Bastard in 1983 [68]. In literature, one mostly only finds the small-field approximation for thin wells, infinitely high barriers and small fields. [69]–[71]. Thin wells means around 3 nm [68], while the field is considered small if:

$$eFt_w \ll E_1 = \frac{\hbar^2 \pi^2}{2m^* t_w^2} \quad (3.34)$$

I.e. the potential dropping across a well is small compared to the ground state E_1 in the well. In this regime, the shift is simply a quadratic function in the electric field:

$$\Delta E = -\frac{m^* e^2 F^2 t_w^4}{24 \hbar^2 \pi^4} (\pi^2 - 15) \quad (3.35)$$

The shift of the band edge then simply becomes $\Delta E_g = \Delta E_c + \Delta E_v$, calculated with the respective masses in the sub bands. Because the shift is proportional to the effective mass, the heavy hole band gap shifts more than the light hole gap. So if one were to make a

QCSE-based modulator operating around the light hole gap (e.g. to make a TM modulator), it would intrinsically suffer from a lower modulation depth.

The quadratic field dependence of (3.35) breaks down in the case of strong fields. A closed form description for ΔE versus any arbitrary field is not possible, but Bastard et al. gave the eigenenergy equation that is to be minimized in [68]:

$$E(\beta) = E_1 \left(1 + \frac{\beta^2}{4\pi^2} + \phi \left(\frac{1}{\beta} + \frac{2\beta}{4\pi^2 + \beta^2} - \frac{1}{2 \tanh\left(\frac{\beta}{2}\right)} \right) \right) \quad (3.36)$$

with the minimization parameter β and the dimensionless electrostatic energy

$$\phi = \frac{eFt_w}{E_1} \quad (3.37)$$

The equation is implemented in python where it can be solved numerically for arbitrary fields. Simulated Stark shifts obtained by this model are shown in figure 3-14.

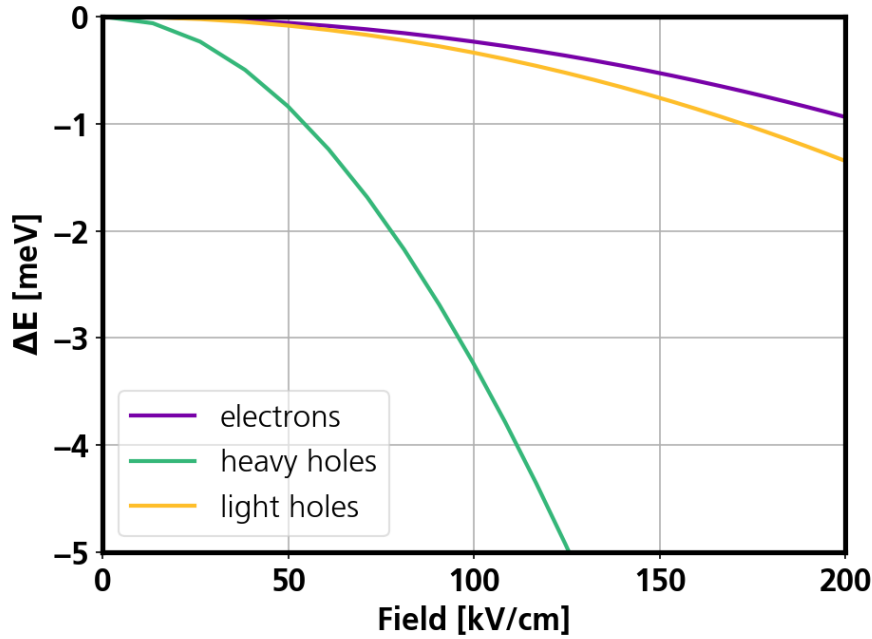


Figure 3-14. Simulated Stark shifts for the respective carriers versus electric field. The MQW structure has a net photoluminescence of $1.53 \mu\text{m}$. The plot is generated by numerically solving equation (3.36). Therefore it holds only for infinitely high barriers, but for arbitrarily large fields. Because tunneling does not occur in this case, the strength of the shifts shows a clear dependence on the effective carrier mass.

For finite barrier heights, however, the situation is further complicated by tunneling effects and the increased spatial separation of electrons and holes induced by the electric field. Bastard et al. pointed out that the effect of finite barrier heights is rather drastic, reporting a 28x to 38x increase of the Stark shift [68]. For weak fields, the Stark shift enhancement can be expressed by Ω^2/Ω_∞^2 with

$$\Omega = A \left(\frac{1}{3} + \frac{\sin k_0}{k_0} + \frac{2 \cos k_0}{k_0^2} - \frac{2 \sin k_0}{k_0^3} + \frac{2}{q_0} \left(1 + \frac{2}{q_0} + \frac{2}{q_0^2} \right) \cos^2 \left(\frac{k_0}{2} \right) \right) \quad (3.38)$$

where

$$A = \frac{1}{1 + \frac{\sin k_0}{k_0} + \frac{2}{q_0} \cos \left(\frac{k_0}{2} \right)} ; q_0^2 = \frac{2m^* t_w^2}{\hbar^2} (V_0 - E_1) ; k_0^2 = \frac{2m^* t_w^2 E_1}{\hbar^2} ; \Omega_\infty = \frac{1}{3} - \frac{2}{\pi^2} \quad (3.39)$$

A is a normalization constant for the continuity of the wave function, q_0 is the wave function's decay constant into the barrier of finite height V_0 and k_0 is the dimensionless wave vector with no field applied. Naturally, $\Omega \rightarrow \Omega_\infty$ for $V_0 \rightarrow \infty$. Note that to calculate k_0 , the ground state energy for a finite barrier height is needed rather than the infinite case of (3.34). It is calculated with section 3.2.2.1.

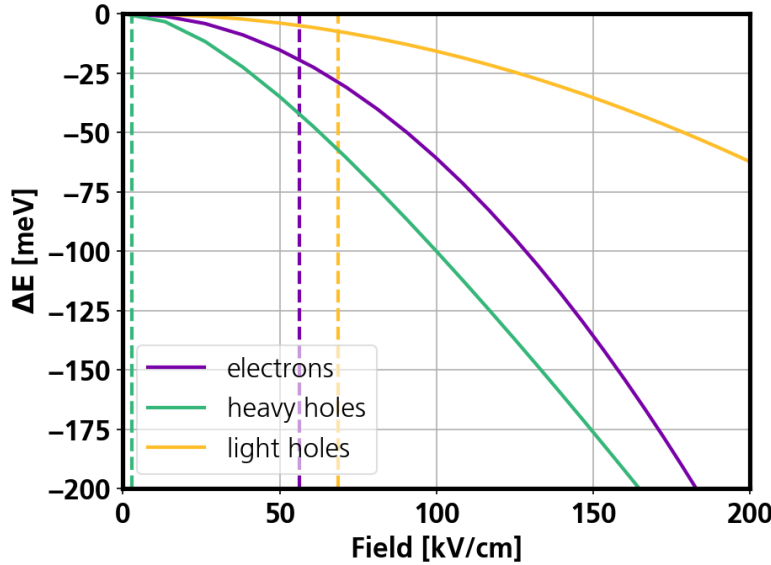


Figure 3-15. Simulated Stark shifts for the respective carriers versus electric field. The MQW structure has a net photoluminescence of $1.53 \mu\text{m}$. The plot is generated by numerically solving equation (3.36) and takes into account the enhancement factor for finite barrier heights. Therefore it holds only for small fields. The critical fields $F_{crit} = \frac{E_1}{eL_w}$ at which the approximation brakes down are depicted as dashed lines.

Given that the enhancement factor is invalid for practical fields (50 kV/cm correspond to a bias of -1 V), we will assume the infinite barrier case in the following. Therefore, the calculated Stark shifts will underestimate the real shifts. The path towards a complete treatment of finite barriers and large fields is pointed towards in [68] and [72].

The results of the QCSE theory will be used in the following to simulate the polarization dependent behavior of the EAM. This will ultimately be used to enable performance estimations of the full DP EAM structure.

3.2.3 EAM Design

3.2.3.1 Modes, birefringence

The EAM is implemented in the MQW-loaded waveguide of HHI's generic integration technology. It uses a ridge waveguide design with an n-doped guiding layer underneath the MQW stack. A cross sectional view of the refractive index distribution is given in figure 3-16. The waveguide supports TE and TM modes.

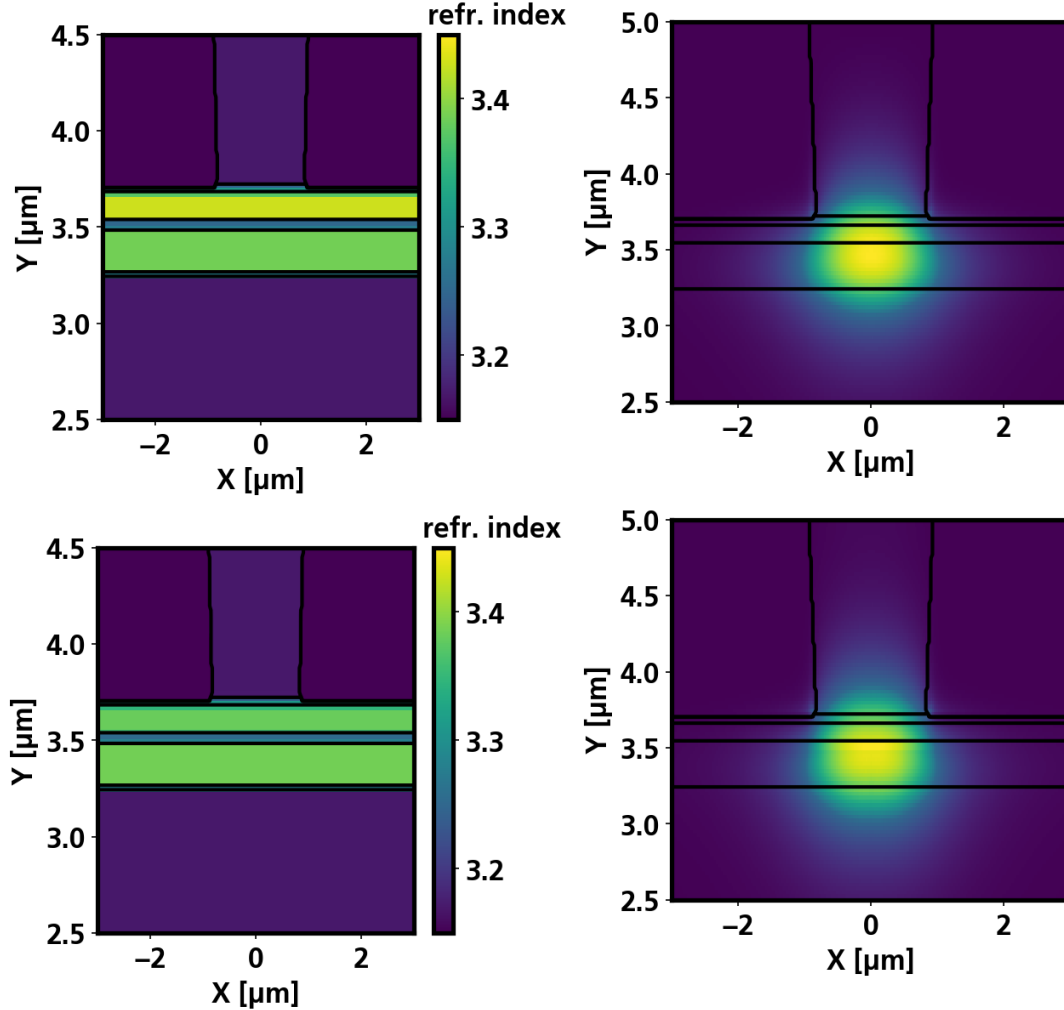


Figure 3-16. Cross-sectional view of the refractive index profile (left) and mode distribution (right) for TE polarized light (top) and TM polarized light (bottom).

To verify that an EAM based on this waveguide really only modulates TE-polarized light, the complex effective index is simulated as a function of MQW PL. This effectively emulates modulation in a real device, as modulation is achieved by means of the QCSE-induced band gap shift. The result is shown in figure 3-17. Indeed, the TM mode modulation is negligible compared to the TE modulation.

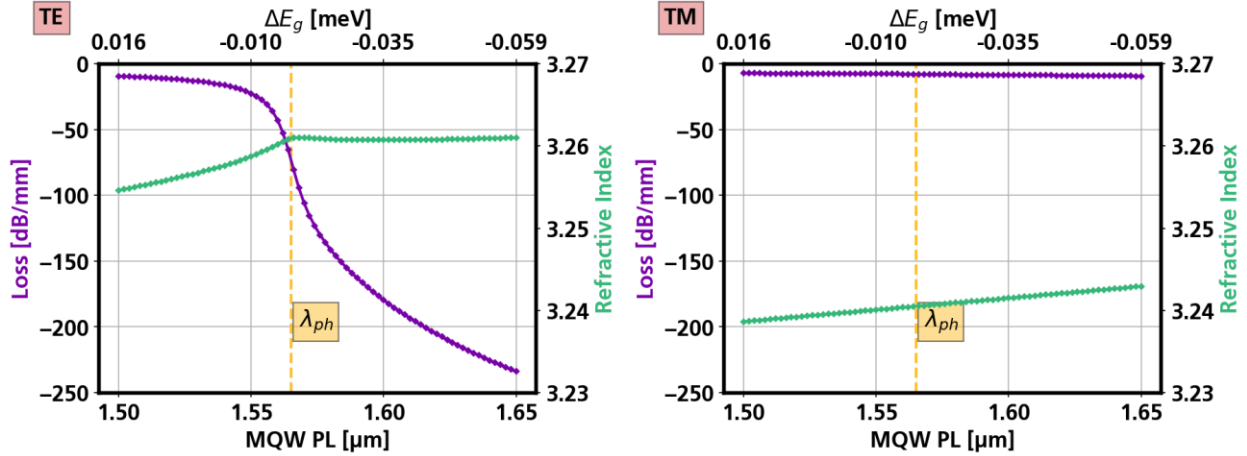


Figure 3-17. MODE simulations of the EAM waveguide operated at a wavelength λ_{ph} of 1565 nm for TE (left) and TM (right). Plotted are the waveguide absorption and effective index versus the MQW photoluminescence (PL). The as-grown PL is 1530 nm, corresponding to $\Delta E_g = 0$ in the upper axis.

Because the integration platform relies on iron-doped (i.e. semi-insulating) substrates, the n-region has to be contacted from the top. To bring the n-contact as close to the active layer as possible, a new form of n-contact is used in the generic technology. Normally, the n-region is contacted 15 μm away from the ridge waveguide and only on one side of the waveguide. A closer and double-sided contact would be desirable, but is prohibited by the electro-plating process. To solve this, the platinum heater, that is also part of the process design kit (PDK) is used. The configuration is shown in figure 3-18.

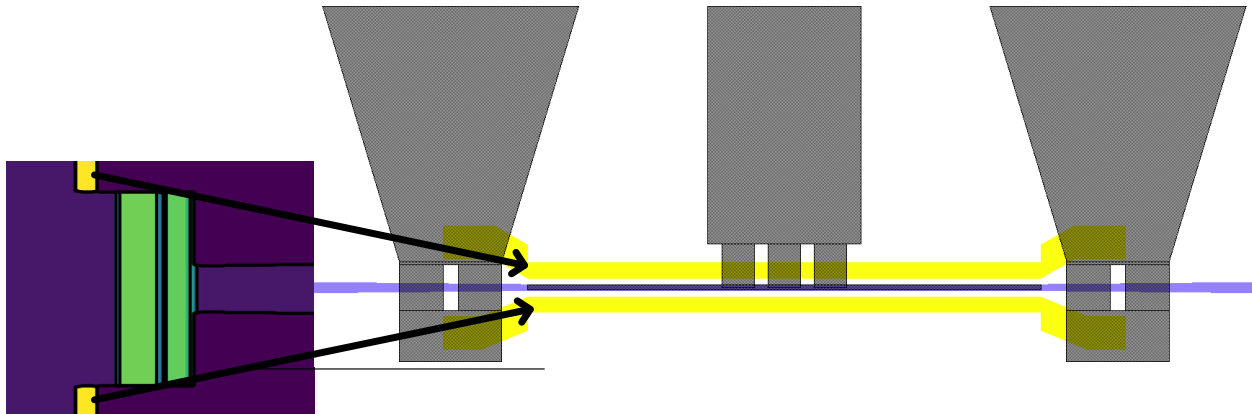


Figure 3-18. EAM cross-section (left) and the layout top view (right). It uses the platinum process of HHI's generic technology, which is normally used for heaters. For the EAM, it is used to bring the n-side contact as close to the active region as possible, while also using both sides of the waveguide for contacting. Most of the layers in the layout view are left out for clarity. The dark grey layer corresponds to the electro plating. The plated gold forms bridges over the waveguide and the platinum stripes.

The lower boundary for the separation of the platinum to the waveguide is given by plasmonic losses. If the platinum is too close, the optical mode will experience excess loss. The propagation loss increases significantly for an edge-to-edge separation between

waveguide and platinum of less than $1\text{ }\mu\text{m}$, as shown in figure 3-19. To allow some error margin for the lithography, the separation in the EAM is chosen as $2.5\text{ }\mu\text{m}$.

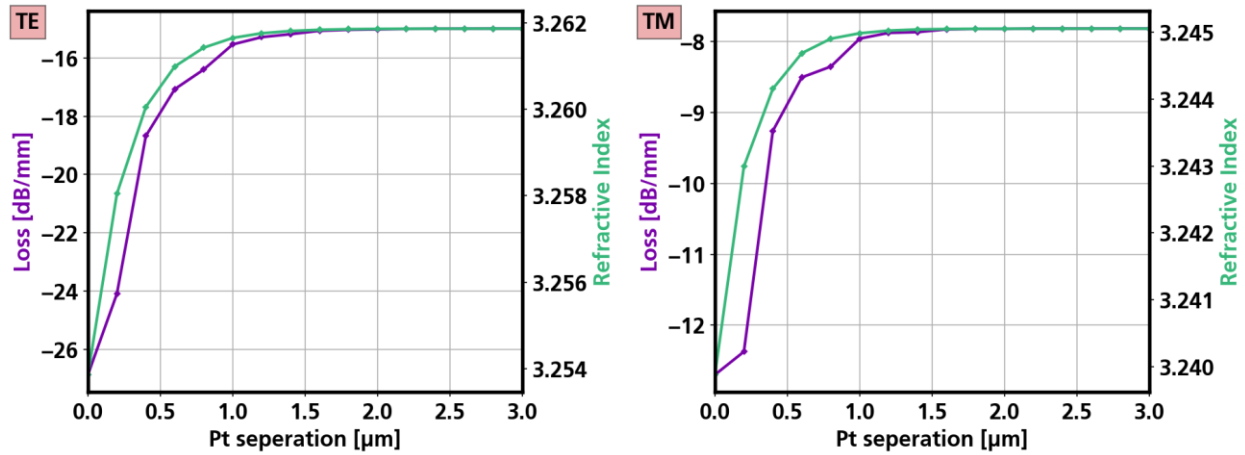


Figure 3-19. Propagation loss in the EAM versus edge-to-edge distance from waveguide to platinum stripe. Both TE (left) and TM (right) experience significant excess loss for separations below $1\text{ }\mu\text{m}$.

3.2.3.2 Electrical properties

The EAM can be thought as an equivalent circuit as in figure 3-20. In reverse bias, the pin-junction acts as a capacitor. To simulate the structure, Lumerical's DEVICE solver is used [41]. It solves the Poisson equation to calculate the electric field and charge distribution, taking into account the device band structure and doping profile. The purpose of this simulation is to ultimately extract the junction capacitance, which is critical for the RF performance of the EAM.

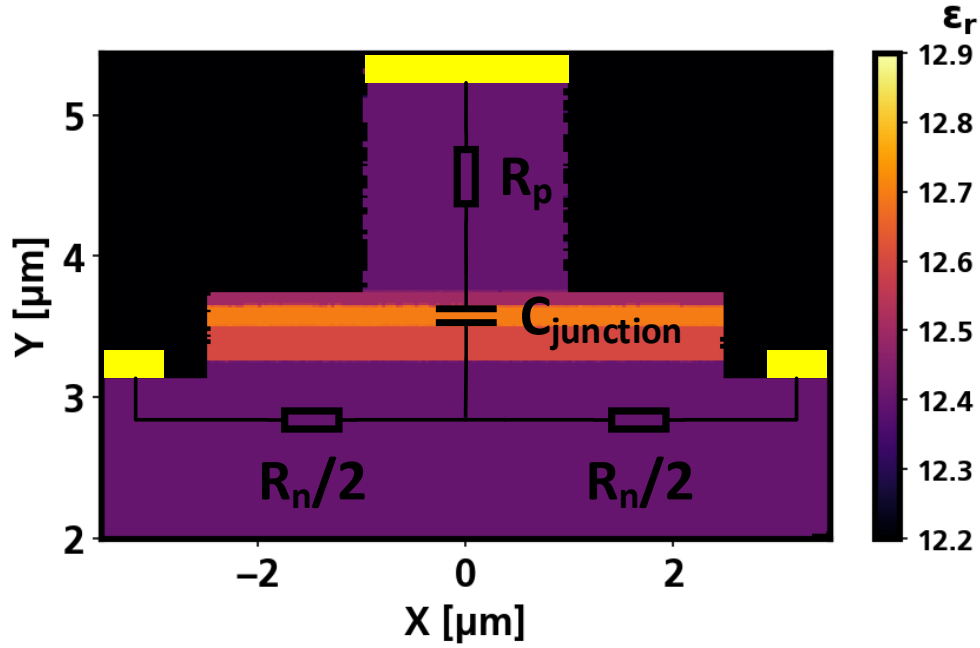


Figure 3-20. Equivalent circuit drawn on top of the cross section as used in DEVICE simulations. The roughness on some interfaces is an artifact caused by the export and not present in the actual simulations.

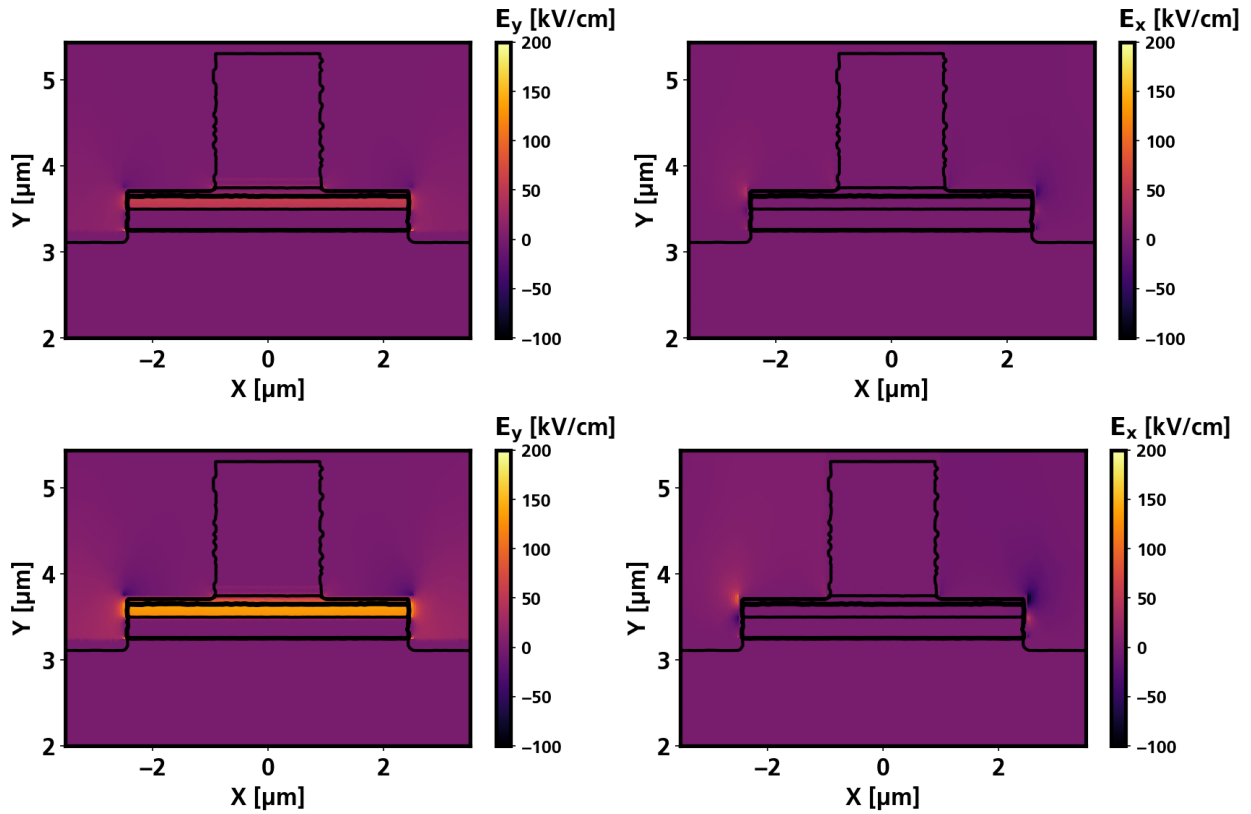


Figure 3-21. Electric fields along x (right) and y (left) for no bias (top) and -2 V bias (bottom). The built-in field across the MQW region due to carrier depletion is around 50 kV/cm along the y-axis.

Neglecting carrier life- and transit-times in the active region, the EAM frequency response is RC limited:

$$f_{3dB} = \frac{1}{2\pi RC} = \frac{1}{2\pi(R_n + R_p)C_{junction}} \quad (3.40)$$

The resistances of the n- and p-regions are simply given by:

$$R = \frac{L}{\sigma A} = \frac{L}{(n\mu_e + p\mu_p)eA} \quad (3.41)$$

The capacitance can be approximated by a parallel plate capacitor or more accurately via $C = \frac{dQ}{dV}$. Since DEVICE can simulate the charge distribution as a function of bias voltage, this enables the simulation of the capacitance as a function of voltage. The simulated excess charge density distribution $\Delta Q = \Delta n + \Delta p$ at -2 V is shown in figure 3-22. The voltage dependent capacity is plotted in figure 3-23.

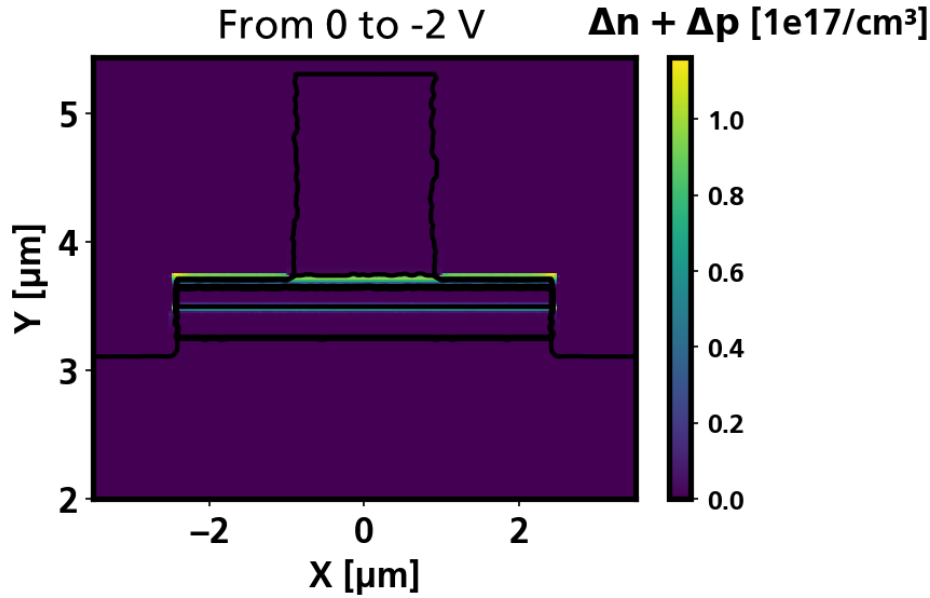


Figure 3-22. Charge density distribution accumulated by applying a bias of -2 V. The distribution at zero bias is subtracted from the total charge density, so only the excess charge density is shown. Charge accumulated at the interfaces to the intrinsic MQW region.

Figure 3-23 also shows the average field inside the MQW region, which is the field responsible for modulation. It is generally the voltage across the MQW stack divided by the thickness of the space charge region (SCR). Since the SCR widens with bias voltage, the field can be written as:

$$E_{y,MQW} = \frac{V_{MQW}}{t_{SCR}(V_{bias})} = \frac{V_{bias} - V_d}{t_{MQW} - aV_{bias}} \quad (3.42)$$

where a is the linear dependence of the SCR on the bias voltage and V_d is the built-in diffusion potential. As can be seen in figure 3-23, the fit gives a good approximation. V_d is 0.7 V, while the SCR widening is found to be $a \approx 20$ nm/V.

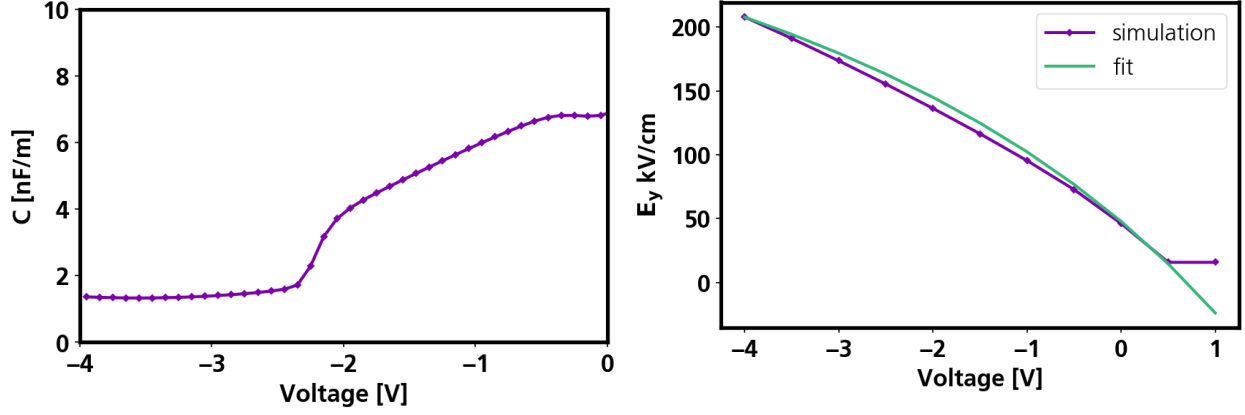


Figure 3-23. Simulated capacitance per unit length as a function of bias voltage (left). Increasing the bias widens the depletion zone in the junction, leading to a decrease of the capacitance. The widening of the depletion zone can also be seen in the sub-linear dependence of the field across the MQWs versus voltage (right). It can be approximated by $E_y = \frac{V-V_d}{t_{MQW}-aV}$.

3.2.3.3 Electro-optic properties

With the fields calculated in the previous section and the index and QCSE models from sections 3.2.2.3 and 3.2.2.4, the actual EAM modulation can be studied. As discussed before, the QCSE model in the simulations can underestimate the real shifts by a factor of up to 28 because it assumes infinite barriers. Effectively, this lead to simulations that suggest too large modulation voltages for a given extinction. Nevertheless, figure 3-24 demonstrates that the EAM as designed in the generic technology only modulates TE polarized light.

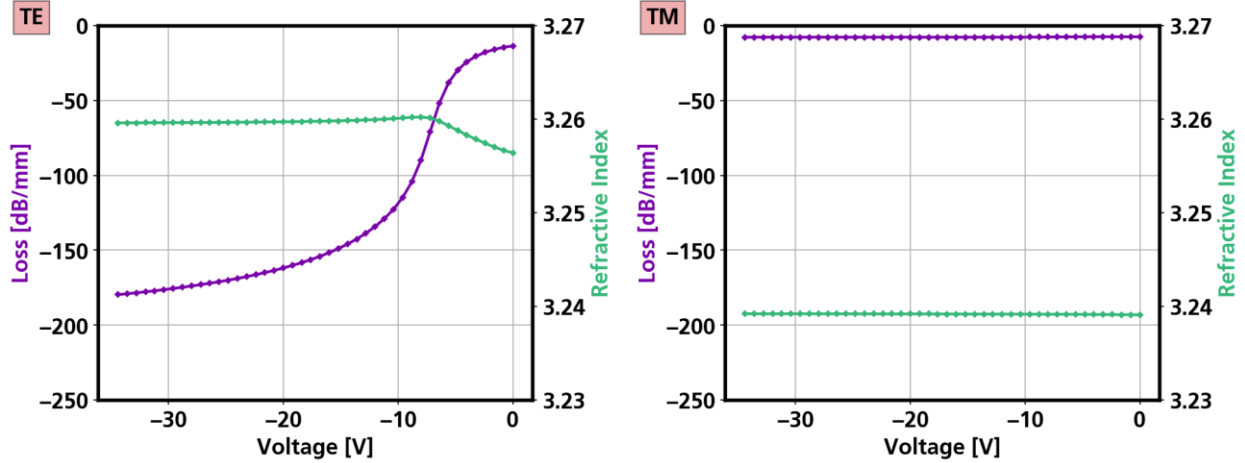


Figure 3-24. Modulation of the TE mode (left) and TM mode (right) in the EAM model. The TM modulation is negligible compared to the TE modulation.

The curves from figure 3-24 encapsulate the entire static optoelectronic behavior of the EAM. They are used in the following section to perform system level analysis.

3.2.4 DP EAM Simulations

So far, polarization-resolved simulations of the individual EAMs are obtained. Together with a low-pass filter derived from the equivalent circuit, we use these results to perform large signal simulations of the DP EAM. To do so, Lumerical's INTERCONNECT tool is used [41].

The EAM is modelled electrically as a low-pass filter. Optically, it is modelled as two independent optical paths for TE and TM polarized light, respectively (see figure 3-25). At the EAM input (output), the two paths are split (combined) by ideal polarization splitters (combiners). In the two parallel branches the modulation of the complex indices for TE and TM from chapter 3.2.3 are implemented. Effectively, each branch represents the modulation of one of the polarizations. This model is encapsulated into a composite building block that is then used for the full system simulation as it is shown in figure 3-26.

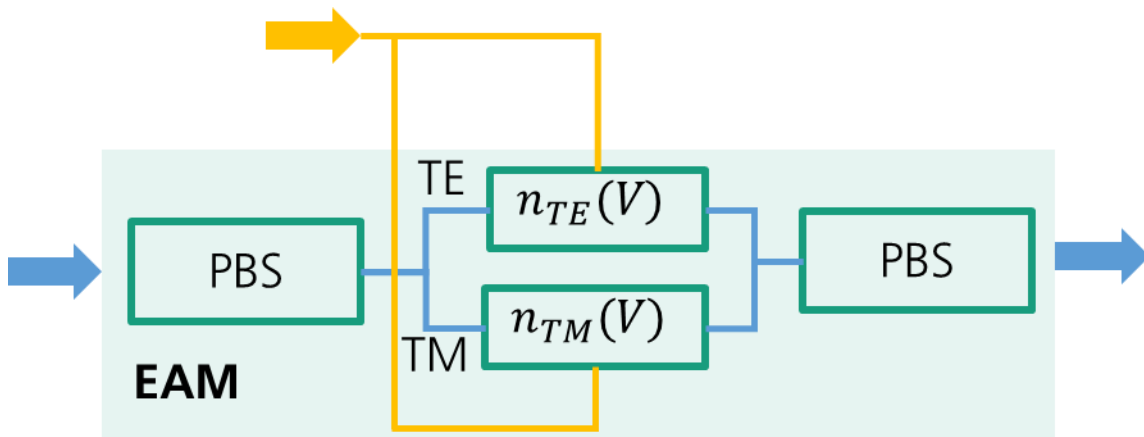


Figure 3-25. Equivalent circuit to model the EAM in INTERCONNECT. The voltage dependent complex indices $n_{TE}(V)$ and $n_{TM}(V)$ are taken from the QCSE calculations in chapter 3.2.3. Because the software does not

include a modulator model with anisotropy, the EAM is modelled as two modulators for the respective polarizations which are split and combined accordingly.

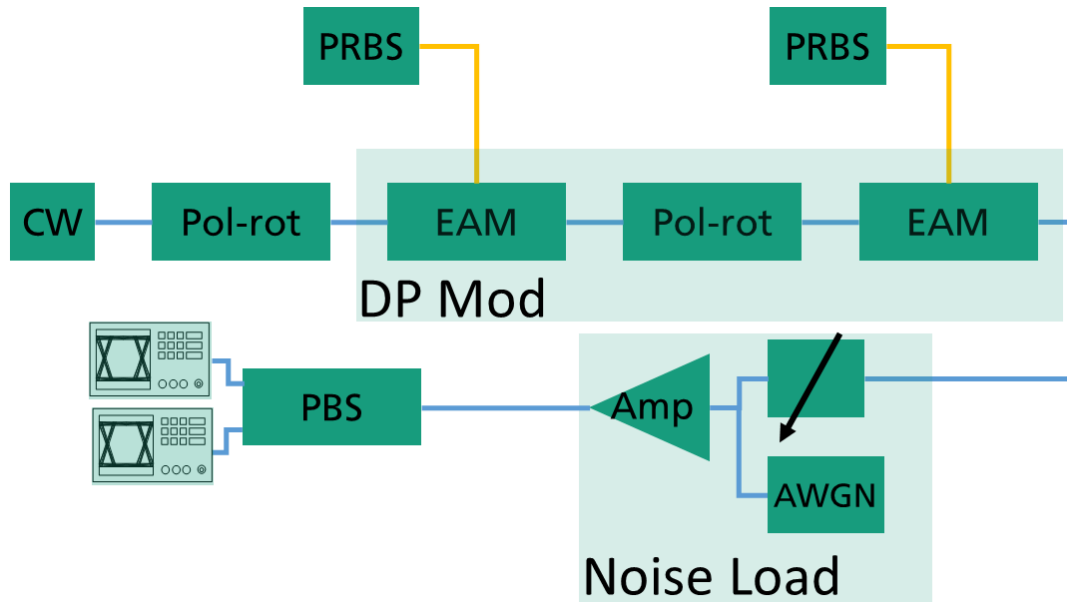


Figure 3-26. The simulated dual-polarization modulator circuit as used in INTERCONNECT. A TE-polarized continuous wave (CW) optical source undergoes polarization rotation by 45° . Two EAMs follow which are interconnected by a polarization rotator that rotates by another 90° in the ideal case. The EAMs themselves are circuits as in Figure 3-25. A noise loading stage consisting of an attenuator, an amplifier and additive white Gaussian noise (AWGN) is used to set arbitrary OSNR values. A polarization beam splitter is used with two receivers to analyze the modulated signals in the two polarization states.

Example eye diagrams of the two received polarizations are shown in figure 3-27. The PR in between the two EAMs is intentionally set to not rotate by exactly 90° but rather 72.5° , 81° and 84.5° . This corresponds to a PER of 10 dB, 15 dB and 20 dB, respectively. The OSNR is set to 20 dB in all cases. In the example of the 15 dB case, the eyes are still open but the signal transmitted by the first EAM is impaired. This can be understood with the fact that 15 dB conversion efficiency means that 0.13 dB are left in the original TE polarization state. This part of the modulated signal then gets modulated again by the second EAM, leading to cross modulation. The 10 dB PER case gives a closed eye transmitted by the first EAM while for 20 dB PER, the first eye has seemingly the same quality as the second EAM's eye.

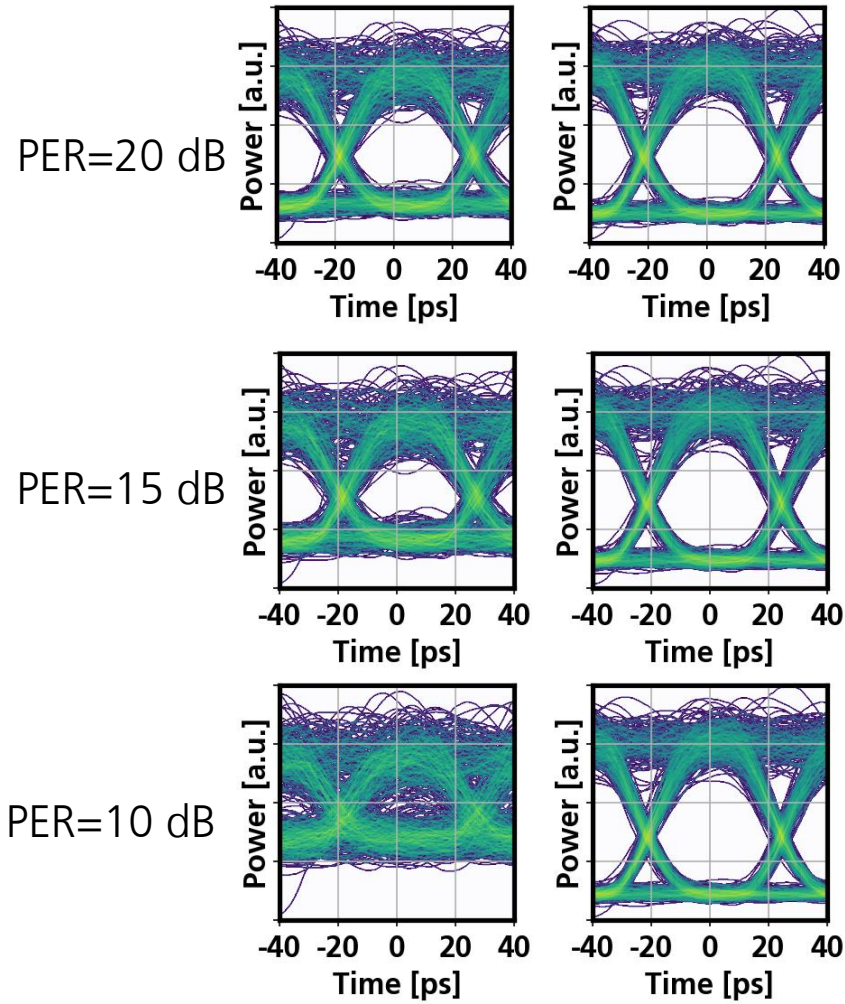


Figure 3-27. Received eye diagrams in the two polarizations for an OSNR of 20 dB. With decreasing PER, the eye corresponding to the first EAM deteriorates.

By calculating the optimum decision thresholds and the μ and σ values for the one and zero levels, INTERCONNECT can calculate the bit error ratios (BER) of the two received signals. BER versus OSNR curves are shown in figure 3-28 for different PERs of the critical PR. At a PER of around 20 dB, the BER converges to a constant value. At a BER of 10^{-9} , the OSNR penalty introduced by the non-ideal PER is plotted in figure 3-29. The penalty is below 1 dB for a PER above 16 dB. In terms of rotational angle, this leaves a corridor of $\pm 9^\circ$ around the ideal 90° .

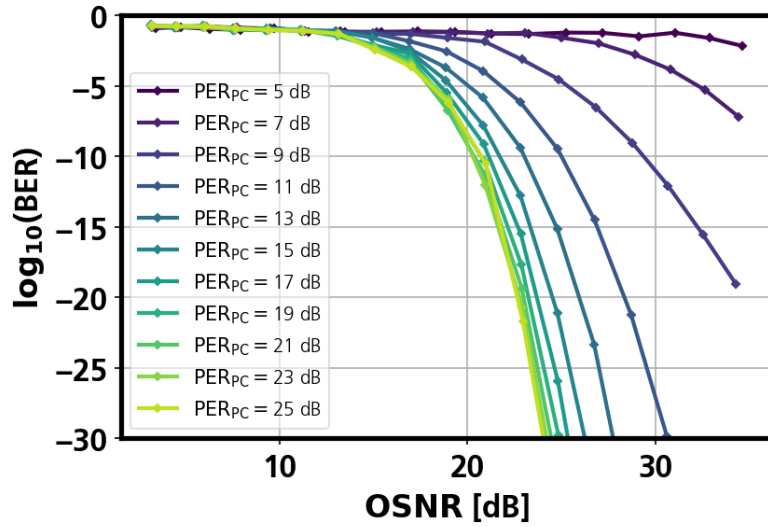


Figure 3-28. Bit error ratio (BER) of the dual-polarization transmitter simulated for different PERs of the rotator in between the two EAMs. The total BER is calculated as the sum of the two individual BERs.

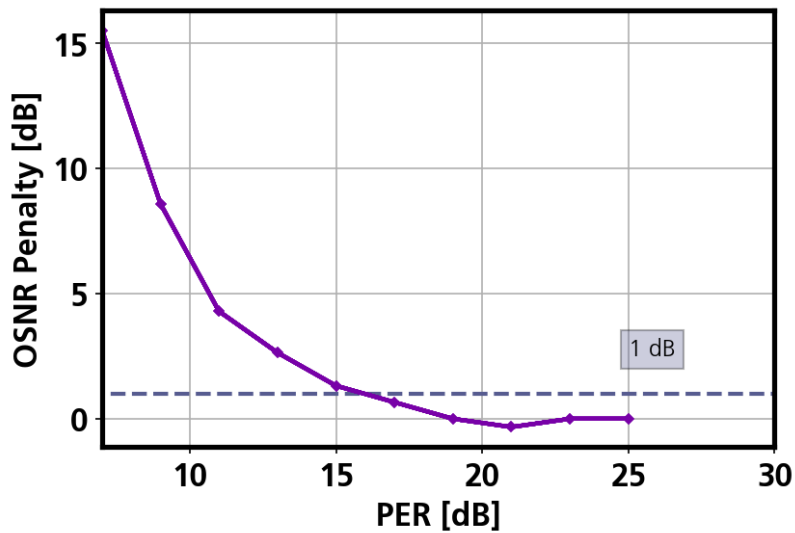


Figure 3-29. Penalty in terms of receiver OSNR for different PER values. The penalty converges to 0 dB for large PERs. It stays below 1 dB (yellow line) for a PER greater than 15 dB.

4 Experiments

4.1 Experimental Methodology – Fiber Based Stokes Measurements

With the mathematical convenience of the Jones formalism comes the price of experimental impracticalities. Jones vectors are representations of perfectly polarized coherent light. Most laboratory equipment cannot measure the absolute phase of optical signals though, so coherent measurements become an issue. Further, a Jones matrix cannot describe the process of depolarization and a Jones vector cannot describe unpolarized light. As was seen in chapter 2.3, both issues are tackled by moving to the Stokes/Müller Formalism. The goal of this chapter is the extraction and analysis of the Müller matrix $\underline{M}_{\text{PIC}}$ of any given integrated device. Except the absolute phase acquired during propagation, the Müller matrix contains a complete picture of the polarization properties of the element it represents. To leverage mature equipment and enable automated measurements, a completely fiber-based setup is pursued.

It should be noted that measurements of integrated optical devices are typically not done in Stokes space in literature. Rather, extinction ratios between TE and TM polarization are recorded at the in- and outputs of the device under test [16], [51], [73]–[75]. As a result, measurements cannot be done without going through free space optics such as lenses and polarizers. When measuring pure TE/TM extinction ratios, the relative phase information gets lost, so the birefringence or helicity of devices remains inaccessible. Some authors used distinct optical polarizations at the input, while only measuring the total power at the output [76], [77]. Effectively, this yields only the first row of the Müller matrix, but it is sufficient to determine the dependence of transmittance on polarization, i.e. PDL. There are reports on interferometric schemes that effectively measure the Jones matrix of a given device, sometimes referred to as optical vector network analyzer [78]–[80]. Apart from depolarization, these methods yield the full Müller matrix, but they require at least one interferometer in the fiber setup. This method is not pursued here to avoid the long-term stability issues that come with fiber based interferometers. To the author's best knowledge, no non-coherent method for full Müller matrix measurements of PICs has been shown yet. Dong et al. did show a method to measure the Müller matrix of fibers, however [81].

4.1.1 Experimental Setup

4.1.1.1 Setup Overview

The schematic of the complete setup is shown in figure 4-1. Its key components are a polarization controller and a polarimeter, both computer controlled. On the control computer, python is used for the communication with the measurement equipment and all necessary calculations.

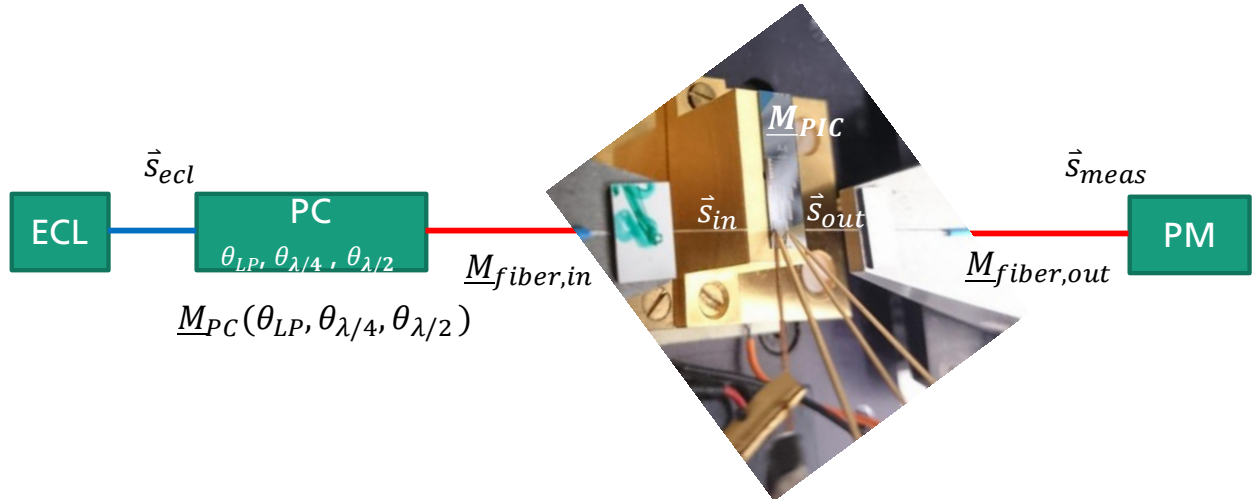


Figure 4-1. Schematic overview of the fiber-based setup to measure the polarization effects in integrated devices. Light of an external cavity lasers (ECL) of Stokes vector \vec{s}_{ecl} goes through a commercial computer-controlled polarization controller (PC). The PC consists of a cascade of a linear polarizer, $\lambda/4$ - and $\lambda/2$ -waveplate. All elements can be rotated by arbitrary angles. The PC is followed by a lensed SSF for efficient chip coupling. The same kind of fiber is used to couple light out of the chip and to route it to a polarimeter (PM) that measures \vec{s}_{meas} . Both input and output fibers are described by their respective Müller matrices $\underline{M}_{fiber,in}$ and $\underline{M}_{fiber,out}$. \vec{s}_{in} and \vec{s}_{out} are the Stokes vectors of the light coupling into and out of the integrated device, which is characterized by its Müller matrix \underline{M}_{PIC} .

As will be seen in chapter 4.1.2, control over \vec{s}_{in} and knowledge of \vec{s}_{out} enables the measurement of \underline{M}_{PIC} . The polarization controller can be used to change \vec{s}_{in} . The polarimeter measures the Stokes vector \vec{s}_{meas} , which is determined by \vec{s}_{out} . However, in both cases an optical fiber complicates the relationships between the respective vectors. The complete setup uses standard single-mode fiber (SSMF). A reliable polarization model for SSMF is therefore needed. The model is then used to undo the effects of the fibers to extract both \vec{s}_{in} and \vec{s}_{out} .

It might seem a natural choice to use polarization maintaining fibers (PMF) instead of SSMF. But PMF only work properly if the polarization injected into the fiber is exactly aligned with either the slow or the fast axis of the PMF. If not, the PMF does in fact rotate the polarization much more rapidly than SSMF. This is because PMF has strong built-in birefringence due to its non rotationally symmetric cross section. But since we want to set arbitrary \vec{s}_{in} and measure the corresponding \vec{s}_{out} , PMF are actually ill suited for this task. Another practical issue would be to accurately align the fast or slow axis of the PMF with the substrate of the chip.

4.1.1.2 Polarization in Optical Fibers

Any piece of SSMF induces an arbitrary rotation of the incident SOP. A practical model for polarization rotation in SSMF is therefore needed.

As has been shown by Walker and Walker [82], [83], mapping between arbitrary SOPs can be achieved by three linear retardation elements at angles θ_i with retardation δ_i . Without

changing the retardation, any given SOP can be mapped to any desired SOP by adjusting the θ_i . This only holds, however, for the condition

$$\frac{\pi}{2} - (|\delta'_1| + |\delta'_2| + |\delta'_3|) \geq 0 \quad (4.1)$$

with

$$\delta'_i = \begin{cases} \frac{\pi}{2} - \delta_i, & 0 \leq \delta_i \leq \pi \\ -\frac{\pi}{2} - \delta_i, & -\pi \leq \delta_i \leq 0 \end{cases} \quad (4.2)$$

One solution to this is $\delta_1 = \delta_3 = \frac{\pi}{2}$ and $\delta_2 = \pi$, i.e. quarter- half- and quarter-wave plate. This is the traditional choice for fiber-based polarization controllers where fiber loops of N, 2N and N windings are used ("Mickey Mouse Ears"). As has been commented in [82], this is not the only solution and also not the ideal solution in some cases. Three quarter-wave plates are the obvious solution to (4.1) and (4.2) and offer the highest tolerance with respect to the elements retardation, namely $\pm \frac{\pi}{6}$. Further, the order of the waveplates is not significant. Since we are only interested in a good mathematical model for arbitrary SOP mapping, we stick to the well known model $(\frac{\pi}{2}, \pi, \frac{\pi}{2})$. The resulting Müller matrix $\underline{M}_{\text{fiber}}$ describes how an input SOP gets mapped to an output SOP:

$$\underline{M}_{\text{fiber}} = \underline{M}_{\lambda/4}(\theta_3) \underline{M}_{\lambda/2}(\theta_2) \underline{M}_{\lambda/4}(\theta_1) \quad (4.3)$$

Since SSMF is dispersive, the angles θ_i will generally also be dispersive. An experimental example is shown in figure 4-2. Because the θ_i are continuous versus wavelength, they can be smoothly interpolated between sampling points. In the following chapters, we will use the $(\frac{\pi}{2}, \pi, \frac{\pi}{2})$ model for all fibers involved.

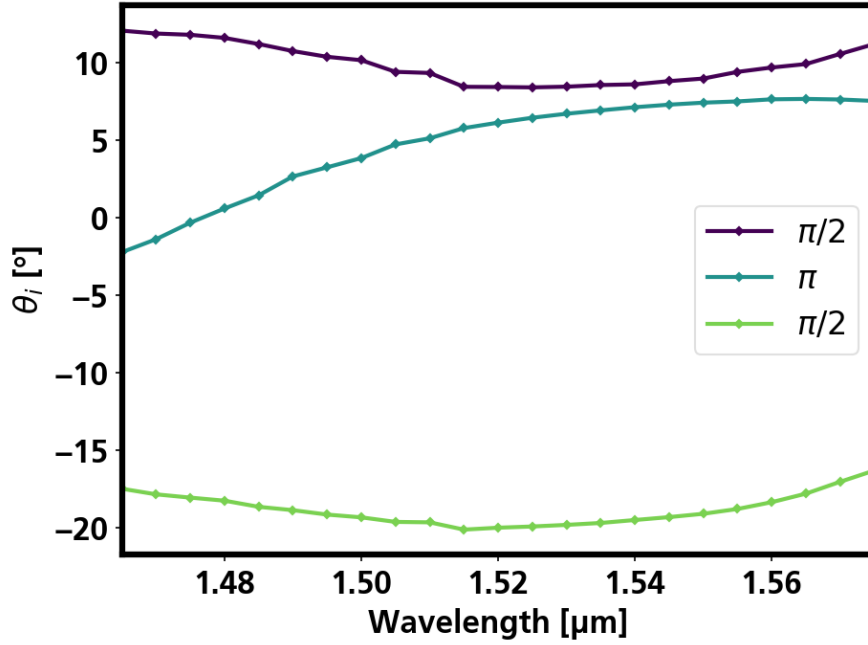


Figure 4-2. Experimental values of the equivalent retarder angles of some meters of SS MF. The retardations are $\frac{\pi}{2}$, π and $\frac{\pi}{2}$, i.e. the classical quarter-, half- and quarter-wave plate arrangement as used in loop-based polarization controllers.

4.1.1.3 Setup Modelling

With the setup as shown in figure 4-1, one can write the important relationships for \vec{s}_{in} and \vec{s}_{out} :

$$\vec{s}_{in} = \underline{M}_{fiber,in} \underline{M}_{PC} \left(\theta_{LP}, \theta_{\frac{\lambda}{4}}, \theta_{\frac{\lambda}{2}} \right) \vec{s}_{ecl} \quad (4.4)$$

$$\vec{s}_{meas} = \alpha_{F2F} \underline{M}_{fiber,out} \vec{s}_{out} \quad (4.5)$$

α_{F2F} is the fiber-to-fiber loss. The polarization controller is comprised of three elements: a linear polarizer, a quarter waveplate and a half waveplate. For higher accuracy of the model, they are modelled as an elliptical diattenuator and two elliptical retarders (see appendix A)), each rotated by the angle set in the controller. Further, the PDL of the controller is modelled by another elliptical diattenuator. The PDL is specified by the manual with ± 0.03 dB. So, we can write the Müller matrix of the PC as:

$$\underline{M}_{PC} \left(\theta_{LP}, \theta_{\frac{\lambda}{4}}, \theta_{\frac{\lambda}{2}} \right) = \underline{\tilde{M}}_{\frac{\lambda}{2}} \left(\theta_{\frac{\lambda}{2}} \right) \underline{\tilde{M}}_{\frac{\lambda}{4}} \left(\theta_{\frac{\lambda}{4}} \right) \underline{\tilde{M}}_{LP} \left(\theta_{LP} \right) \quad (4.6)$$

Here, $\underline{\tilde{M}}$ denotes non-ideal elements with some residual ellipticity and retardation offset. In the example of a non-ideal half waveplate, it is defined as follows: the eigenvector \vec{u} of the non-rotated waveplate should be $(1 \ 1 \ 0 \ 0)^T$, or $\psi_{\vec{u}} = 0$ and $\chi_{\vec{u}} = 0$. The actual eigenvector will be slightly rotated, so that $\psi_{\vec{u}} = \Delta\psi_{\frac{\lambda}{2}}$ and $\chi_{\vec{u}} = \Delta\chi_{\frac{\lambda}{2}}$. Also, the retardation should ideally be $\delta = \pi$, but it is actually slightly off so that $\delta = \pi + \Delta\delta_{\frac{\lambda}{2}}$. The quarter

waveplate is completely analogous. Also, the polarizer diattenuation vector \vec{D} is slightly rotated by a $\Delta\psi_{LP}$ and $\Delta\chi_{LP}$.

Equation (4.5) can simply be inverted to yield \vec{s}_{out} for a given \vec{s}_{meas} . Setting a desired \vec{s}_{in} is a matter of finding the correct parameters $(\theta_{LP}, \theta_{\lambda/4}, \theta_{\lambda/2})$. Both tasks, however, require the knowledge of $\underline{M}_{fiber,in}$, $\underline{M}_{fiber,out}$, \vec{s}_{ecl} as well as all the residual errors in the PC. What follows is a discussion of how we extract all those three objects to move on with actual device measurements.

4.1.1.4 Setup Calibration

In the optical back-to-back case (no device under test present), $\vec{s}_{out} = \vec{s}_{in}$ and therefore (4.4) and (4.5) give:

$$\vec{s}_{meas} = \alpha_{F2F} \underline{M}_{fiber,out} \underline{M}_{fiber,in} \underline{M}_{PC} \left(\theta_{LP}, \theta_{\lambda/4}, \theta_{\lambda/2} \right) \vec{s}_{ecl} \quad (4.7)$$

This poses the issue of differentiating $\underline{M}_{fiber,out}$ from $\underline{M}_{fiber,in}$, since only their product appears in the back-to-back case. This makes an additional measurement necessary that introduces a modification to the setup as in figure 4-1. The modified setup is shown in figure 4-3. We can write the power measured at the photodetector as:

$$P_{FS} = (1 \ 0 \ 0 \ 0) \vec{s}_{FS} \quad (4.8)$$

With some loss α_{FS} associated to the free space path, the Stokes vector in free space is given by:

$$\vec{s}_{FS} = \alpha_{FS} \underline{M}_{LP} \underline{M}_{fiber,in} \underline{M}_{PC} \left(\theta_{LP}, \theta_{\lambda/4}, \theta_{\lambda/2} \right) \vec{s}_{ecl} \quad (4.9)$$

With (4.7) and (4.9), we have the two important equations to calibrate the setup, i.e. to determine $\underline{M}_{fiber,in}$, $\underline{M}_{fiber,out}$, \vec{s}_{ecl} as well as all the residual errors in the PC. The flow of the calibration procedure is depicted in figure 4-4. First, the setup is brought to free-space configuration (as in figure 4-3). A set of measurements of P_{FS} is recorded, with $5 \cdot 5 \cdot 3 = 75$ different settings for $(\theta_{LP}, \theta_{\lambda/4}, \theta_{\lambda/2})$ at each wavelength to be calibrated. The setup is then brought to its fiber-to-fiber configuration (figure 4-1 without a device). The same 75 settings for $(\theta_{LP}, \theta_{\lambda/4}, \theta_{\lambda/2})$ are set, but now \vec{s}_{meas} is recorded. Again, this is done for each wavelength that is to be calibrated. As a result, 150 equations per wavelength are obtained (75 per (4.7) and 75 per (4.9)), with only $\underline{M}_{fiber,in}$, $\underline{M}_{fiber,out}$, \vec{s}_{ecl} and the PC's residuals unknown. Each fiber is determined by only three parameters (see 4.1.1.2) and \vec{s}_{ecl} has two degrees of freedom (two spherical coordinates, its power is known). Hence, the 150 equations can be used to extract the unknown parameters with enough degrees of freedom left to implement a least-square fit. It uses the same python-based methodology of a target function and its minimization that has already been used for the device optimization in chapter 2.5.4. The result of the minimization is numerical values for the matrices of the two fibers as well as \vec{s}_{ecl} . Additionally, the residuals of the PC are also computed.

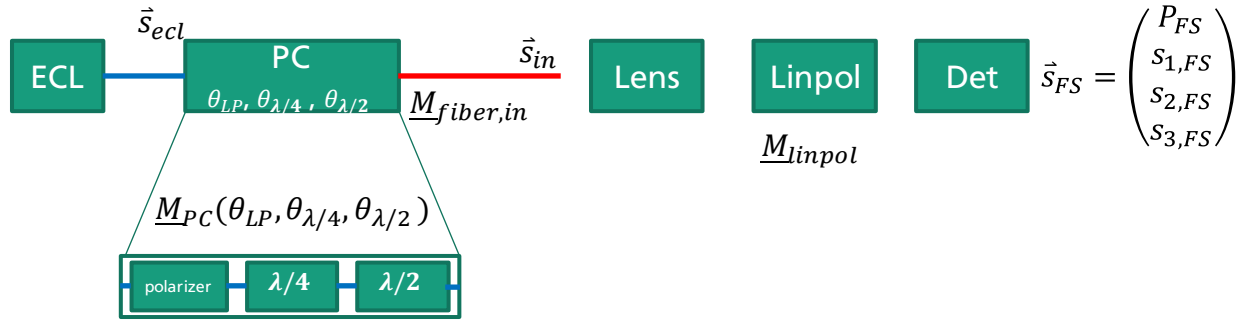


Figure 4-3. Schematic of the setup in its free space configuration. A lens is used to collimate the light exiting the input fiber. The beam is analyzed by a linear polarizer that transmits only TE light followed by a photodetector. The detector only measures P_{FS} .

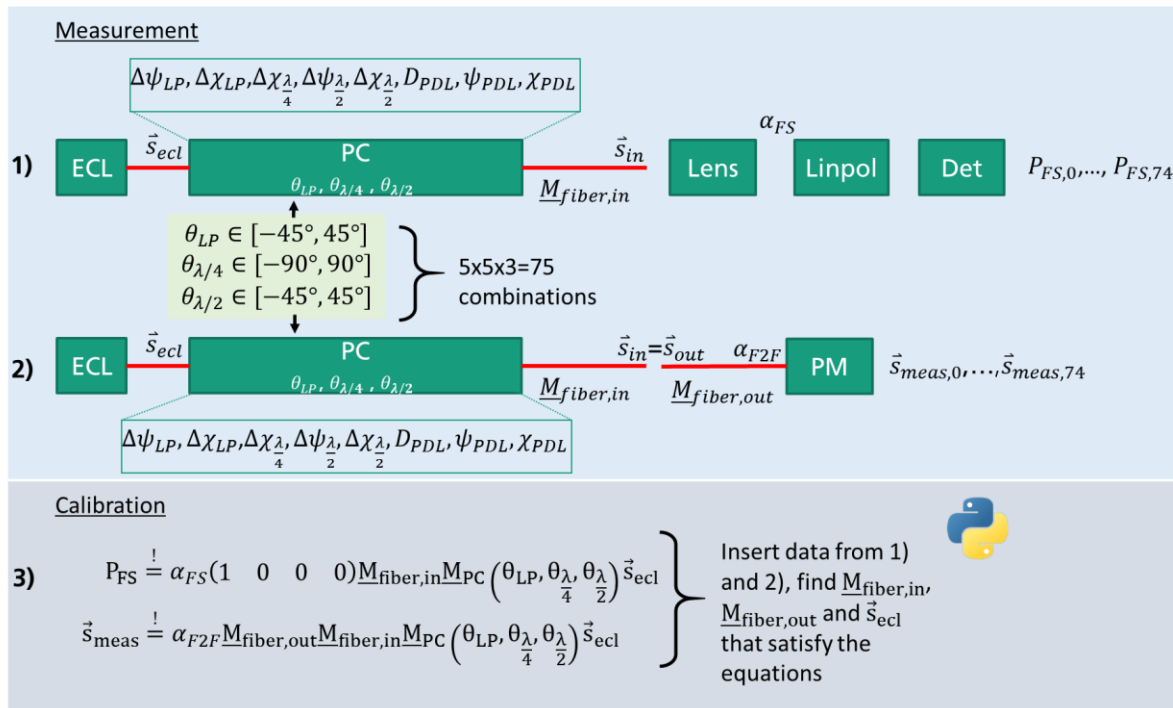


Figure 4-4. Flow of the setup calibration process. 70 triples $(\theta_{LP}, \theta_{\lambda/4}, \theta_{\lambda/2})$ are used at the polarization controller (PC), for each triple the free space power P_{FS} (1) and the in-fiber Stokes vector \vec{s}_{meas} (2) at the polarimeter (PM) are recorded. This data is used in 3) to fit all unknowns in the model: $\underline{M}_{fiber,in}$, $\underline{M}_{fiber,out}$, \vec{s}_{ecl} and the imperfections at the PC. The entire mechanism is carried out on a per-wavelength basis, with wavelengths from 1465 to 1575 nm in 5 nm steps. Spline fits are used to fill in the calibration data for a continuous wavelength range.

4.1.1.5 Calibration Validation

The validation of the calibrated setup is done two-fold. First, the triple $(\theta_{LP}, \theta_{\lambda/4}, \theta_{\lambda/2})$ is scanned and the measured values for \vec{s}_{meas} and P_{FS} are compared with what can be calculated using (4.7) and (4.9). The comparison at different wavelengths is shown in figure 4-5 and figure 4-6.

As a second step, the actual task of the setup is emulated. Rather than blindly scanning $(\theta_{LP}, \theta_{\lambda/4}, \theta_{\lambda/2})$, \vec{s}_{in} is set and \vec{s}_{out} is deduced. To do so, (4.4) and (4.5) are used. (4.5) can easily be solved for \vec{s}_{out} after measuring \vec{s}_{meas} . The appropriate $(\theta_{LP}, \theta_{\lambda/4}, \theta_{\lambda/2})$ for a desired \vec{s}_{in} can be calculated numerically. For the validation, the setup is operated in the back-to-back regime, so $\vec{s}_{in} = \vec{s}_{out}$. This way, the deviation between the desired polarization ellipse and what is measured can be specified. The deviation is expressed in terms of the central angle between the corresponding points on the Poincaré sphere. The experimental results are summarized in figure 4-7.

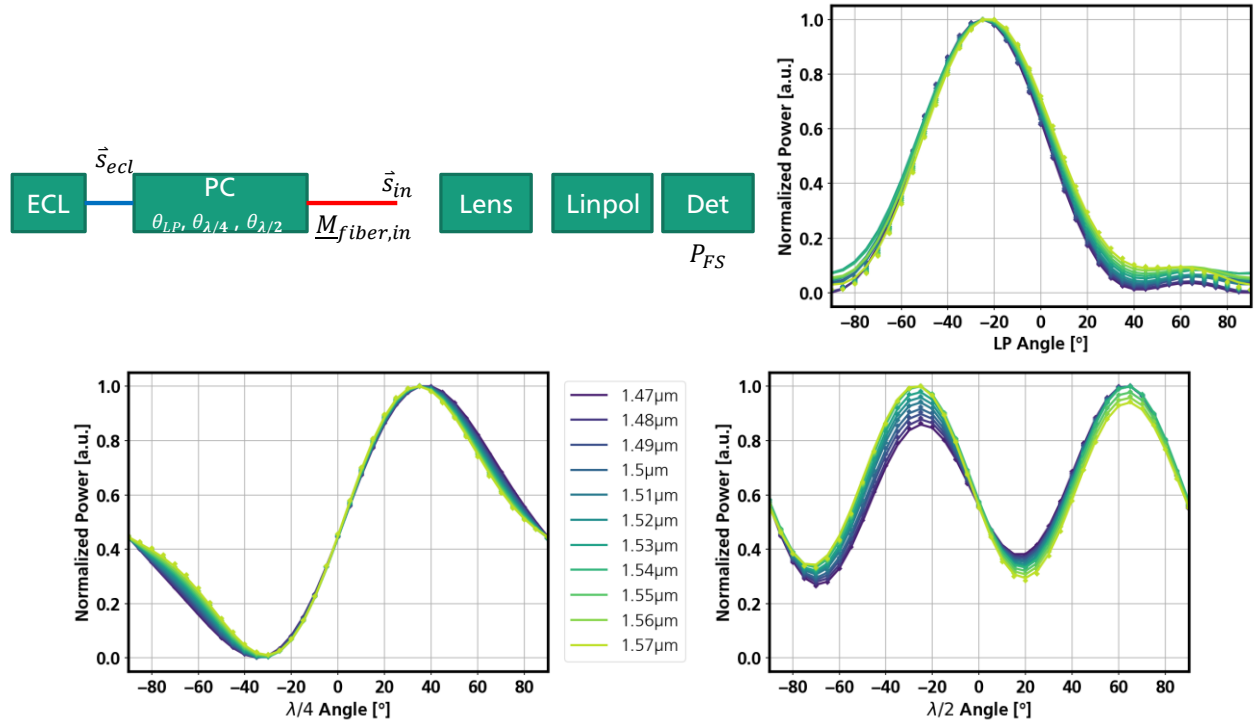


Figure 4-5. Validation of the setup calibration for the input path. The angles of the three elements of the polarization controller are swept: the linear polarizer (top right), the quarter waveplate (bottom left) and the half waveplate (bottom right). The solid lines show the predicted values after (4.9), the markers indicate actually measured values. The errors between measurement and model stay below 5% across all wavelengths and angles.

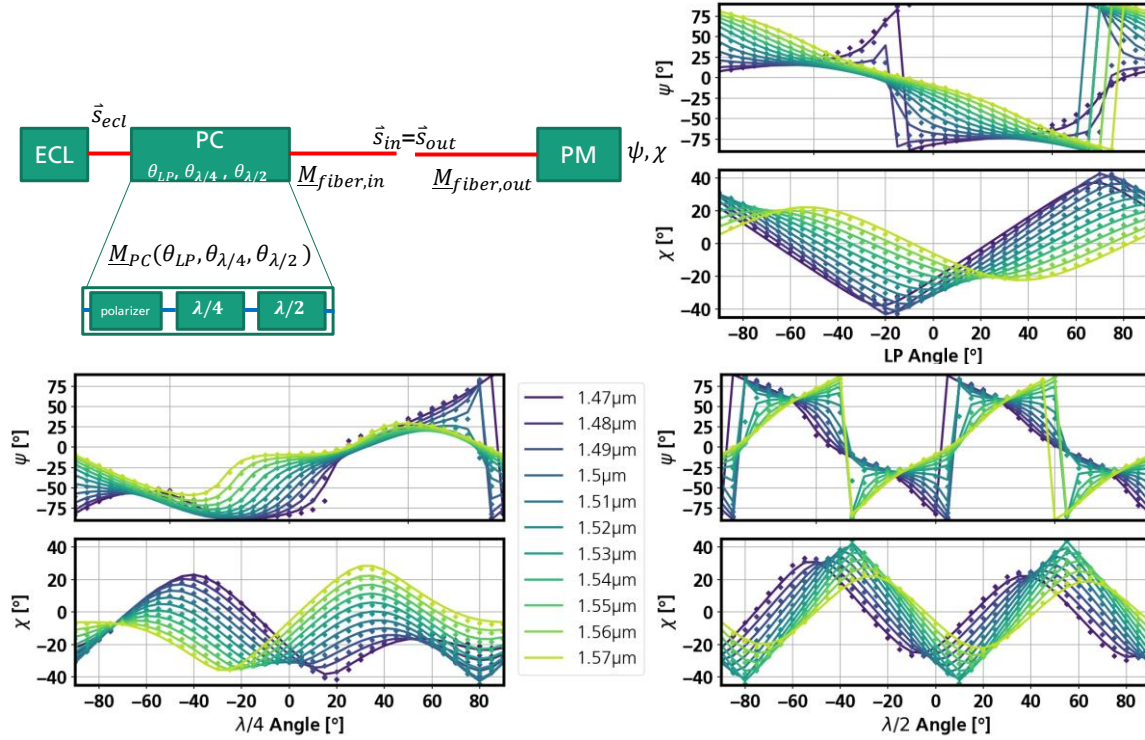


Figure 4-6. Validation of the setup calibration for the output path. The setup is operated in the back-to-back configuration (top left). The three elements in the PC are rotated, the angles of the polarization ellipse at the polarimeter ψ, χ are recorded. The solid lines show the values predicted by the calibrated model, the markers represent the actual measurements. The plots show the sweeps of the linear polarizer (top right), quarter waveplate (bottom left) and half waveplate (bottom right). In each plot, the other two angles are set to 0° .

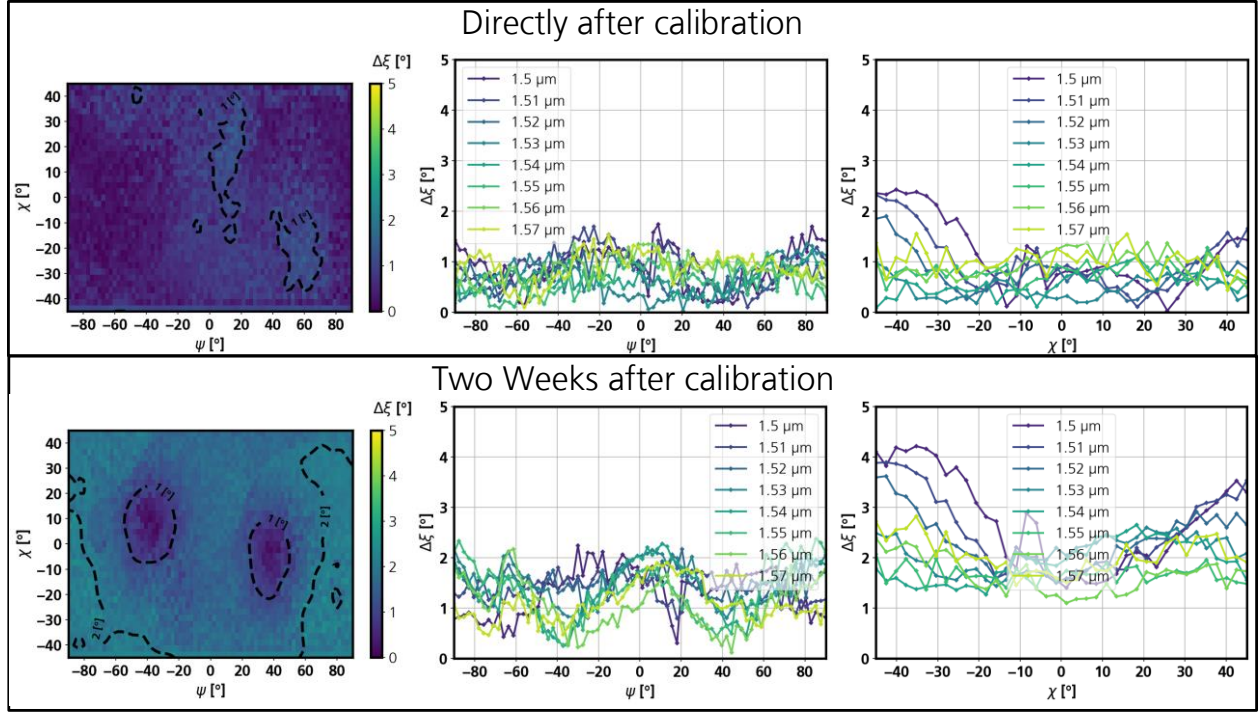


Figure 4-7. Validation of the setup core functionality: setting \vec{s}_{in} (characterized by $\psi = \psi_{in}$ and $\chi = \chi_{in}$) and measuring \vec{s}_{out} . The setup is operated back-to-back, so ideally $\vec{s}_{in} = \vec{s}_{out}$. The measure for the deviation between \vec{s}_{in} and \vec{s}_{out} is their central angle $\Delta\xi$ on the Poincaré sphere. The heatmap on the left shows the deviation across all angles at a wavelength of $1.55 \mu\text{m}$. Slices along $\chi = 0$ and $\psi = 0$ are shown in the middle and right plots, respectively (including wavelength dependency). The position on the Poincaré sphere is accurate within 2° , or 30 dB in terms of PER across the whole C-band. Two weeks after calibration the performance is slightly degraded, but the errors are still below 5° or better than 21 dB PER.

As can be seen in figure 4-7, the overall angular error is below 2° across the entire C-band and for all target angles. By carefully fixating all fibers to the optical bench and avoiding long paths, the calibration accuracy can be maintained over more than a week. The setup is located in an air-conditioned grey room area. The deviations between model and measurement (see figure 4-7) stays well below 5° over the course of two weeks in the entire C-band and beyond.

4.1.2 Solving the Polarimetric Measurement Equation

With 4.1.1, it is possible to set any arbitrary polarization ellipse at the input of a PIC and to measure the polarization ellipse at its output. I.e., it is possible to control \vec{s}_{in} and to measure \vec{s}_{out} . In general, the PIC is characterized by its Müller matrix as follows:

$$\vec{s}_{out} = \underline{M}_{PIC} \vec{s}_{in} \quad (4.10)$$

To determine \underline{M}_{PIC} , at least four different \vec{s}_{in} have to be set and \vec{s}_{out} has to be recorded for each of those. Since each measurement yields four linear equations from (4.10), the four measurements yield 16 equations which allow solving for all elements of the 4x4 matrix \underline{M}_{PIC} . Suppose we carry out N measurements, each with an input polarization $\vec{s}_{in,q}$, with

$q = 0, 1, \dots, 15$. We record each output polarization $\vec{s}_{out,q}$. By defining N analyzer vectors \vec{a}_q , N measured powers are defined as:

$$P_q = \vec{a}_q^T \cdot \vec{s}_{out,q} = \vec{a}_q^T \underline{M}_{PIC} \vec{s}_{in,q} \quad (4.11)$$

Note that because we always measure all four elements of $\vec{s}_{out,q}$, we really only do $N/4$ measurements but still get N different resulting powers. When re-writing \underline{M}_{PIC} as a vector \vec{m} , we can write the powers as

$$P_q = \vec{w}_q \cdot \vec{m} = \begin{pmatrix} a_{q,0} s_{in,q,0} \\ a_{q,0} s_{in,q,1} \\ a_{q,0} s_{in,q,2} \\ a_{q,0} s_{in,q,3} \\ a_{q,1} s_{in,q,0} \\ \vdots \\ a_{q,3} s_{in,q,3} \end{pmatrix} \cdot \begin{pmatrix} m_{00} \\ m_{01} \\ m_{02} \\ m_{03} \\ m_{10} \\ \vdots \\ m_{33} \end{pmatrix} \quad (4.12)$$

Finally, all powers can be absorbed in one vector \vec{P} and the \vec{w}_q are interpreted as rows of a matrix \underline{W} :

$$\vec{P} = \underline{W} \vec{m} \quad (4.13)$$

This result is in literature commonly referred to as the polarimetric measurement equation, [26], [84]. \underline{W} is the polarimetric measurement matrix. A necessary condition for this method to correctly yield \underline{M}_{PIC} is that \underline{W} has to be of rank 16. To achieve this, we use the following analyzer vectors \vec{a}_i :

$$\vec{a}_0, \dots, \vec{a}_3 = \begin{pmatrix} 1 \\ 0 \\ 0 \\ 0 \end{pmatrix}; \vec{a}_4, \dots, \vec{a}_7 = \begin{pmatrix} 0 \\ 1 \\ 0 \\ 0 \end{pmatrix}; \vec{a}_8, \dots, \vec{a}_{11} = \begin{pmatrix} 0 \\ 0 \\ 1 \\ 0 \end{pmatrix}; \vec{a}_{12}, \dots, \vec{a}_{15} = \begin{pmatrix} 0 \\ 0 \\ 0 \\ 1 \end{pmatrix} \quad (4.14)$$

Four measurements are performed with the input polarizations:

$$\vec{s}_{in,0}, \vec{s}_{in,4}, \vec{s}_{in,8}, \vec{s}_{in,12} = \begin{pmatrix} 1 \\ 1 \\ 0 \\ 0 \end{pmatrix}; \vec{s}_{in,1}, \dots, \vec{s}_{in,13} = \begin{pmatrix} 1 \\ 0 \\ 1 \\ 1 \end{pmatrix}; \vec{s}_{in,2}, \dots, \vec{s}_{in,14} = \begin{pmatrix} 1 \\ 0 \\ 0 \\ 1 \end{pmatrix}; \vec{s}_{in,3}, \dots, \vec{s}_{in,15} = \begin{pmatrix} 1 \\ -1 \\ 0 \\ 0 \end{pmatrix} \quad (4.15)$$

Again, even though this gives 16 independent “measured” powers, only four physical measurements are carried out. Each one gives four virtual measurements by virtue of four different analyzer vectors. With this, it can be shown that the polarimetric measurement equation simplifies and can be solved for \vec{m} :

$$\begin{pmatrix} m_{0,0} \\ m_{1,0} \\ m_{2,0} \\ m_{3,0} \\ m_{0,1} \\ m_{1,1} \\ m_{2,1} \\ m_{3,1} \\ m_{0,2} \\ m_{1,2} \\ m_{2,2} \\ m_{3,2} \\ m_{0,3} \\ m_{1,3} \\ m_{2,3} \\ m_{3,3} \end{pmatrix} = \frac{1}{2} \begin{pmatrix} S_{out,0,0} + S_{out,3,0} \\ S_{out,0,0} - S_{out,3,0} \\ -S_{out,0,0} + 2S_{out,1,0} - S_{out,3,0} \\ -S_{out,0,0} + 2S_{out,2,0} - S_{out,3,0} \\ S_{out,0,1} + S_{out,3,1} \\ S_{out,0,1} - S_{out,3,1} \\ -S_{out,0,1} + 2S_{out,1,1} - S_{out,3,1} \\ -S_{out,0,1} + 2S_{out,2,1} - S_{out,3,1} \\ S_{out,0,2} + S_{out,3,2} \\ S_{out,0,2} - S_{out,3,2} \\ -S_{out,0,2} + 2S_{out,1,2} - S_{out,3,2} \\ -S_{out,0,2} + 2S_{out,2,2} - S_{out,3,2} \\ S_{out,0,3} + S_{out,3,3} \\ S_{out,0,3} - S_{out,3,3} \\ -S_{out,0,3} + 2S_{out,1,3} - S_{out,3,3} \\ -S_{out,0,3} + 2S_{out,2,3} - S_{out,3,3} \end{pmatrix} \quad (4.16)$$

In this form, all 16 elements $m_{i,j}$ of $\underline{M}_{\text{PIC}}$ can be obtained directly from the four measurements. We use (4.16) for all measurements in this chapter.

To summarize, four the different states from (4.15) are launched into the PIC, namely TE-, +45° linearly-, right-hand circularly and TM-polarized light. From the measured output states, $\underline{M}_{\text{PIC}}$ is obtained via (4.16). Then, the complete polarization behavior of the PIC is known.

4.1.3 Müller Matrix Decomposition

Even though with the previous chapter we can in principle fully describe the polarization properties of a PIC, it remains unclear how to extract tangible properties like birefringence, polarization rotation or PDL. The reason is that the physical interpretation of an experimental Müller matrix is generally not obvious. One way of interpreting a given matrix is to decompose it into simple factors which can then be understood individually. Several authors investigated the possibilities of decomposing experimental Müller matrices [85]–[89]. We will follow Lu’s and Chipman’s method of polar decomposition [85]. They have shown that any experimental \underline{M} can be written as:

$$\underline{M} = \underline{M}_D \underline{M}_A \underline{M}_R \quad (4.17)$$

Where \underline{M}_A represents depolarization and \underline{M}_D and \underline{M}_R are elliptical diattenuators and retarders, respectively. They can be constructed from the diattenuation vector \vec{D} , average transmission T and the retardation vector $\vec{R} = \delta \vec{u}$ as given in appendix A). From the experimental \underline{M} , T and \vec{D} can be directly obtained [85]:

$$T = m_{00} \quad \vec{D} = \frac{1}{m_{00}} \begin{pmatrix} m_{01} \\ m_{02} \\ m_{03} \end{pmatrix} \quad (4.18)$$

From this, we can calculate \underline{M}_D . If we assume non-depolarizing elements, \underline{M}_A becomes the identity. Then, by calculating \underline{M}_D^{-1} , equation (4.17) yields \underline{M}_R , which in turn yields \vec{R} (see appendix A)). Note that \vec{R} is along fast axis of the retarder. The third component of \vec{R}

vanishes for a linear retarder and we get the case from chapter 2.3.3. Any polarization conversion in a given DUT will express itself as an \vec{R} that is neither parallel nor anti-parallel to the s_1 -axis. The former corresponds to a fast axis parallel to the substrate (along TE), while the latter corresponds to a fast axis perpendicular to the substrate (along TM, the usual case for ridge waveguides). A DUT whose \vec{R} and \vec{D} are parallel is said to be homogeneous [85].

In the general case, \underline{M}_A might not be the identity, i.e. the PIC might be depolarizing. An SOA would be an example, as ASE has a stochastic polarization and its phase noise will be imprinted on the relative phase between the two principal polarizations. In this case, the calculation is slightly more tedious, effectively getting extended by the polarizance vector \vec{P} . The decomposition in the depolarizing case is given in [85]. The depolarization power Δ gets defined by:

$$\Delta = 1 - \frac{|\text{trace}(\underline{M}_A) - 1|}{3}, \quad 0 \leq \Delta \leq 1 \quad (4.19)$$

4.1.4 Software Implementation

As mentioned before, the numerics of the Müller/Stokes measurements are implemented in python. Using the bokeh library [90], a web-based interface is written that visualizes in- and output polarization and displays the Müller matrix of a given sample. A screenshot is shown in figure 4-8. It also allows the decomposition of the matrix into its retarding, diattenuating and depolarizing parts, as described in the previous section.

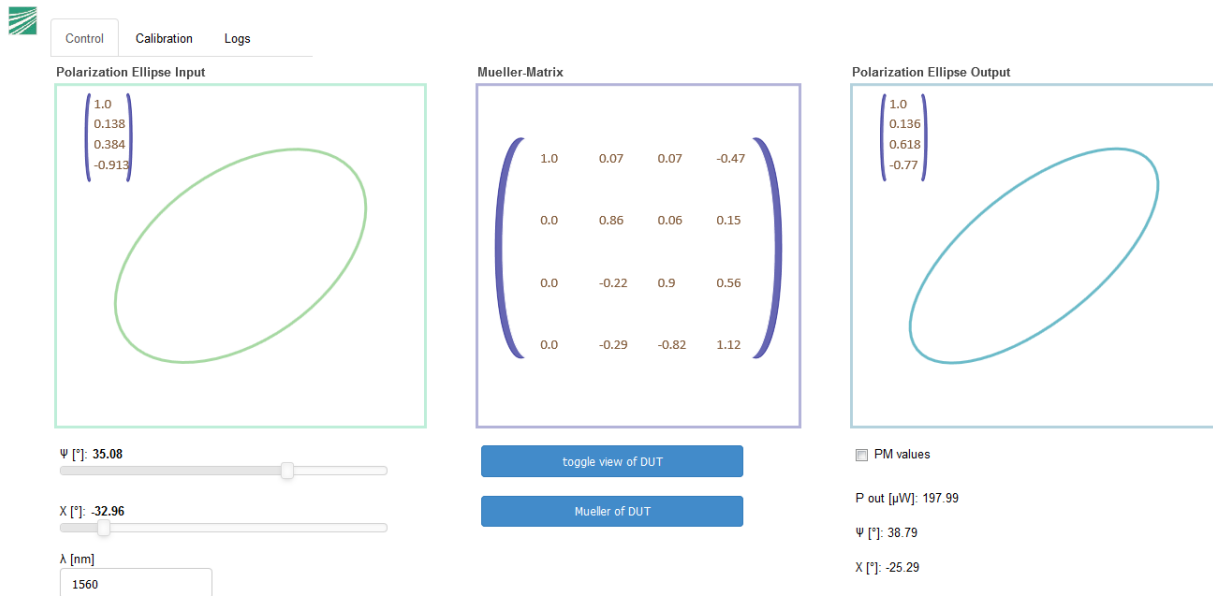


Figure 4-8. Screenshot of the graphical interface for the Stokes measurements. The input polarization can be controlled on the left using two sliders for ψ and χ . The Müller matrix can be measured and is displayed with normalized values in the middle. The right panel shows the current output polarization.

With this, the measurement setup is ready to perform wavelength dependent Müller matrix measurements of any integrated device with just fiber coupling.

4.2 Polarization Rotator Results

With the experimental methodology in place, measurements of actual devices can be carried out. Optical photographs of fabricated PRs are shown in figure 4-9. A scanning electron microscope picture of the asymmetric waveguide used in the PRs is shown in figure 4-10.

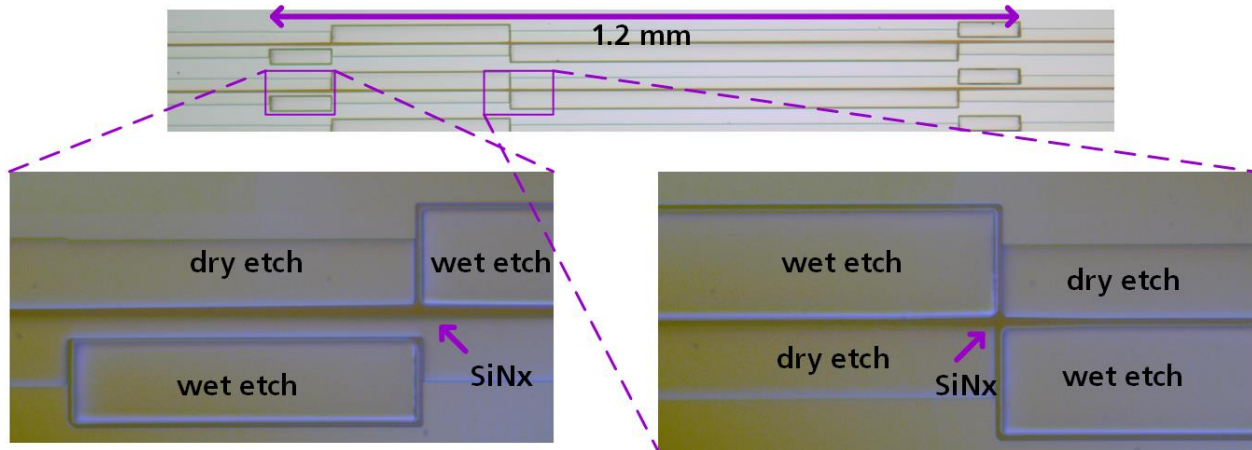


Figure 4-9. Photograph showing an overview of a fabricated 90° PR (top). The two zooms at the bottom show the area around the 100 μm long in- and output taper (bottom left) and the 25 μm long taper in the mid section (bottom right). The dummy etch window at the in- and outputs leads to a more homogeneous etching along the PR. The waveguides are fabricated with a SiN mask.

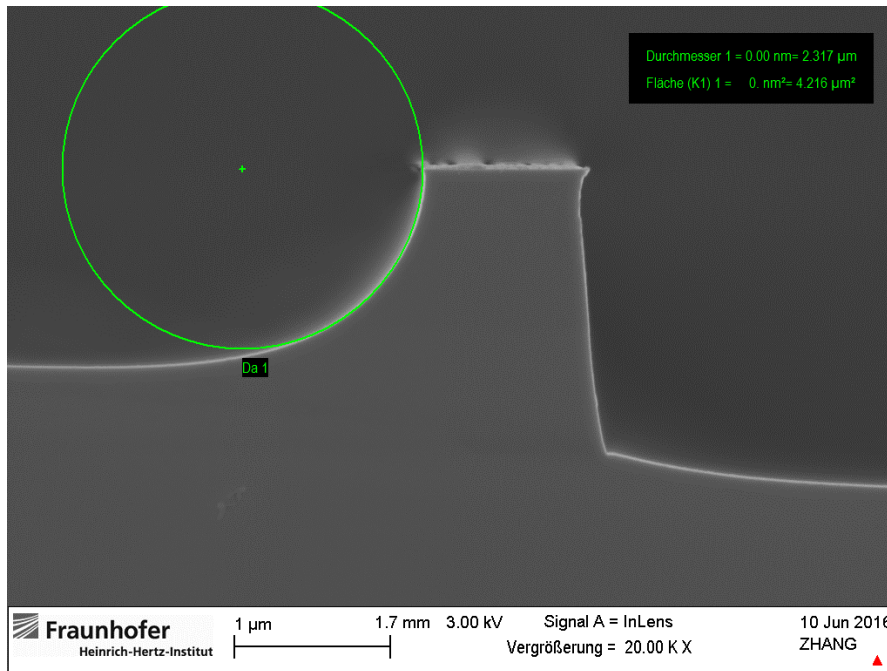


Figure 4-10. Scanning electron microscope (SEM) picture of the asymmetric waveguide cross section. The top width of the waveguide shown is 1 μm . The green inset shows that the sidewall is circular (with a diameter of 2.3 μm).

Results for 90° PRs and 45° PRs are presented in the following two sections.

4.2.1 90° Polarization Rotators

The fabricated polarization rotators are measured on the Stokes space setup as described in chapter 4.1. Therefore, the full Müller matrix is retrieved as a function of wavelength. Because the rotators are fabricated on bars of fixed length, the actual device under test consists of two waveguides with the PR in between. Therefore we can write:

$$\underline{M}_{PIC} = \underline{M}_{WG,out} \cdot \underline{M}_{PR} \cdot \underline{M}_{WG,in} \quad (4.20)$$

We assume that the in- and output waveguides are linear retarders with no rotation. Further, we write the PR itself as a rotated linear retarder with some polarization dependent loss (i.e. diattenuation):

$$\underline{M}_{PR} = \underline{M}_{\delta_{PR}}(\theta_{PR}) \cdot \underline{M}_{PDL} \quad (4.21)$$

A first simple measure for the performance is the PER of the exiting light for incident TM-polarized light. It can easily be shown that

$$PER = \frac{P_{TE}}{P_{TM}} \Big|_{\vec{s}_{in} \cong TM} = \frac{s_{out,0} + s_{out,1}}{s_{out,0} - s_{out,1}} \Big|_{\vec{s}_{in} \cong TM} \quad (4.22)$$

So, by exciting the measured Müller matrix with a TM-polarized input vector, the PER of the device can be calculated. The results in this framework for several devices are shown in figure 4-12.

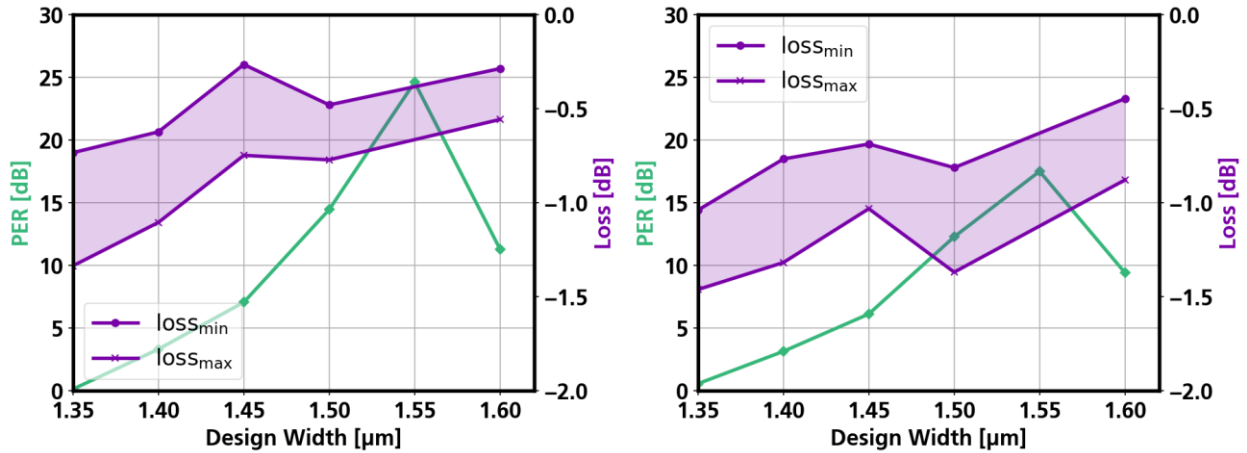


Figure 4-11. PER and loss for designs with different widths at a wavelength of 1.53 μm (left) and 1.55 μm (right). The device with $w=1.55 \mu\text{m}$ has an epitaxial defect in the input waveguide, giving around 8 dB of excess loss. The design width refers to the width of the PR's first section, all other widths (second section, tapers) scale linearly with this width.

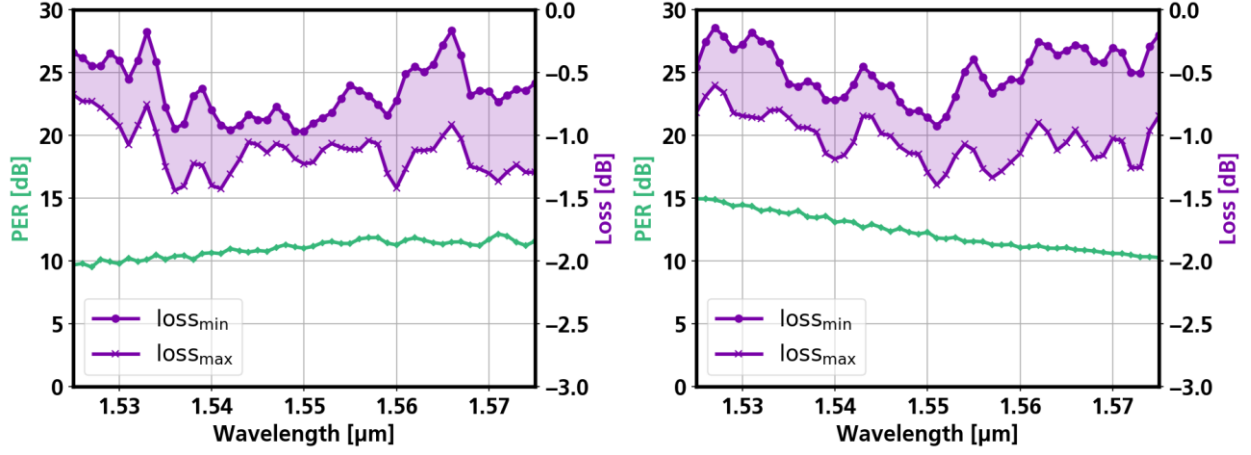


Figure 4-12. Measured PER and insertion loss of the same device from two different wafers. The PER is above 10 dB on both wafers. Both devices have a PDL below 1 dB, with an average loss around 1 dB.

To analyze the PRs further, we want to understand the origins of the PER. We decompose $\underline{\mathbf{M}}_{\text{PIC}}$ into its elliptical retardation and diattenuation components as outlined in section 4.1.3. Thus, we retrieve the retardation vector \vec{R} that emerges from the combination of in- and output waveguides and the actual PR. Since the in- and output waveguides are symmetric, their fast axis will be at 90° with the substrate. So, in the absence of a PR, \vec{R} will be along $-s_1$.

It can be shown geometrically that in the case of an ideal PR (i.e. full polarization conversion), the fast axis \vec{R} of $\underline{\mathbf{M}}_{\text{PIC}}$ will lie in the s_2s_3 -plane. In other words, the fast axis will be at 45° with the substrate in real space or 90° with the s_1 -axis in Stokes space. The total rotation around that axis, δ , should be 180° . Therefore, we take the following quantities to specify the PR performance: the angle enclosed by \vec{R} and the s_1 -axis, and δ . The former is a measure for the rotation of the principal axes, the latter gives the phase retardation between the principal axes. The relationships are illustrated in figure 4-13.

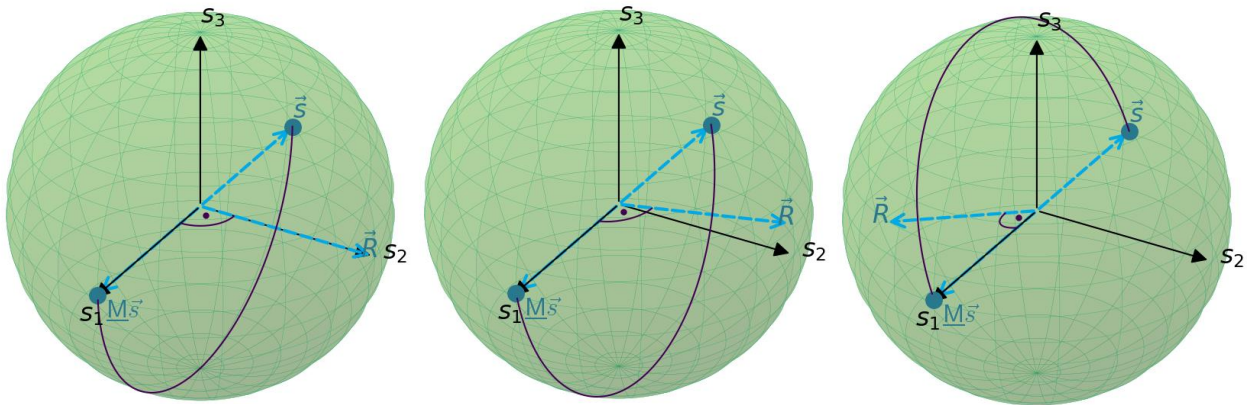


Figure 4-13. Principle of operation of an ideal integrated polarization rotator on incident TM light (\vec{s}). The PR is preceded and followed by non-rotating waveguides of different lengths, i.e. different phase retardations. Left: zero retardation before and behind the PR. The overall PIC then simply rotates around the s_2 axis, i.e. its

fast axis is with 45° to the PIC substrate. Middle: 20° phase retardation before the PR, zero behind. The PIC now rotates around an axis that is not along s_2 anymore, but still at 90° to the s_1 axis. Even when an additional retardation behind the PR is present (50° , right graph), the rotational axis is still at 90° to the s_1 axis, i.e. in the s_2s_3 plane.

The fast axis and retardation of the same devices as in figure 4-12 is shown in figure 4-14. The retardance δ is around 25° too small. This can be explained by the fact that for the design of the devices, the birefringence of the asymmetric waveguide was overestimated. The rational function $\Delta n(w)$ describing the width dependence did not sample accurately enough around the minimum, which is where the PR operates. Thus, the design can be improved by increasing its length accordingly.

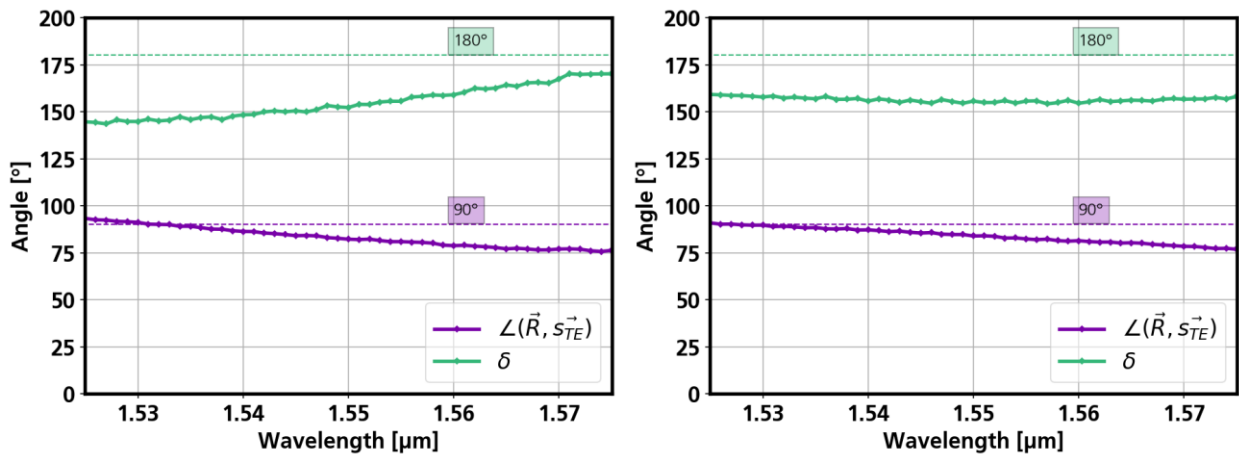


Figure 4-14. Measured retardance δ and fast axis angle $\angle(\vec{R}, \vec{s}_{TE})$ of the same device from two different wafers. The ideal angles for retardance and fast axis are depicted as dashed lines.

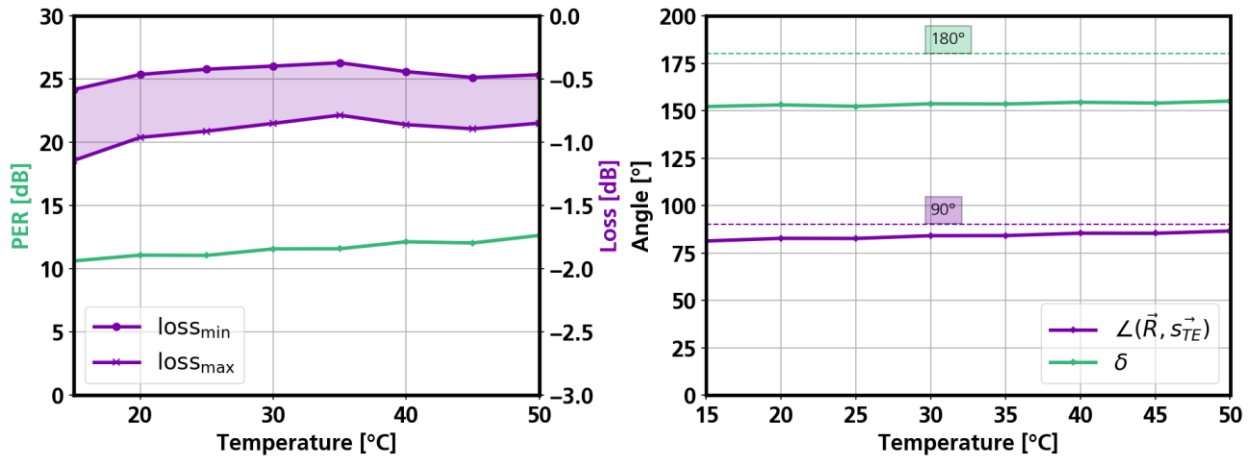


Figure 4-15. Measured dependence of PER and loss (left) and fast axis angle and retardance (right) on temperature for 90° PRs.

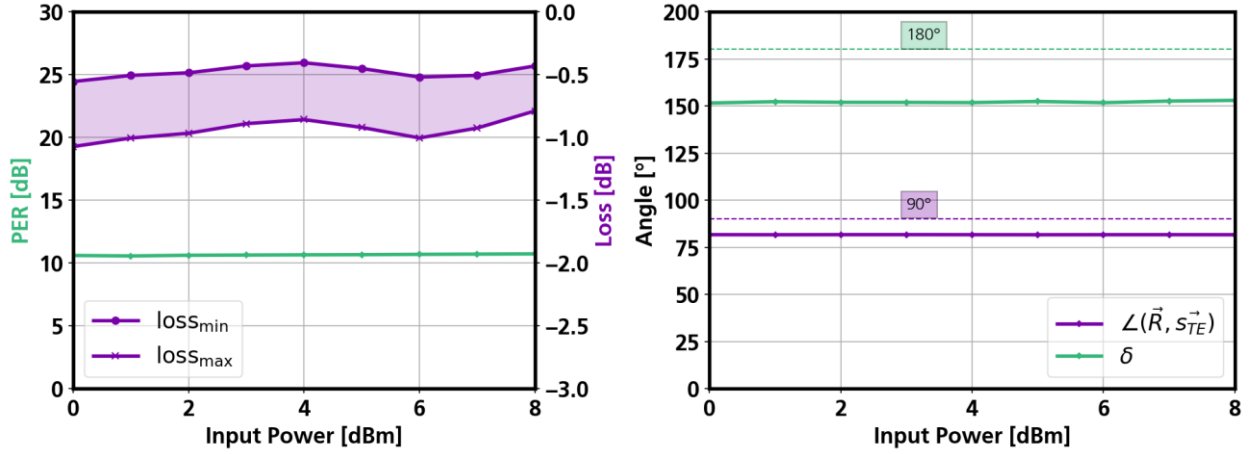


Figure 4-16. Measured dependence of PER and loss (left) and fast axis angle and retardance (right) on input power for 90° PRs.

4.2.2 45° Polarization Rotators

Using the same approach as in the previous section, devices designed for 45° rotation are characterized. Note that the PER should ideally be 0 dB for these devices, as both TE and TM incident light ought to be mapped to a 50/50 mix of TE and TM. ± 1 dB PER corresponds to $\pm 3.3^\circ$ error around the ideal 45°.

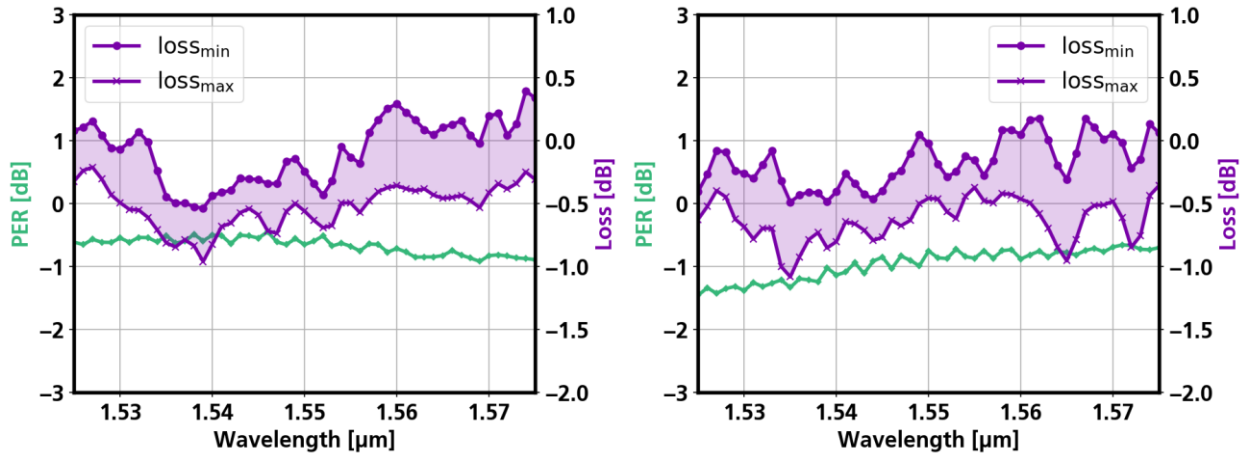


Figure 4-17. Experimental results for 45° polarization rotators. The mask widths are different by 150 nm for the two devices shown. The left device has narrower waveguides. Apart from the widths, the design for both devices is identical, and they are processed on the same wafer. The losses are normalized to straight symmetric waveguides of the same length. For some polarizations and wavelengths, the rotators have less loss than the symmetric waveguides, which is expressed in positive loss values in the plots.

An analysis of the mask width dependence is shown in figure 4-18. The PER stays within ± 1 dB for a mask width deviation of at least 150 nm.

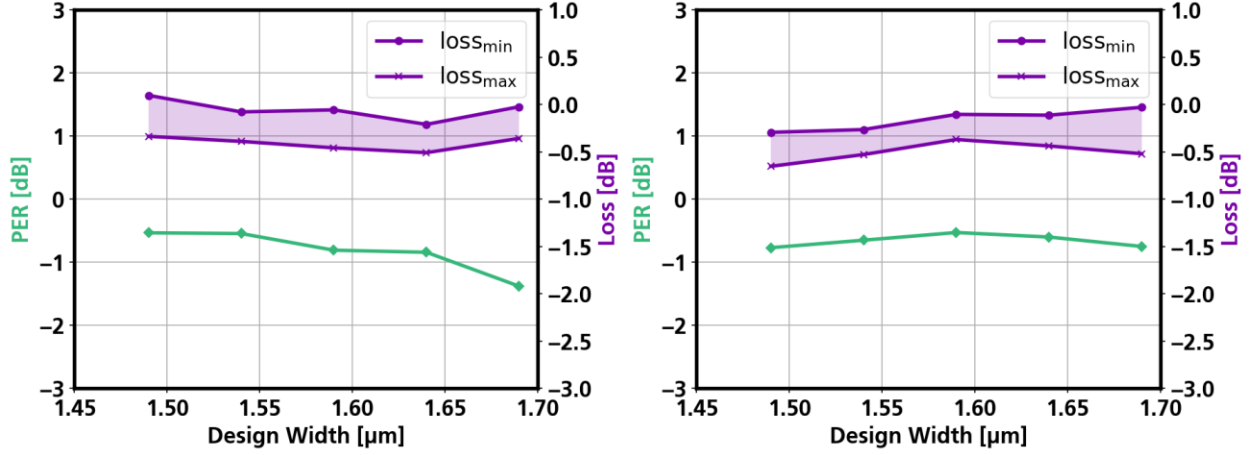


Figure 4-18. Dependence of PER and loss on mask width for 45° PRs. The left shows the dependence for 1.53 μm wavelength, the right for 1.55 μm .

Following the same logic as for the 90° rotators, the Müller matrices of the devices are decomposed to calculate the retardances and fast axes. The result for the same devices as in figure 4-17 are shown in figure 4-19.

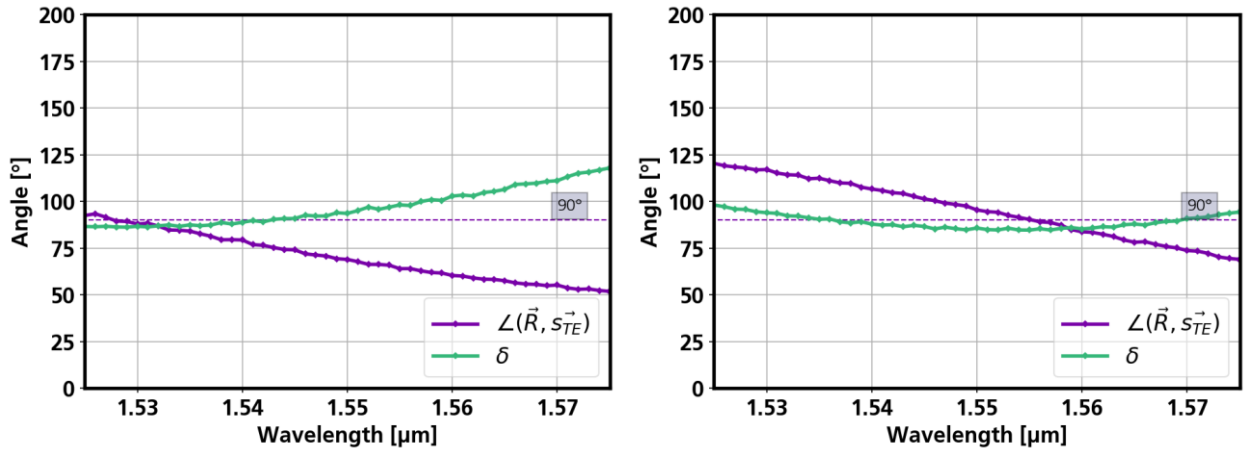


Figure 4-19. Measured retardance δ and fast axis angle $\angle(\vec{R}, \vec{s}_{TE})$ of 45° rotator devices. The mask widths are different by 150 nm in for two devices shown. The ideal angles for retardance and fast axis are depicted as dashed lines (both 90°).

4.3 EAM Results

4.3.1 DC Measurements

The fabricated EAMs are measured the same way as the PRs, with voltage as an additional parameter. The decomposition of the measured Müller matrices again allows the quantification of retardance and diattenuation. Because the slow axis of EAM as well as in- and output waveguides should be along the TM-polarization, this should also be the axis of the retardance and diattenuation vectors. An optical photograph of an exemplary EAM structure is shown in figure 4-20.

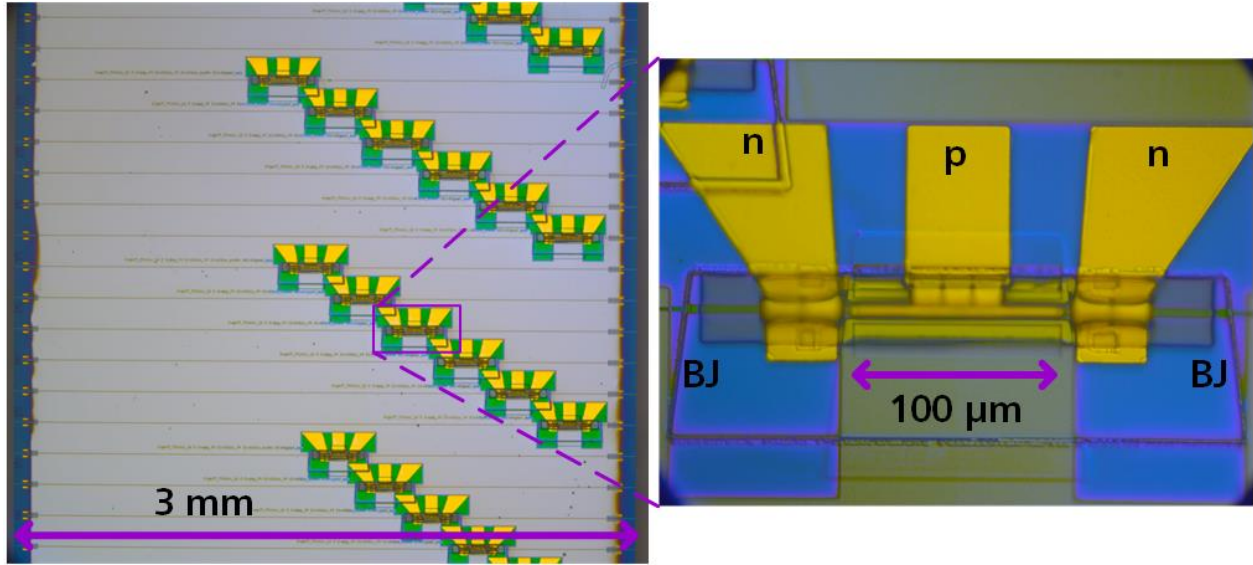


Figure 4-20. Photograph of an entire bar of fabricated EAMs (left) and zoom on a single EAM (right). The bar is anti-reflection coated on both sides. EAMs of different active lengths are fabricated. The right shows a picture of an EAM with an active length of 100 μm .

The absolute birefringence of an EAM is hard to measure because the devices always comprise butt-jointed passive waveguide sections on both sides of the EAM. The measured birefringence cannot be readily divided into the EAM and passive waveguide contributions, respectively. However, applying a voltage to the EAM leaves the passive waveguide birefringence unchanged, so that the birefringent change in the EAM versus voltage can be obtained directly. So, we define a relative birefringence such that it vanishes for zero bias. The corresponding result is shown for two different wavelengths in figure 4-21.

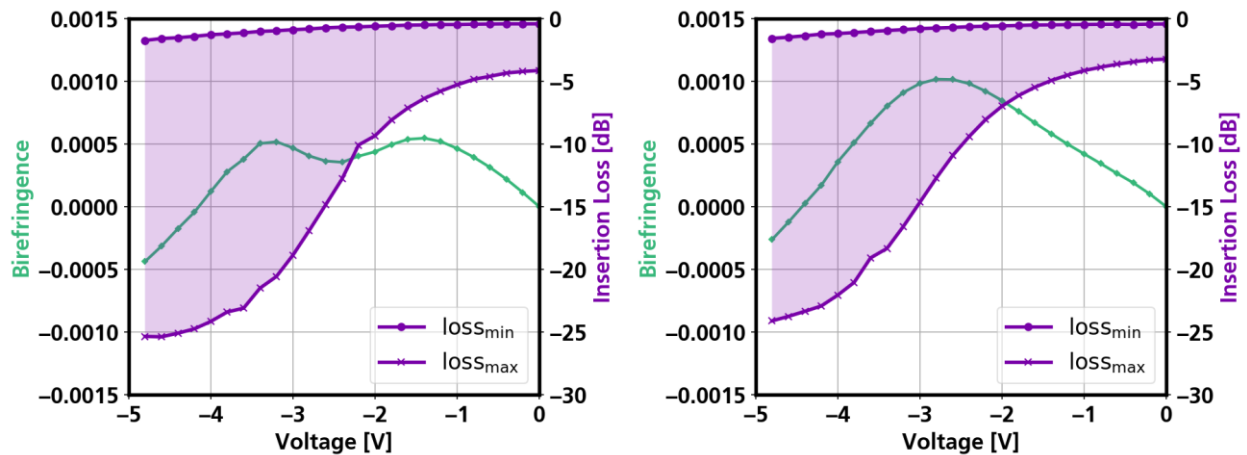


Figure 4-21. Experimental birefringence and PDL for an EAM with 200 μm active length. Voltage dependences are shown for two different wavelengths: 1.565 μm (left) and 1.57 μm (right). The chip substrate is at 20°C, 3 dBm are launched into the device.

A summary of the EAM measured wavelength dependence is shown in figure 4-22. A slight dependence on input power is also found, as shown in figure 4-23. Higher input powers

tend to increase the achievable extinction. This can be attributed to the larger photocurrents that are flowing, corresponding to a higher concentration of heavy holes in the active layer. Heavy holes can participate in intraband absorption. The photocurrent can also heat up the active region to such an extent that the bandgap shrinks, leading to higher absorption too.

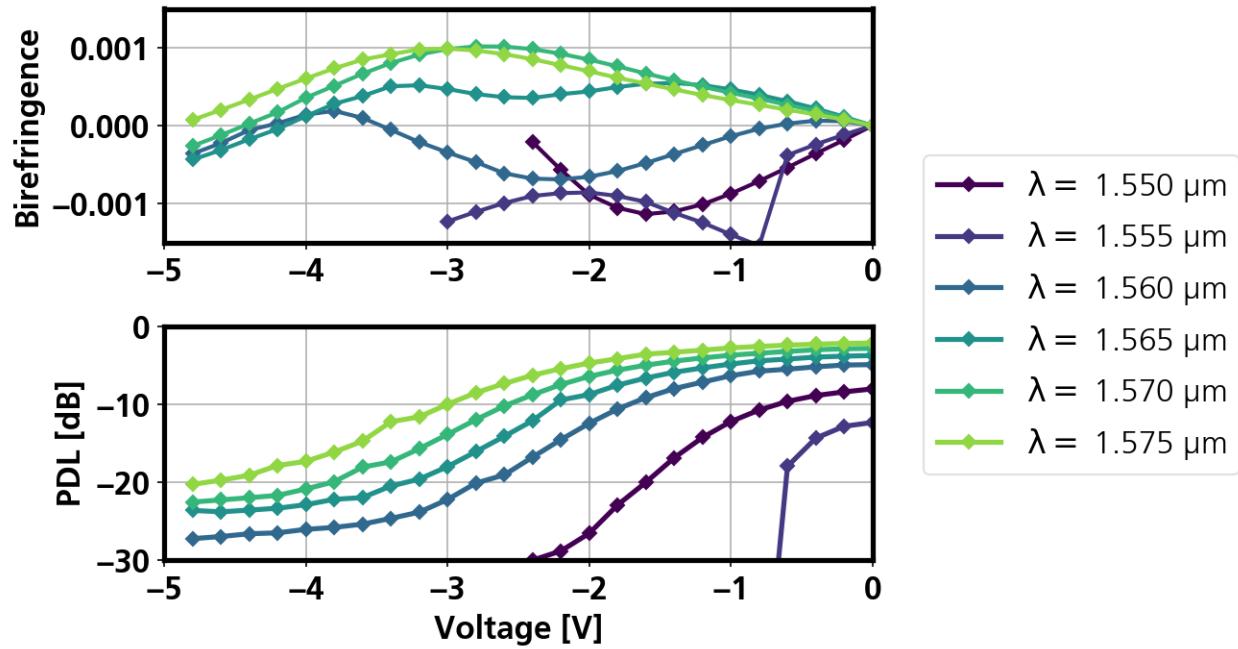


Figure 4-22. Wavelength dependence of birefringence (top) and PDL (bottom). The input power is 3 dBm, the substrate temperature is 20°C.

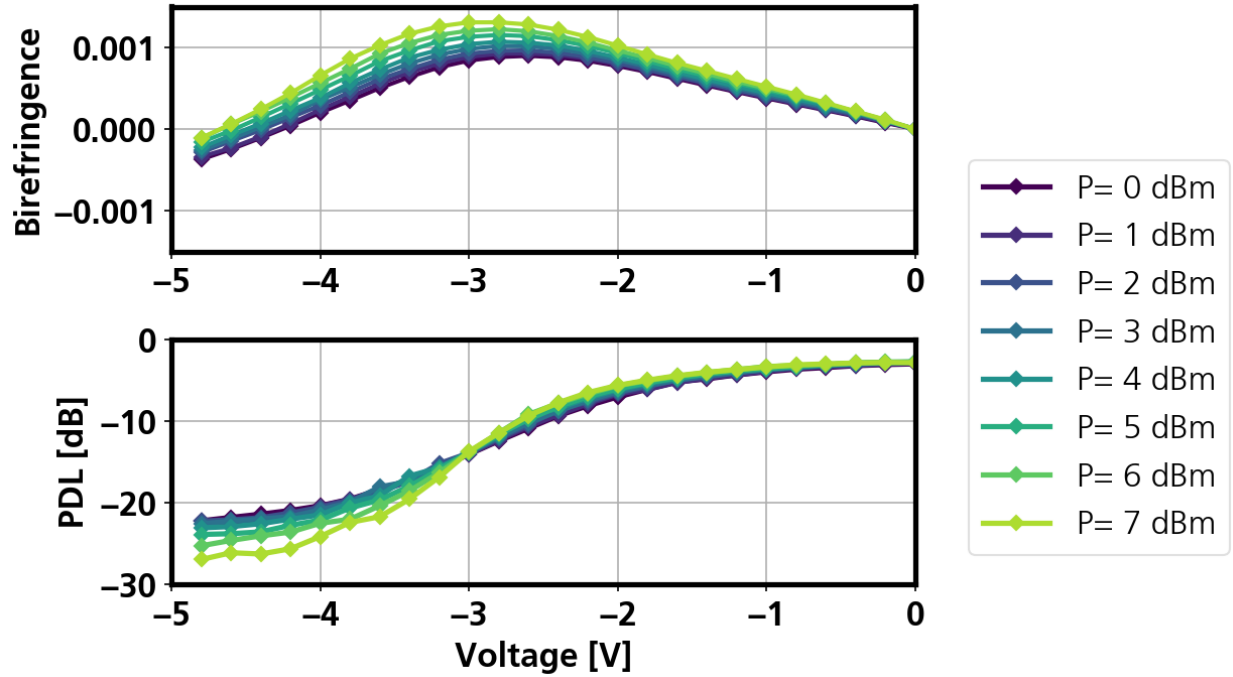


Figure 4-23. Input power dependence of birefringence (top) and PDL (bottom). The wavelength is $1.57 \mu\text{m}$, the substrate temperature is 20°C .

4.3.1.1 Extraction of Chirp

As suggested by theory in chapter 3.2, the previous section proves that the effective index of the EAM TM mode depends much less on reverse bias than the TE index. The same is true for the absorption of the two modes. Mathematically:

$$\frac{\partial n_{TE}}{\partial V} - \frac{\partial n_{TM}}{\partial V} \approx \frac{\partial n_{TE}}{\partial V}; \quad \frac{\partial \alpha_{TE}}{\partial V} - \frac{\partial \alpha_{TM}}{\partial V} \approx \frac{\partial \alpha_{TE}}{\partial V} \quad (4.23)$$

So, it follows that:

$$\frac{\partial n_{TE}}{\partial \alpha_{TE}} \approx \frac{\partial \Delta n}{\partial PDL} \quad (4.24)$$

In other words, the measured birefringence and PDL offer a good approximation for the chirp parameter. We use the definition that is sometimes referred to as Henry factor or simply chirp, which we then may rewrite as follows:

$$\nu = 2 \frac{\partial \phi}{\partial \alpha} \approx \frac{4\pi}{\lambda} \frac{\partial \Delta n}{\partial PDL} \quad (4.25)$$

With the PDL in natural logarithmic scale. So, in the approximation of (4.23), the chirp can be simply deduced from Müller measurements. This may be useful in many circumstances since (4.23) is a good approximation for most typical MQW-based devices. The extracted chirp parameter of a $200 \mu\text{m}$ long EAM is given in figure 4-24.

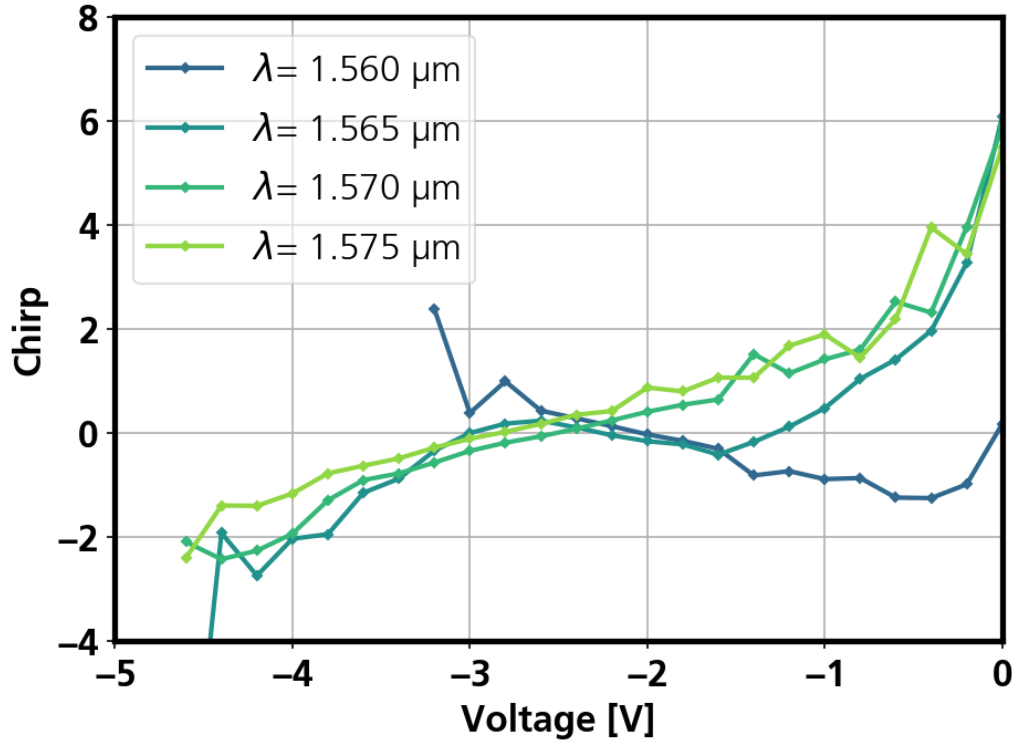


Figure 4-24. EAM chirp extracted via (4.25). The chirp parameter crosses zero at around 2.8 V for most wavelengths. At bias-wavelength combinations that yield too low output power, the Müller matrix and therefore the chirp could not be determined due to the polarimeter sensitivity.

The measured chirp shows typical behavior, starting with positive values for small voltages and crossing zero at higher voltages. The crossing moves to lower voltages with lower wavelengths, as the photon energy moves closer to the band gap.

4.3.2 Small Signal Measurements

To determine the electro-optic bandwidth of the EAMs, a lightwave component analyzer (LCA) is used. It is essentially a vector network analyzer (VNA) with a calibrated electro-optic frontend to characterize the frequency-dependent scattering matrix of electro-optic components. A schematic of the setup that was used for the measurements is shown in figure 4-25.

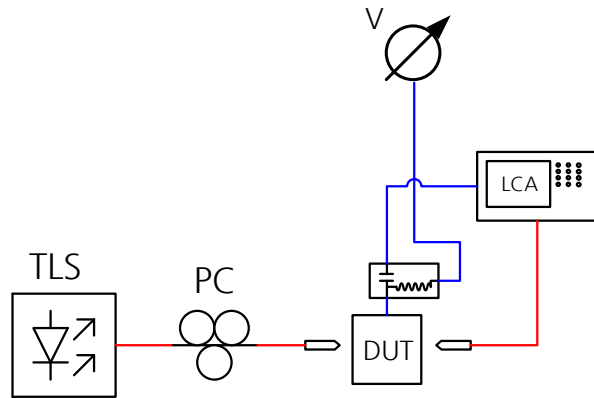


Figure 4-25. Setup used for the electro-optic small signal measurements. The LCA consists of a VNA and a calibrated photodetector. A reverse bias voltage is applied via an external bias-T.

Measured frequency responses for a 200 μm long EAM are shown in figure 4-26. A modulated electrical power of -8 dBm (100 mV peak-to-peak) is applied to the EAM. The figure includes an overview of the dependence of bandwidth on bias, wavelength, temperature and optical power. To allow a reliable determination of the 3 dB bandwidth f_{3dB} even when the power received by the LCA is low (i.e. the signal is noisy), a moving average filter is used. It averages across 10 points, 1600 points are recorded by the LCA. The electro-optic bandwidth is found to be highest at a wavelength 1.569 nm, a temperature of 20°C and around 6 dBm input power. The optimum bias is around -3.5 V.

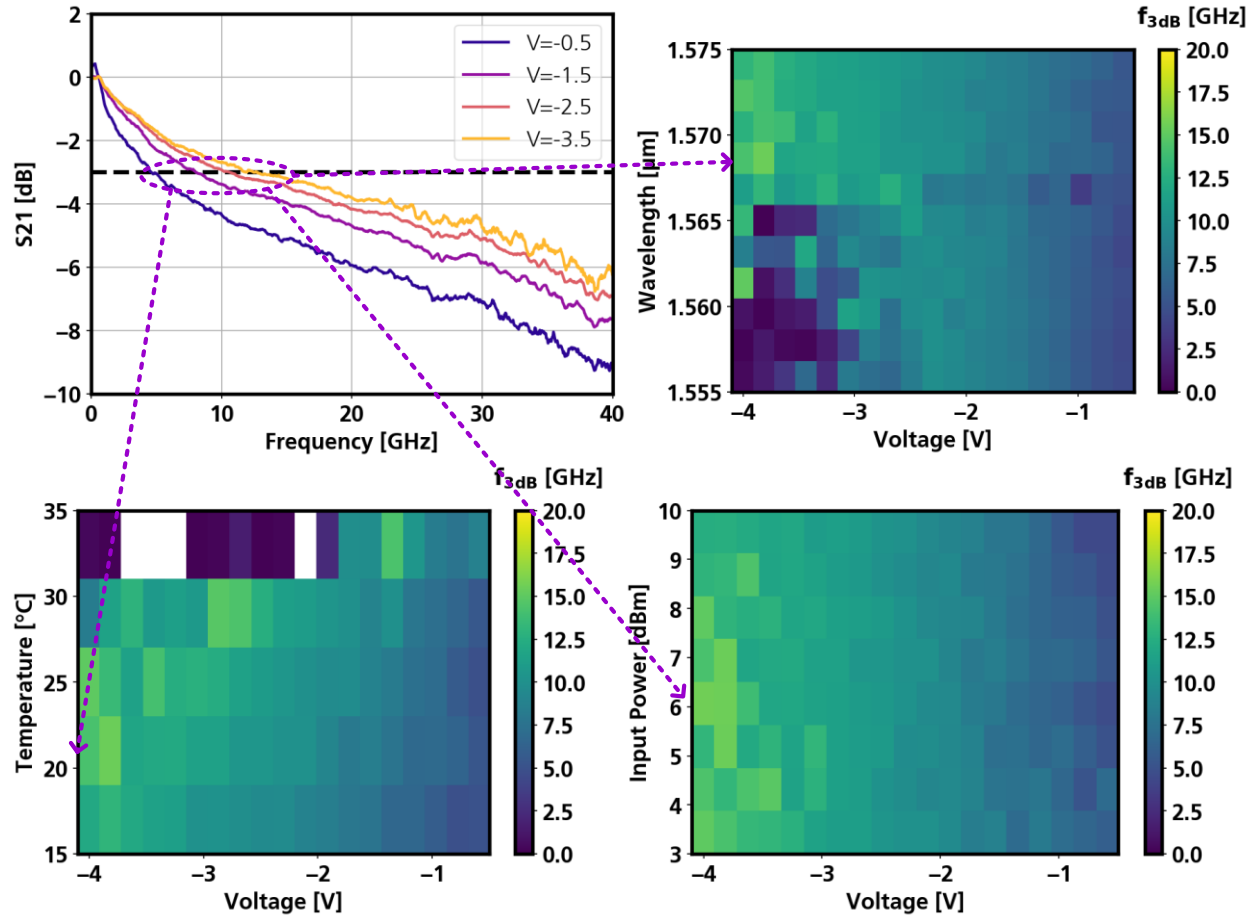


Figure 4-26. Top left: measured electro-optic frequency responses of a 200 μm long EAM at different bias voltages. The EAM is operated at a wavelength of 1.569 μm, 20°C and 6 dBm input power. The color maps show the 3 dB bandwidth dependence on wavelength (top right), temperature (bottom left) and input power (bottom right).

The highest achievable bandwidth is around 17 GHz. To compare this to the simulations of the previous chapter, we recall that figure 3-23 suggest 1.5 nF/m at biases above -3 V. So a 200 μm long device should give 0.3 pF. Together with the measured series resistance of 25 Ω, the theoretical RC limited bandwidth is 21 GHz.

4.3.3 Large Signal Measurements

The setup used for the small signal measurements is extended to enable NRZ OOK. An electrical PRBS source is used to generate a 39 Gbit/s PRBS of length $2^{31} - 1$ bits. The electrical signal from the PRBS is slightly impaired, as shown in figure 4-27. The EAM is operated at 1565 nm, 20°C and a bias voltage of -2.5 V. A clean eye opening is obtained as seen in figure 4-28, but the double-rails from the electrical signal get enhanced. The extinction ratio is 4.3 dB. The eye is recorded with a high speed photodetector and a digital communications analyzer (DCA).

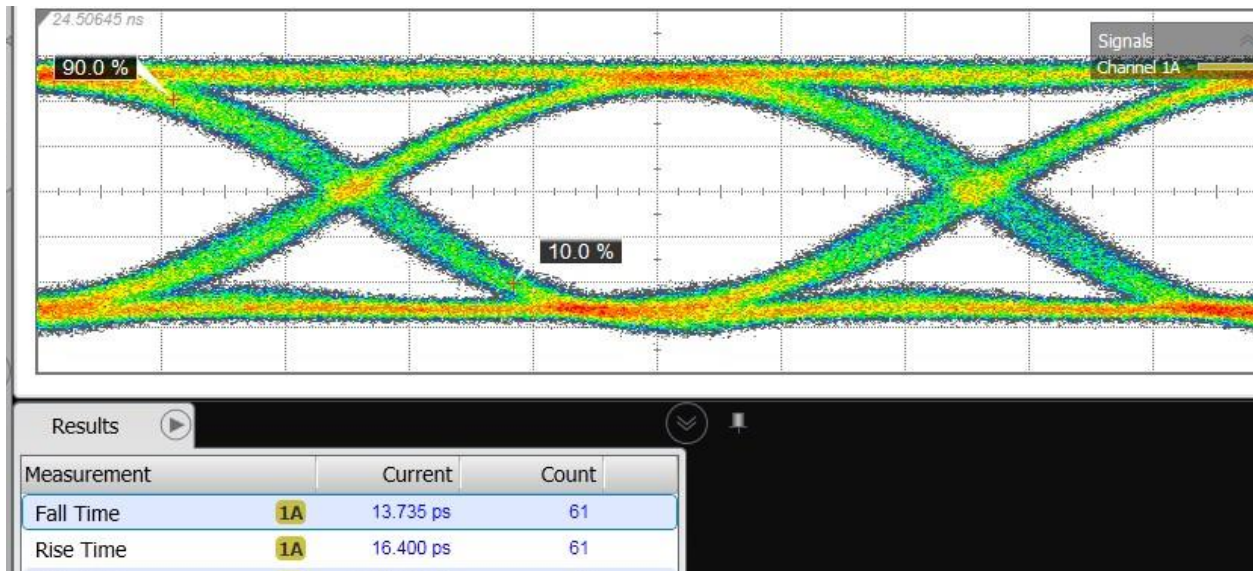


Figure 4-27. Electrical eye diagram at 39 Gbit/s generated by the PRBS. The eye shows double-rail behavior.

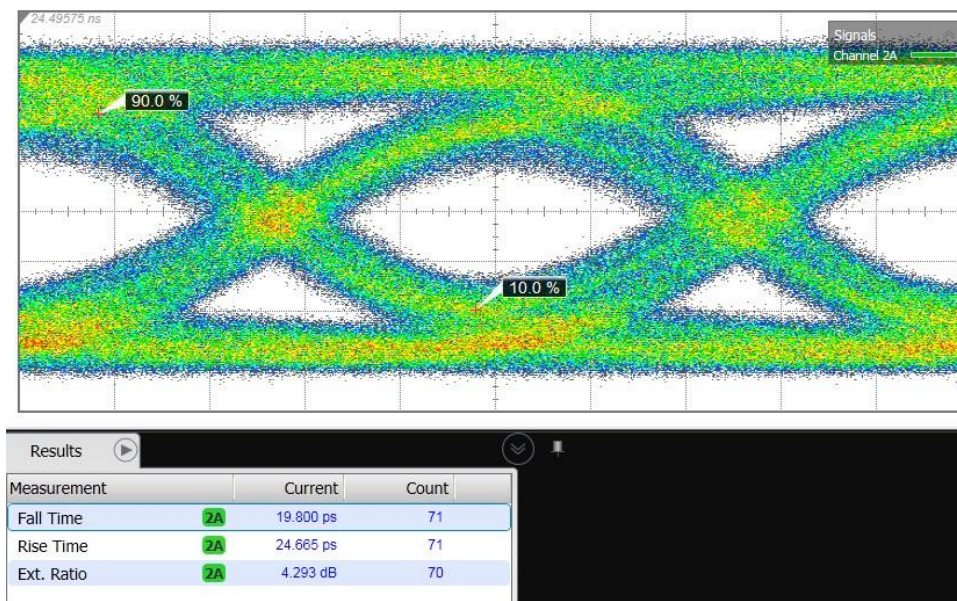


Figure 4-28. Measured eye diagram generated by an EAM at 39 Gbit/s. The double-rail features stem from the slightly impaired electrical signal that is generated by the PRBS source.

4.4 DP EAM Results

A SEM picture of a fabricated DP EAM is shown in figure 4-29. It is colorized for clarity.

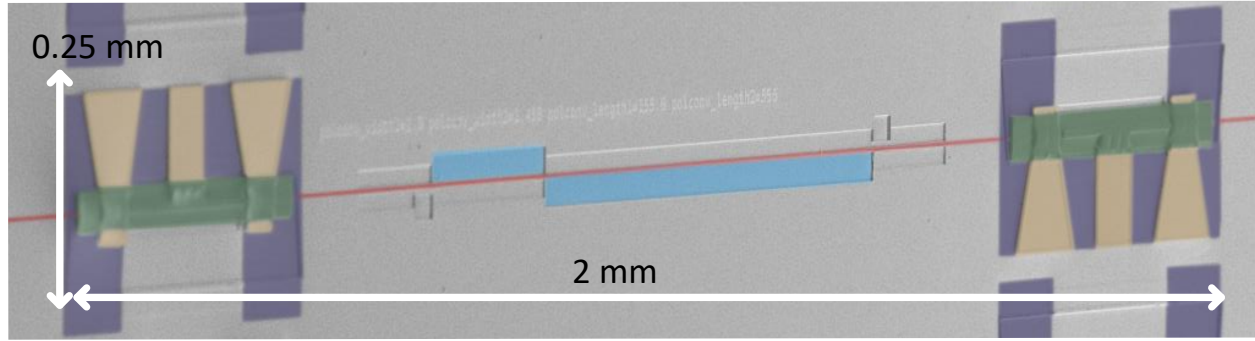


Figure 4-29. Colorized SEM photograph of a manufactured DP EAM. The blue boxes are the windows for the PR wet etch, the red line indicates the waveguide. The active areas are covered in BCB (green), the Au contacts (yellow) reside on SiN_x (purple) for electrical isolation.

4.4.1 DC Measurements

For the DC characterization, the fabricated device is again characterized via the Stokes/Müller formalism. The Müller matrix of the integrated DP EAM is recorded as a function of the two bias voltages of the respective EAMs.

As a first analysis, the DP EAM Müller matrix is decomposed according to 4.1.3 into its retarding and diattenuating constituents. A detailed visualization of \vec{D} is shown in figure 4-30.

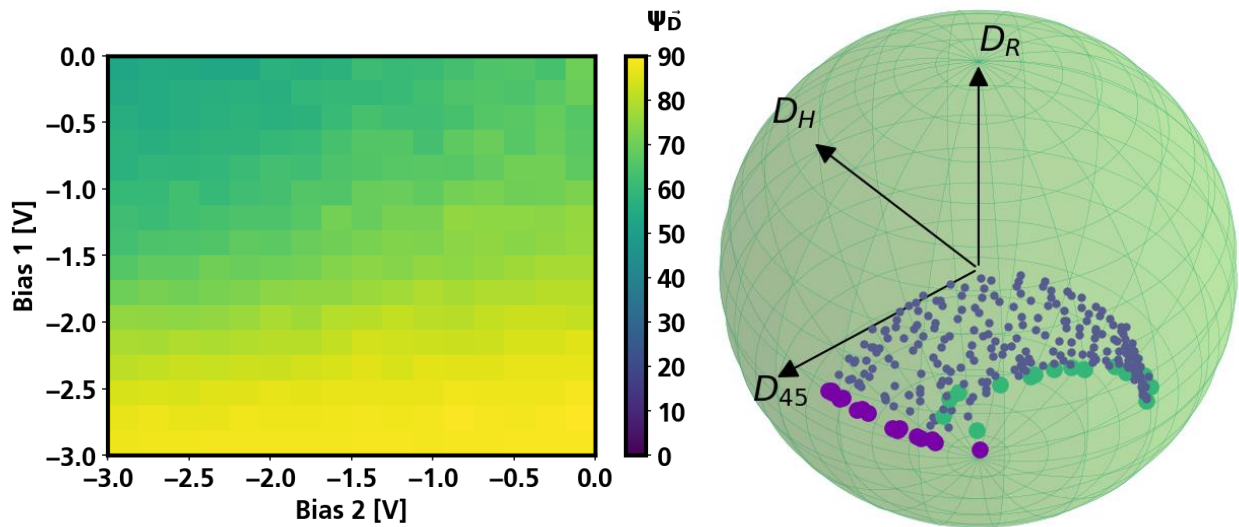


Figure 4-30. Dependence of the normalized diattenuation vector \vec{D} of the DP EAM on the bias voltages. The color map on the left shows the dependence of the vector longitude $\psi_{\vec{D}}$. The left plot shows the position of \vec{D} on the Poincaré sphere. Green points indicate that the second bias is zero, purple points indicate that the first bias is zero. The smaller blue points correspond to both EAMs being biased. Each pixel on the left as a corresponding dot on the right Poincaré sphere. The wavelength is 1.575 μm , the input power 8 dBm and the substrate temperature is 20°C.

For a certain incident Stokes vector, the resulting output polarization as a function of the two bias voltages is calculated via:

$$\vec{s}_{out} = \underline{M}_{PIC}(V_1, V_2) \cdot \vec{s}_{in} \quad (4.26)$$

Ideally, \vec{s}_{out} should be along $[-1 \ 0 \ 0]^T$ and $[1 \ 0 \ 0]^T$ in the two respective bias conditions ($V_1 = 0, V_2 = -3 \text{ V}$) and ($V_1 = -3 \text{ V}, V_2 = 0$). Indeed, when $\vec{s}_{in} \approx [1 \ 0.9 \ 0.05 \ -0.42]^T$, the DP EAM operates this way, as shown in figure 4-31.

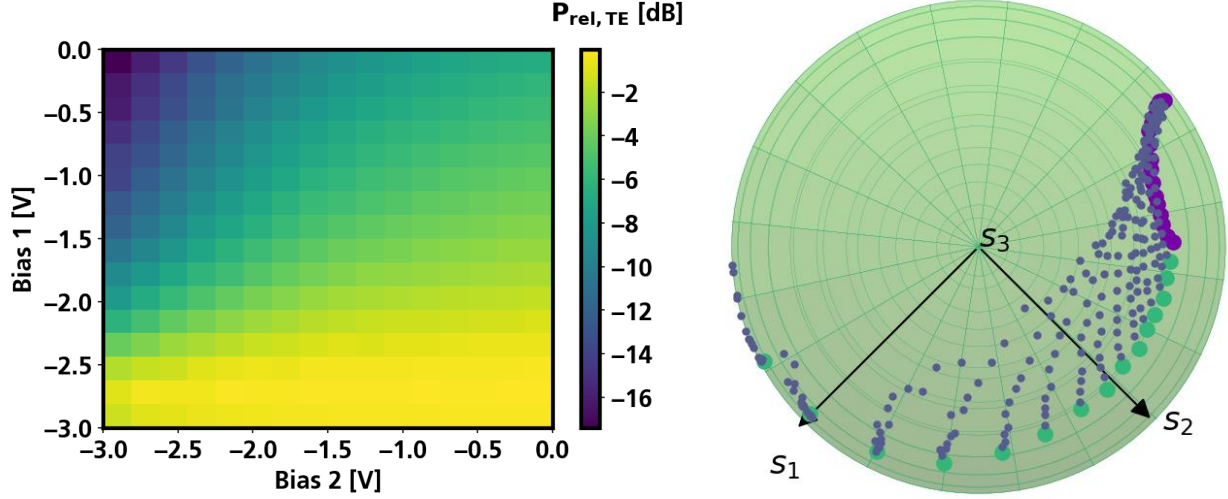


Figure 4-31. Operation of the DP EAM when $\vec{s}_{in} \approx [1 \ 0.9 \ 0.05 \ -0.42]^T$. Left: relative power of the exiting signal as a function of the two bias voltages. Without bias, the TE fraction is around 50%, so its relative power is around -3 dB. Increasing one bias suppresses TE, increasing the other increases the relative TE power by virtue of suppressing the TM fraction. Right: output polarization on the Poincaré sphere for the voltages on the left. Green dots show the SOPs when only sweeping the first EAM, purple dots when only sweeping the second EAM. Blue dots correspond to both EAMs being biased.

With the results in figure 4-31, it is shown experimentally that the device can indeed modulate two orthogonal polarization states independently. The next section shows how this can be used for PDM communication channels. The DP EAM has an on-chip insertion loss of around 14 dB. Most of this loss originates from the butt-joint transitions between active and passive waveguides, which are measured to be around 3 dB per interface, so 12 dB in total.

4.4.2 Transmission Experiments

4.4.2.1 On-Off Keying

A PDM transmission setup as shown in figure 4-32 is used to demonstrate non return-to-zero (NRZ) OOK transmission in a PDM scheme. A “Mickey mouse”-type polarization controller is used to set the SOP at the DP EAM input. A second one is used to align the modulated PDM signal with the coordinate system of a polarization beam splitter (PBS). A 1 dB coupler is used to tap 20% of the modulated signal and monitor it on an optical spectrum analyzer (OSA). Two high speed photodiodes at the two outputs of the PBS are used to analyze the eye diagrams on a digital communication analyzer (DCA). An erbium-doped fiber amplifier (EDFA) is used in conjunction with an etalon wavelength filter on the receiver side of the setup.

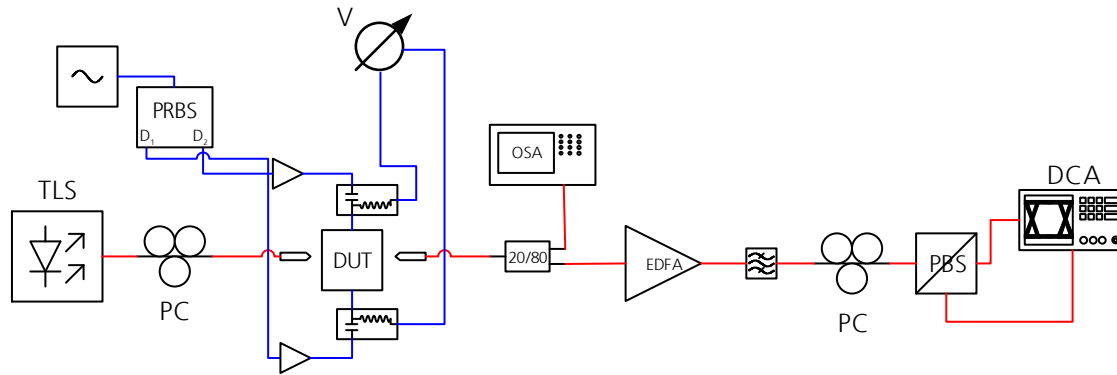


Figure 4-32. Transmission setup used for PDM-OOK. A PRBS source generates two data signals for the two respective EAMs of the DP EAM. Polarization controllers (PC) are used to set the input polarization and to align the output polarization with the PBS coordinate system on the receiver side.

The received optical power is set to 3 dBm. Wavelength is 1570 nm, the TEC is at 20°C.

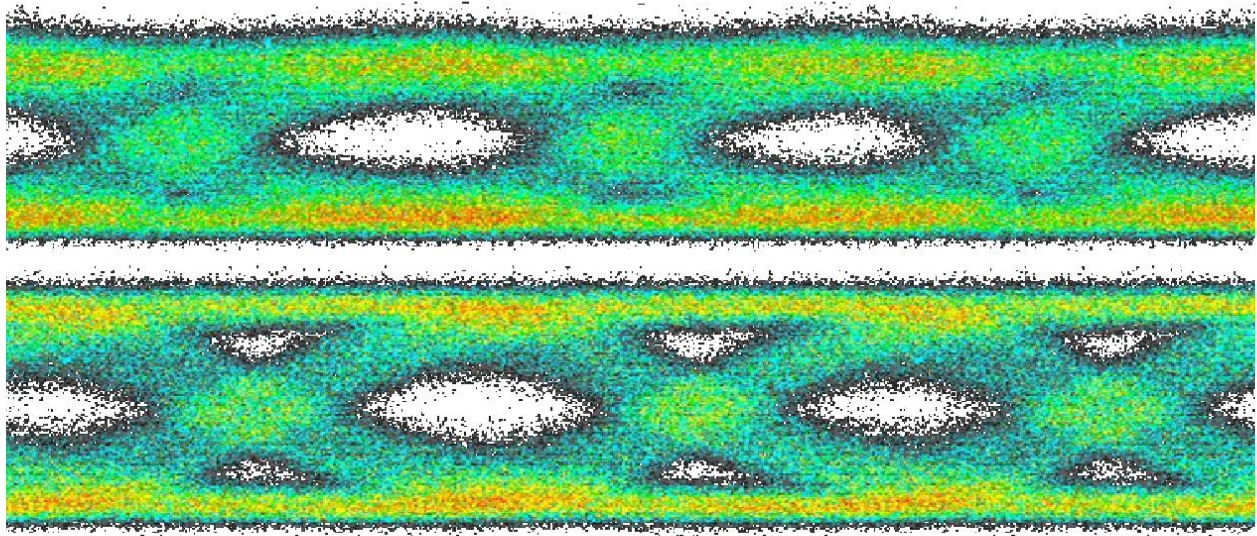


Figure 4-33. Recorded eye diagrams after 32 Gbit/s modulation in the DP EAM, so a total data rate of 64 Gbit/s. The upper eye diagram corresponds to the first EAM, the lower to the second. The extinction ratio is above 6 dB in both polarizations.

4.4.2.2 Quaternary Pulse Amplitude Modulation

To demonstrate 100 Gbit/s transmission, the setup is modified to allow PAM-4 transmission. The new setup is shown in figure 4-34.

To allow offline digital signal processing (DSP), a coherent receiver is used. The receiver is located in another laboratory at HHI of the photonic networks (PN) department, so an in-house fiber link is used to interconnect the two laboratories. The link transmission loss is measured to be 0.9 dB. PN also provided an arbitrary waveform generator (AWG) that is used to generate two PAM-4 signals. A variable optical attenuator (VOA) or an 80 km fiber coil is used to emulate a real transmission link. The receiver itself consists of an integrated

[illegible]

The DSP is used for chromatic dispersion compensation, phase estimation and data-aided channel estimation [91]. The signal is resampled to two samples per symbol. The symbol rate per EAM is 28 GBaud, giving a total $2 \times 2 \times 28 = 112$ Gbit/s gross data rate.

96

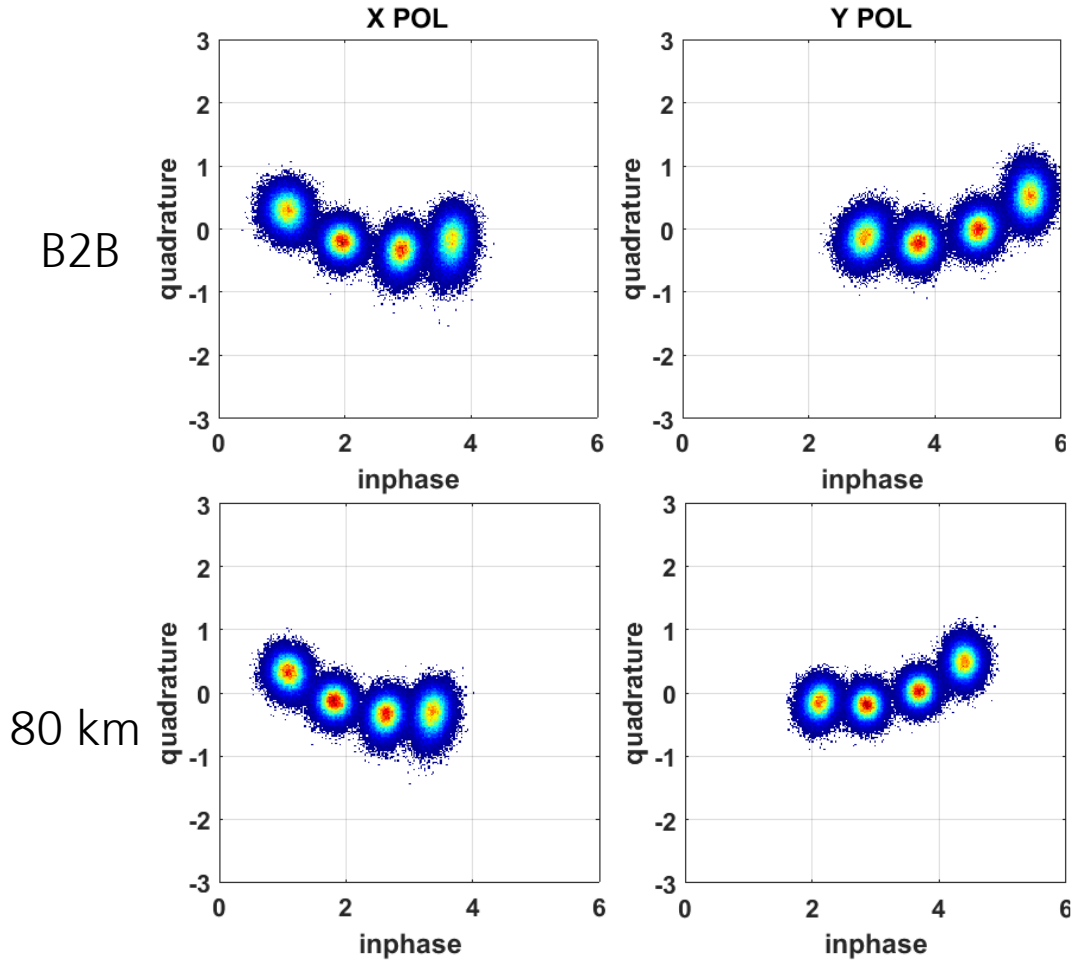


Figure 4-35. Received constellation diagrams of 28 Gbaud PDM-PAM4 in the back-to-back case (top) and after transmission over 80 km of SSMF (bottom).

4.5 DP EML Results

The most complex PIC that is fabricated as part of this work is a complete dual-polarization externally modulated laser (DP EML). Besides the DP EAM, it also monolithically integrates a 45° PR and a distributed feedback (DFB) laser source. For the DFB laser, the standard building block in the integration platform is used. It has an active length of 200 μm . The 45° PR is the device that is characterized in section 4.2.2. An optical photograph of the fabricated DP EML is shown in figure 4-36. It has a footprint of around 1.5 mm² of InP.

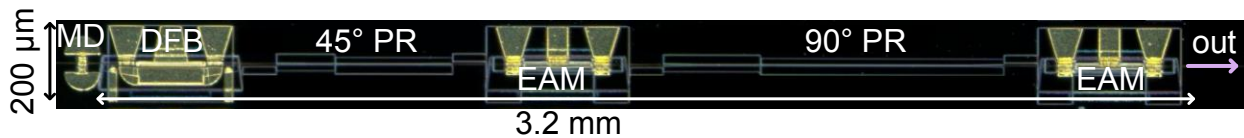


Figure 4-36. Photograph of the Dual Polarization Externally Modulated Laser (DP EML). From left to right: a monitor diode (MD), followed by a DFB. The DFB emits TE polarization. The first polarization rotator (PR) rotates polarization by 45°. The following DP EAM is the same as in the previous section. The output facet is anti-reflection coated. The PIC width of 200 μm is dominated by the RF pads, the length is 3.2 mm.

4.5.1 DC Measurements

Just as the previous devices, the DP EML is characterized using the setup from section 4.1. In the case of the DP EML, the laser source is integrated on chip. So, rather than measuring the Müller matrix of the device, only the Stokes vector exiting the device can be measured. For practical purposes, the DP EML EAMs are contacted with RF probes also for the DC measurements. Only the DFB laser is probed with DC needles. A picture of a contacted DP EML is shown in figure 4-37. An emission spectrum of the unmodulated DP EML is shown in figure 4-38. The DFB has a side mode suppression ratio (SMSR) of over 45 dB, its series resistance is about $25\ \Omega$ and it has a threshold current of 20 mA.

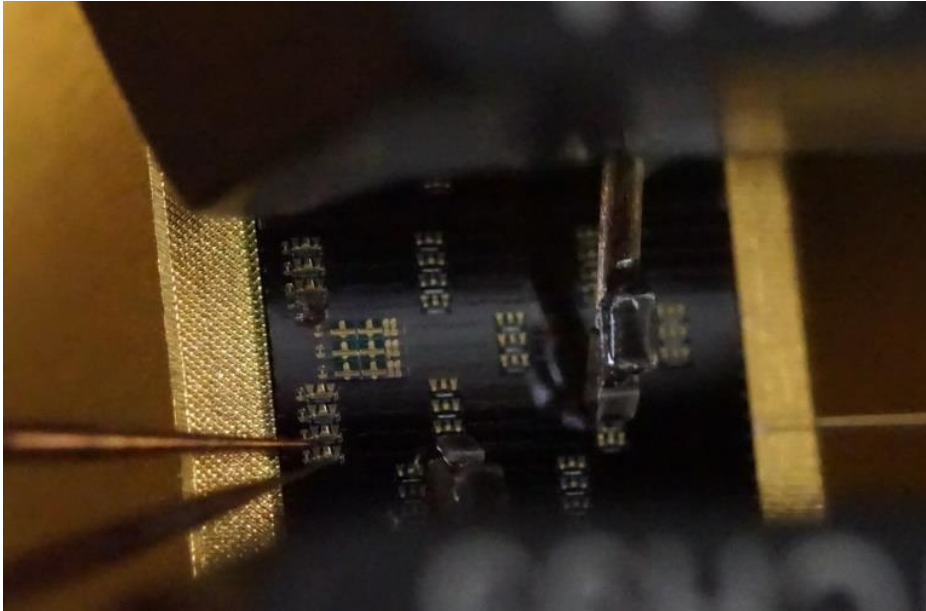


Figure 4-37. Optical photograph of a contacted bar containing DP EMLs. The DFB laser is on the left and is contacted by two probe needles. The two EAMs are contacted by GSG high-frequency probes that contain an integrated AC-coupled $50\ \Omega$ resistor. The fiber on the right for optical coupling has a tapered tip and a mode field diameter ($1/e^2$) of $3.5\ \mu\text{m}$.

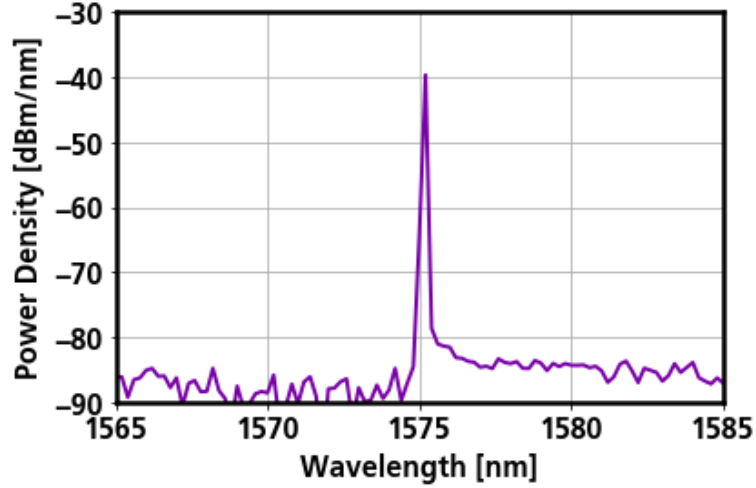


Figure 4-38. Output spectrum of the DP EML. No bias voltages are applied to the EAMs and the TEC is set to 20°C. The DFB is biased with a CW current of 95 mA. The side mode suppression ratio exceeds 45 dB.

The output SOP of the DP EML as a function of the two EAM biases is measured. Due to the 3 mm long output waveguide with non-zero birefringence, the output SOP for zero bias is arbitrary. For understanding the SOP behavior, however, the ability to measure the complete output Stokes vector becomes very powerful: we can rotate the output SOP in our model using any arbitrary retarder. For clarity, we rotate the output SOP to 45° linearly polarized light, i.e. $\vec{s}_{45^\circ} = [1 \ 0 \ 1 \ 0]^T$. The result is illustrated in figure 4-39. The strategy to find the (generally elliptical) retarder that achieves this rotation is as follows: we define a retardation vector $\hat{\vec{R}}$ using the unbiased (and normalized) output SOP \vec{s}_0 as:

$$\hat{\vec{R}} = \vec{s}_0 \times \vec{s}_{45^\circ} \quad (4.27)$$

This way, $\hat{\vec{R}}$ is orthogonal to both SOPs, so rotating around it can map one onto the other. The rotation angle R then simply is the spherical distance between \vec{s}_0 and \vec{s}_{45° :

$$R = \angle(\vec{s}_0, \vec{s}_{45^\circ}) \quad (4.28)$$

For the spherical distance see appendix D1). For the details of general elliptical retarders see A). The output SOPs at the DP EML facet as well as the rotated SOPs are shown in figure 4-39. The DFB laser is biased with 130 mA and the PIC substrate temperature is set to 20°C. Ideally, the trajectories corresponding to the two respective EAMs should go along the equator of the Poincaré sphere, but in opposite directions, i.e. towards pure TE and TM respectively. After rotation, the measurement clearly show that the two EAMs do indeed cause trajectories in opposite directions, but they have some residual movement along the s_3 -axis. This is the effect of the EAM chirp. The retarder necessary for the virtual rotation has a retardation of 75° around and axis with $\psi = 0^\circ$ and $\chi = -20^\circ$, so it is purely circular.

The dependence of TE- and TM-polarized output power after the virtual SOP rotation is shown in figure 4-40. The colormaps also include contour lines, showing that the

modulation of the two polarizations is indeed orthogonal with respect to the two EAMs. The powers in the two polarizations are obtained from the measured Stokes vectors via:

$$P_{TE} = \frac{s_0 + s_1}{2}; \quad P_{TM} = \frac{s_0 - s_1}{2} \quad (4.29)$$

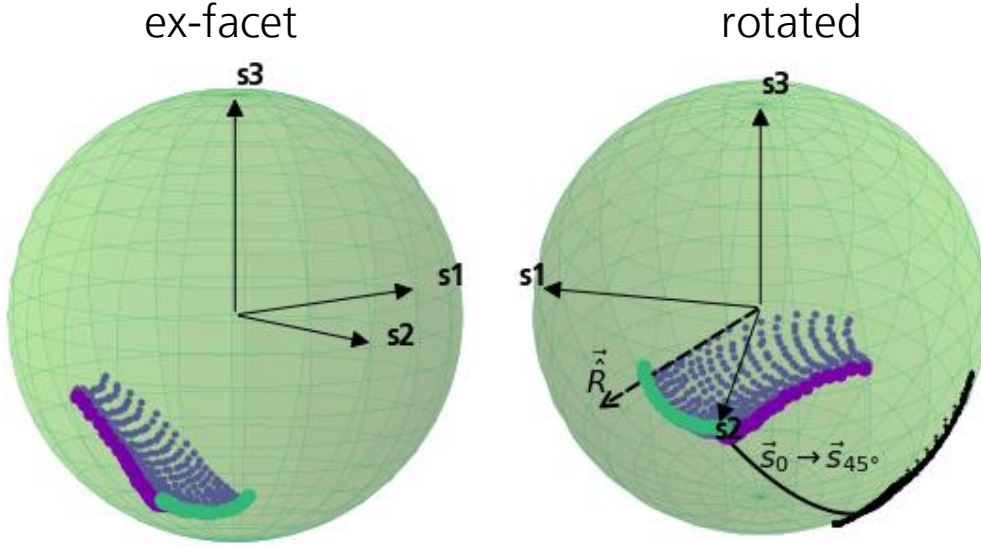


Figure 4-39. Output state of polarization (SOP) of the DP EML for different bias voltages. The laser current is 130 mA and the TEC is set to 20°C. Left: measured SOPs of the light exiting the facet. Right: SOPs rotated such that the unbiased DP EML emits 45° linearly polarized light. The rotation is done after the measurement in python, emulating a circular retarder with retardance 75°, $\psi = 0^\circ$ and $\chi = -20^\circ$. The retarder axis is indicated as \vec{R} . Green dots show the SOPs when only sweeping the first EAM, purple dots when only sweeping the second EAM. Blue dots correspond to both EAMs being biased. The EAMs bias voltages are between 0 and -5 V.

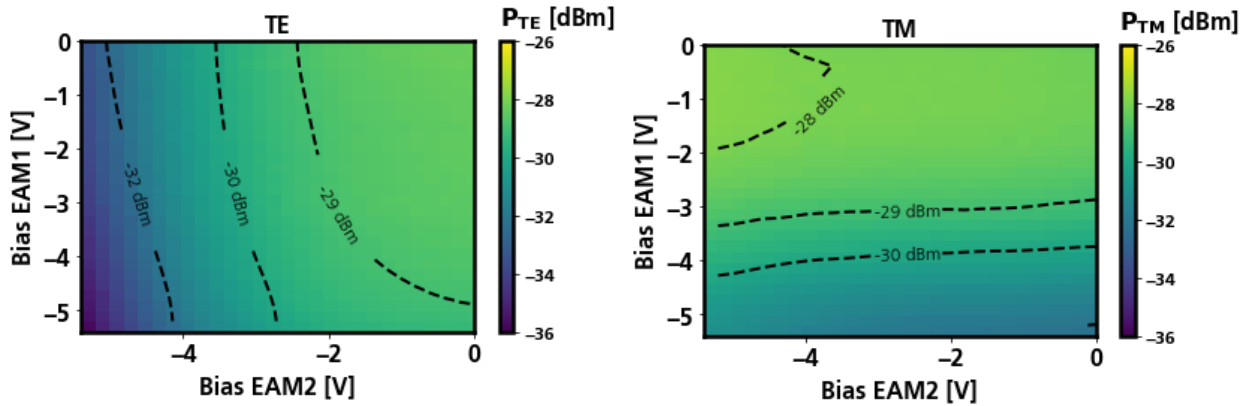


Figure 4-40. Colormaps and contour plots of the output power carried by the TE polarization (left) and TM polarization (right) versus EAM bias voltages. Ideally, the contours should be perpendicular in the two plots, corresponding to an ideal 90° PR and consequently no crosstalk between the two polarizations.

The total fiber-coupled output power of the DP EML is -25 dBm with zero bias. This can be broken down as follows: 0 dBm is emitted from one side of the DFB, experiencing 1.5 dB loss per PR on this particular wafer, 9 dB per EAM (including the two epitaxial butt-joint

interfaces) and 4 dB coupling loss to a tapered single mode fiber. The output power of future devices could be improved by 10 dB by lowering the butt-joint interface coupling loss between PR and EAM sections by 2.5 dB. Another ~5 dB could be gained by reducing the DFB series resistance to below 10 Ω and mounting the chip on a proper heat sink.

4.5.2 Large Signal Measurements

For a large signal modulation experiment, a setup as shown in figure 4-41 is used. Just like in the case of the DP EAM in the previous section, a polarization controller together with a beam splitter and two high speed photodetectors and an oscilloscope form the receiver. Two 20 Gbit/s PRBS signals of length $2^{31} - 1$ are generated and launched via the RF probes onto the two EAMs.

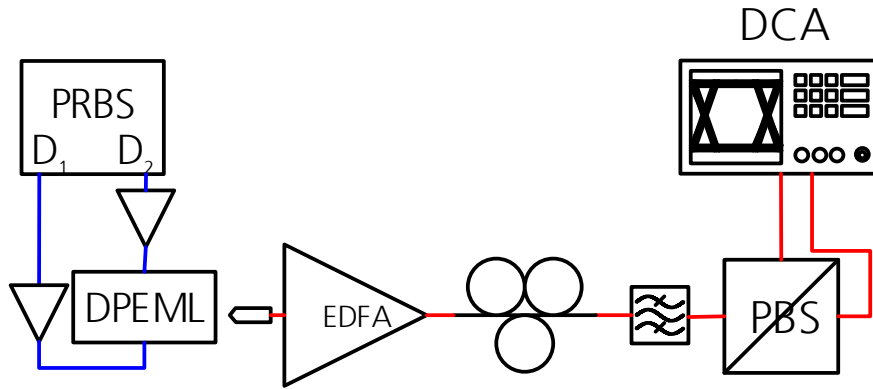


Figure 4-41. Transmission setup used for PDM-OOK. A PRBS source generates two data signals for the two respective EAMs of the DP EML. A polarization controllers (PC) is used to align the output polarization with the PBS coordinate system on the receiver side. A digital communication analyzer record the eye diagrams and dynamic extinction ratios.

For the generation of the 40 Gbit/s PDM-OOK signal, the bar substrate is set to 10°C, and the two EAMs are biased via bias-Ts at -4.6 and -4.7 V respectively. The 20 Gbit/s signals are amplified to a peak-to-peak voltage of 2 V_{pp} . The DFB current is 130 mA. The resulting eye diagrams are shown in figure 4-42. The eye corresponding to the first EAM has a strong DC fraction, limiting its dynamic ER to 2.5 dB. The ER corresponding to the second EAM is 7 dB. The DC fraction can be attributed to a sub-optimal PR in this particular device, resulting in an incomplete conversion of the light that is unmodulated in the first EAM. Due to this incomplete conversion, some part of this light does not get modulated by the second EAM either, giving rise to a DC fraction. The eye diagrams are noise limited due to the comparably low output power of the DP EML. To ensure that the two optical eyes indeed correspond to the two EAMs, respectively, we turned off one of the electrical amplifiers feeding the EAMs. As expected, one of the eye diagrams vanished with the other one remaining.

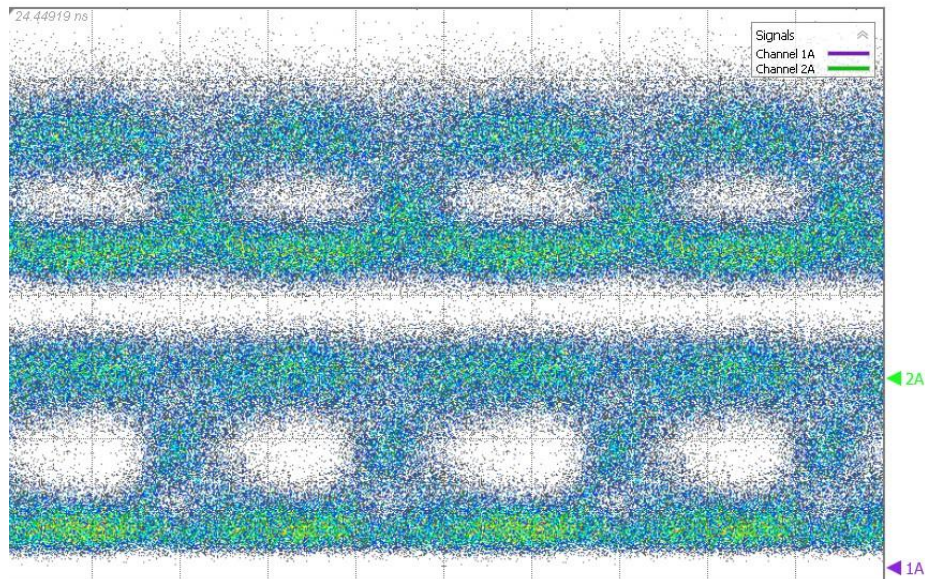


Figure 4-42. Recorded eye diagrams after 2x 20 Gbit/s modulation in the DP EML, corresponding to a total data rate of 40 Gbit/s. The upper eye diagram corresponds to the first EAM, the lower to the second. The extinction ratios (ER) are 2.5 and 7 dB, respectively. The ER of the upper eye is DC-limited. The modulated power in the fiber is -26.5 dBm.

5 Conclusion & Outlook

5.1 Conclusion

The focal point of this thesis is polarization multiplexing in photonic integrated circuits. Integrated polarization rotators are identified as the key enabler to achieve PDM functionality on both the transmit- and receive side. To this end, two major milestones are achieved in this thesis: first, bringing polarization rotators into the HHI InP photonic integration technology. Second, exploiting the PRs to implement a dual-polarization transmitter for 100 Gbit/s. With the iSTOMP, the theory for a completely new PDM/Stokes receiver is also given.

A new design methodology for PRs is developed [93] and verified. It is based on the Jones formalism and combines this formalism with modern numerical optimization techniques to achieve maximum fabrication tolerance. PRs with a conversion efficiency up to 24 dB are demonstrated experimentally. No active tuning is necessary. The conversion stays above 10 dB across the entire C-band even among different wafers. The PRs are implemented as part of HHI's generic InP photonic integration technology.

Using the PRs, a new DP EA modulator configuration is proposed and implemented, capable of error-free 100 Gbit/s PDM-PAM4 transmission [94], [95]. The DP EA modulator concept is also shown in a fully integrated DP EML PIC, integrating a DFB laser source, two PRs and two EAMs to give monolithic PDM transmitter [96]. To realize those PICs, EAMs are introduced into HHI's generic InP photonic integration technology as part of this work. Extensive calculations of the MQW-based active layer are done to feed a circuit simulator. Circuit simulations show that the PR PER should be above 15 dB for an OSNR penalty of the transmitter below 1 dB.

All newly developed components (PR, EAM, DP EAM) are now part of HHI's process design kit (PDK). They can readily be used in multi-project wafers.

With the iSTOMP, an integrated version of a classical polarimeter is presented. It provides PDM- or Stokes receiver functionality. Various ways of implementing such a device are pointed out, which can be pursued with relative ease now since the only critical part are the PRs.

Based on the Müller/Stokes formalism, a new measurement methodology is demonstrated. It enables an analysis of the newly developed devices with unprecedented detail because it goes beyond classical extinction measurements. By measuring the Müller matrix of any given device, it allows insights into a device birefringence, mode hybridization and depolarization. To the author's best knowledge, no Müller matrix measurements of PICs have been done before. The implemented measurement setup is accurate within 2° on the entire Poincaré sphere and across the whole C-band. It is also stable for more than a week.

5.2 Outlook

The design methodology used to derive the PR design optimizes the tolerance versus one parameter only, namely width deviations. As the methodology is proven, multidimensional

optimization might be done, to optimize the performance versus several parameters. These might include wavelength to make the PR more broadband. Also epitaxial deviations (thickness and material composition) can be taken into account.

Even though the presented DP EML is the first integrated PDM transmitter of its kind, several further developments can be perceived. The demonstrated design was made with the assumption that a 45° PR after the laser is the ideal component. Given the PDL along the transmitter, this might not be true, however. In this case, it might be desirable to have less or more conversion. The lasing wavelength is also not optimized yet. The results on single EAM devices indicate that a wavelength of around $1.565\text{ }\mu\text{m}$ should give better performance over the now demonstrated $1.575\text{ }\mu\text{m}$. Regarding output power, improving the butt-joint interface coupling loss from between PR and EAM sections by 2.5 dB per interface should be achievable, giving 10 dB more output power. Also improving the parasitic resistance of the active sections would improve the DFB output power, possibly giving another 5 dB when the device is properly packaged. This would also benefit the EAM frequency response. The output power could be improved even further by adding SOA sections to both EAMs. Finally, integrating an phase shifter with strong polarization dependence in the same serial fashion would allow movement along on the entire Poincaré sphere, making the device a true Stokes space transmitter and/or polarization tunable laser source. For the latter, a slow phase modulator based on carrier injection would be sufficient (see Kazi et al. in [97])

The extensive experimental analysis of the EAMs will be made available as part of HHI's PDK for external users of HHI's generic photonic technology. The frequency response of the first devices is RC-limited, mostly due to excessive p-side series resistances. Test runs showed that an optimized processing can give more than two times lower resistances. Using these optimized processes, the EAM bandwidth in future runs should reach values above 30 GHz, at least if the carrier transit times prove to be fast enough. Then, 56 GBaud signaling becomes feasible.

With the iSTOMP, a new receiver scheme is proposed that can be used together with the DP EAM to avoid coherent reception. MMIs and photodetectors are already part of HHI's PDK and the necessary PRs can be implemented following the presented methodology. Some custom MMI design might be required, however. To make use of the devices in real transmission systems, the required DSP complexity to retrieve the Stokes vector from the measured signals remains to be analyzed.

The measurement of the full Müller matrix of an integrated device can enable new insights into device characteristics even beyond what is demonstrated so far. The depolarization of devices is encapsulated in its Müller matrix, potentially giving insight into noise mechanisms such as spontaneous emission in SOAs, non-coherent scattering or nonlinear processes [98].

5.3 Acknowledgements

I would like to thank Prof. Dr. Martin Schell for allowing me to pursue the topics his young PhD student was so keen on investigating. In modern science, however, a single person

cannot achieve much on his or her own. I am especially indebted to my supervisor Dr. Francisco M. Soares. His tireless advice and technological expertise was invaluable. Special thanks go to Dr. Ute Troppenz for many fruitful discussions during late hours and thorough proof reading. I would also like to thank my group leader, Dr. Martin Moehrle, for his patience and trust, as well as for sharing the knowledge of the highly skilled and experienced expert that he is. Without Dr. Norbert Grote much of this work would have been impossible as it is based on the large number of projects he acquired for HHI. I owe thanks to the entire clean room team at HHI, whose excellence shines through in the resulting devices.

6 Appendices

A) Müller Matrix of Elliptical Diattenuators and Retarders

The most general diattenuators and retarders are elliptical. They are used in this work to accurately model the elements in the polarization controller of the experimental setup (see 4.1.1.3) and for the decomposition of measured Müller matrices (see 4.1.3). We use the same definitions as Lu and Chipman in [85].

For a given diattenuation vector of length D

$$\vec{D} = \begin{pmatrix} D_H \\ D_{45} \\ D_C \end{pmatrix} = D \begin{pmatrix} d_1 \\ d_2 \\ d_3 \end{pmatrix} \quad (6.1)$$

and the unpolarized transmission T , we can write the diattenuator Matrix as

$$\underline{M}_D = T \begin{pmatrix} 1 & \vec{D}^T \\ \vec{D} & \underline{m}_D \end{pmatrix} \quad (6.2)$$

With the 3x3 kernel:

$$\underline{m}_D = \sqrt{1 - D^2} \underline{I} + \frac{(1 - \sqrt{1 - D^2})}{D^2} \vec{D} \vec{D}^T \quad (6.3)$$

For a given retardation vector with total retardation R

$$\vec{R} = \begin{pmatrix} R_H \\ R_{45} \\ R_C \end{pmatrix} = R \begin{pmatrix} a_1 \\ a_2 \\ a_3 \end{pmatrix} = R \vec{R} \quad (6.4)$$

We can write the retarder matrix as

$$\underline{M}_R = \begin{pmatrix} 1 & \vec{0}^T \\ \vec{0} & \underline{m}_R \end{pmatrix} \quad (6.5)$$

And, with the Kronecker symbol δ and the Levi-Civita symbol ϵ :

$$[\underline{m}_R]_{ij} = \delta_{ij} \cos R + a_i a_j (1 - \cos R) + \sum_{k=1}^3 \epsilon_{ijk} a_k \sin R \quad (6.6)$$

The retardation vector \vec{R} can also be obtained from a given \underline{M}_R as follows:

$$R = \cos^{-1} \left(\frac{\text{trace}(\underline{M}_R) - 1}{2} \right) \quad (6.7)$$

$$a_i = \frac{1}{2 \sin R} \sum_{j,k=1}^3 \epsilon_{ijk} [\underline{m}_R]_{jk}$$

B) Material Models

With the values from Table 2, any parameter p of the quaternary material $\text{In}_{1-x}\text{Ga}_x\text{As}_y\text{P}_{1-y}$ can be interpolated in between the values of the four binary materials using the stoichiometric fractions (Vegard's law, [99]):

$$p(x, y) = (1 - x)(1 - y)p_{\text{InP}} + (1 - x)y p_{\text{InAs}} + x y p_{\text{GaAs}} + x(1 - y)p_{\text{GaP}} \quad (6.8)$$

The stoichiometric fractions for a desired band gap can be deduced from the condition of lattice matching to InP.

Parameter	InP	InAs	GaAs	GaP
Hydrostatic deformation potential, a [eV]	-6.16	-5.79	-8.68	-9.76
Shear deformation potential, b [eV]	-1.6	-1.8	-1.7	-1.5
Elastic stiffness coefficient, C_{11} [GPa]	1022	833	1188	1412
Pressue coefficient of E_g, C_{12} [GPa]	576	453	538	625
Lattice constant [Å]	5.8687	6.0583	5.6533	5.4505
Band gap E_g [eV]	1.35	1.42	0.36	2.74
m_e^*	$0.077m_e$	$0.021m_e$	$0.063m_e$	$0.33m_e$
m_{HH}^*	$0.56m_e$	$0.517m_e$	$0.5m_e$	$0.54m_e$
m_{LH}^*	$0.12m_e$	$0.024m_e$	$0.088m_e$	$0.16m_e$

Table 2. Material parameters of binary alloys after Li [100]. m_e is the electron rest mass, m^* denotes the effective masses of electrons and holes.

For passive waveguides (i.e. with a core band gap much larger than the photon energy), we use the refractive index model after [101]:

$$n^2 = 1 + \frac{E_d}{E_0} + \frac{E_d E}{E_0^3} + \frac{\eta E^4}{\pi} \ln \left(\frac{2E_0^2 - 2E_g^2 - E^2}{E_g^2 - E^2} \right) \quad (6.9)$$

Where E_g is the band gap and E is the photon energy. The oscillator parameters are (in eV):

$$E_0 = 0.595x^2(1 - y) + 1.626xy - 1.891y + 0.524x + 3.391 \quad (6.10)$$

$$E_d = (12.36x - 12.71)y + 7.54x + 28.91 \quad (6.11)$$

C) Simulation Parameters

Meshsize	25 nm
Wavelength	1.55 μm
Threads	16

Table 3: MODE FDE Parameters

Meshsize	25 nm
Wavelength	1.55 μm
CVCS	Yes
Number of modes	8
Threads	16

Table 4 MODE EME Parameters

Meshsize	55 nm
Mesh Refinement	3
Threads	16

Table 5 FDTD Parameters

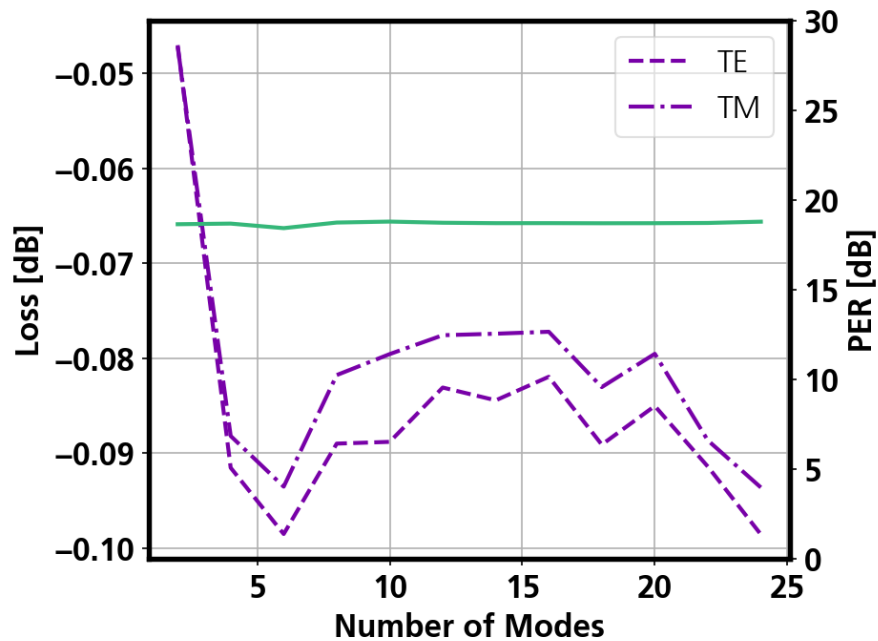


Figure 6-1. Convergence of EME simulations for tapered PR designs. The number of cells per taper should be at least 10 if one wishes to calculate proper transmission losses. The number of modes should be larger than 8 to model the loss accurately. The PER is much less sensitive.

D) Formulas

D1) Orthodromic distance

To calculate the central angle $\Delta\xi$ between two points $(2\psi_1, 2\chi_1)$ and $(2\psi_2, 2\chi_2)$ on the Poincaré sphere, we use the definition of the inner product and compute it in spherical coordinates:

$$\begin{aligned} \cos \Delta\xi &= \begin{pmatrix} \cos 2\psi_1 \cos 2\chi_1 \\ \sin 2\psi_1 \cos 2\chi_1 \\ \sin 2\chi_1 \end{pmatrix} \cdot \begin{pmatrix} \cos 2\psi_2 \cos 2\chi_2 \\ \sin 2\psi_2 \cos 2\chi_2 \\ \sin 2\chi_2 \end{pmatrix} \\ &= \cos 2\psi_1 \cos 2\chi_1 \cos 2\psi_2 \cos 2\chi_2 + \sin 2\psi_1 \cos 2\chi_1 \sin 2\psi_2 \cos 2\chi_2 + \sin 2\chi_1 \sin 2\chi_2 \\ &= \cos 2\chi_1 \cos 2\chi_2 (\cos 2\psi_1 \cos 2\psi_2 + \sin 2\psi_1 \sin 2\psi_2) + \sin 2\chi_1 \sin 2\chi_2 \\ &= \cos 2\chi_1 \cos 2\chi_2 \cos(2\psi_1 - 2\psi_2) + \sin 2\chi_1 \sin 2\chi_2 \end{aligned} \quad (6.12)$$

Consequently:

$$\Delta\xi = \arccos(\sin 2\chi_1 \sin 2\chi_2 + \cos 2\chi_1 \cos 2\chi_2 \cos(2\psi_1 - 2\psi_2)) \quad (6.13)$$

The distance d between the points along the sphere of radius r then writes as:

$$d = r\Delta\xi \quad (6.14)$$

E) Abbreviations

AC	Alternating current
DC	Direct current
DFB	Distributed feedback
DOP	Degree of polarization
DP	Dual polarization
DP EML	Dual-polarization externally modulated laser
DUT	Device under test
EAM	Electro-absorption modulator
iSTOMP	Integrates Stokes mapper
LCA	Lightwave component analyzer
MQW	Multi quantum well
NRZ	Non return to zero
OOK	On-off keying
PAM-4	Quaternary pulse amplitude modulation
PBS	Polarization beam splitter
PC	Polarization controller
PDM	Polarization division multiplexing
PR	Polarization rotator
QAM	Quadrature-amplitude modulation
QCSE	Quantum-confined Stark effect
SCR	Space charge region
SMSR	Side mode suppression ratio
SOP	State of polarization
TEC	Temperature controller

7 Published Work

Parts of this work have already been published:

M. Baier et al., "Highly fabrication tolerant polarization converter for generic photonic integration technology," in 2016 Compound Semiconductor Week (CSW) [Includes 28th International Conference on Indium Phosphide Related Materials (IPRM) 43rd International Symposium on Compound Semiconductors (ISCS), 2016, pp. 1–2.

Moritz Baier, Francisco M. Soares, Martin Moehrle, Norbert Grote, and Martin Schell, "A New Approach to Designing Polarization Rotating Waveguides," presented at the European Conference on Integrated Optics 2016, Warsaw, 2016.

M. Baier et al., "112-Gb/s PDM-PAM4 Generation and 80-km Transmission Using a Novel Monolithically Integrated Dual-Polarization Electro-Absorption Modulator InP PIC," in Proc. 43rd European Conference on Optical Communication (ECOC), 2017, p. Th.1.C.3.

M. Baier et al., "Fully Integrated Serial Dual-Polarization Electro-absorption Modulator PIC in InP", in Proceedings of the 19th European Conference on Integrated Optics, 2017.

M. Baier et al., "64 Gbit/s Generation from a Fully Integrated Serial 0.25 x 2.0 mm² Dual-Polarization Electroabsorption Modulator PIC in InP," presented at the Compound Semiconductor Week 2017, Berlin, 2017, vol. C1.2.

M. Baier und F. Soares, „Verfahren zum Herstellen eines Polarisationskonverters, Polarisationskonverter und Polarisationskonverterelement“, Patent DE102016202634A1, 24-Aug-2017.

M. Baier, F. M. Soares, T. Gaertner, A. Schoenau, M. Moehrle, and M. Schell, "New Polarization Multiplexed Externally Modulated Laser PIC," in 2018 European Conference on Optical Communication (ECOC), 2018, pp. 1–3.

M. Baier, F. M. Soares, T. Gaertner, M. Moehrle, and M. Schell, "Fabrication Tolerant Integrated Polarization Rotator Design Using the Jones Calculus," J. Light. Technol., May 2018.

M. Baier, F. Soares, und M. Schell, „Modulatoranordnung und Verfahren zum Modulieren von Licht“, Patent DE102016224615, 14-Juni-2018.

Bibliography

- [1] J. Bardeen and W. H. Brattain, "The Transistor, A Semi-Conductor Triode," *Phys. Rev.*, vol. 74, no. 2, pp. 230–231, Jul. 1948.
- [2] T. H. Maiman, "Stimulated Optical Radiation in Ruby," *Nature*, vol. 187, no. 4736, p. 493, Aug. 1960.
- [3] "Inside Volta: The World's Most Advanced Data Center GPU," *Parallel Forall*, 10-May-2017. [Online]. Available: <https://devblogs.nvidia.com/parallelforall/inside-volta/>. [Accessed: 05-Jan-2018].

- [4] G. E. Moore, "Cramming more components onto integrated circuits, Reprinted from Electronics, volume 38, number 8, April 19, 1965, pp.114 ff.," *IEEE Solid-State Circuits Soc. Newsl.*, vol. 11, no. 3, pp. 33–35, Sep. 2006.
- [5] "The Zettabyte Era: Trends and Analysis," *Cisco*. [Online]. Available: <https://www.cisco.com/c/en/us/solutions/collateral/service-provider/visual-networking-index-vni/vni-hyperconnectivity-wp.html>. [Accessed: 05-Jan-2018].
- [6] M. Smit, J. van der Tol, and M. Hill, "Moore's law in photonics," *Laser Photonics Rev.*, vol. 6, no. 1, pp. 1–13, Jan. 2012.
- [7] P. J. Winzer, "Making spatial multiplexing a reality," *Nature Photonics*, 25-Apr-2014. [Online]. Available: <https://www.nature.com/articles/nphoton.2014.58>. [Accessed: 02-Mar-2018].
- [8] P. J. Winzer, "Modulation and multiplexing in optical communications," in *2009 Conference on Lasers and Electro-Optics and 2009 Conference on Quantum electronics and Laser Science Conference*, 2009, pp. 1–2.
- [9] M. Theurer, G. Przyrembel, A. Sigmund, W.-D. Molzow, U. Troppenz, and M. Möhrle, "56 Gb/s L-band InGaAlAs ridge waveguide electroabsorption modulated laser with integrated SOA," *Phys. Status Solidi A*, vol. 213, no. 4, pp. 970–974, Apr. 2016.
- [10] N. K. Fontaine *et al.*, "30x30 MIMO transmission over 15 spatial modes," in *2015 Optical Fiber Communications Conference and Exhibition (OFC)*, 2015, pp. 1–3.
- [11] M. Lauermann *et al.*, "Multi-channel, widely-tunable coherent transmitter and receiver PICs operating at 88Gbaud/16-QAM," in *2017 Optical Fiber Communications Conference and Exhibition (OFC)*, 2017, pp. 1–3.
- [12] S. C. Heck *et al.*, "Miniaturized InP dual I amp;Q mach Zehnder modulator with full monitoring functionality for CFP2," in *2014 The European Conference on Optical Communication (ECOC)*, 2014, pp. 1–3.
- [13] Y. Ueda, Y. Ogiso, and N. Kikuchi, "InP PIC technologies for high-performance Mach-Zehnder modulator," 2017, vol. 10129, pp. 1012905-1012905–7.
- [14] D. Taillaert, H. Chong, P. I. Borel, L. H. Frandsen, R. M. D. L. Rue, and R. Baets, "A compact two-dimensional grating coupler used as a polarization splitter," *IEEE Photonics Technol. Lett.*, vol. 15, no. 9, pp. 1249–1251, Sep. 2003.
- [15] F. V. Laere, W. Bogaerts, P. Dumon, G. Roelkens, D. V. Thourhout, and R. Baets, "Focusing Polarization Diversity Grating Couplers in Silicon-on-Insulator," *J. Light. Technol.*, vol. 27, no. 5, pp. 612–618, Mar. 2009.
- [16] S. P. Anderson and M. Webster, "Silicon Photonic Polarization-Multiplexing Nanotaper for Chip-to-Fiber Coupling," *J. Light. Technol.*, vol. 34, no. 2, pp. 372–378, Jan. 2016.
- [17] F. Kish *et al.*, "System-on-Chip Photonic Integrated Circuits," *IEEE J. Sel. Top. Quantum Electron.*, vol. 24, no. 1, pp. 1–20, Jan. 2018.
- [18] R. Kaiser *et al.*, "Monolithically integrated polarisation diversity heterodyne receivers on GaInAsP/InP," *Electron. Lett.*, vol. 30, no. 17, pp. 1446–1447, 1994.
- [19] T. Brast *et al.*, "Monolithic 100 Gb/s twin-IQ Mach-Zehnder modulators for advanced hybrid high-capacity transmitter boards," in *2011 Optical Fiber Communication Conference and Exposition and the National Fiber Optic Engineers Conference*, 2011, pp. 1–3.
- [20] J. Estarán *et al.*, "Quaternary Polarization-Multiplexed Subsystem for High-Capacity IM/DD Optical Data Links," *J. Light. Technol.*, vol. 33, no. 7, pp. 1408–1416, Apr. 2015.
- [21] D. Plant, "Optical Communications Systems for Data Center Networking," in *Optical Fiber Communication Conference (2017)*, paper W3B.1, 2017, p. W3B.1.

- [22] M. Chagnon and D. Plant, "504 and 462 Gb/s Direct Detect Transceiver for Single Carrier Short-Reach Data Center Applications," in *Optical Fiber Communication Conference (2017)*, paper W3B.2, 2017, p. W3B.2.
- [23] M. Morsy-Osman, M. Chagnon, and D. V. Plant, "Polarization division multiplexed intensity, inter polarization phase and inter polarization differential phase modulation with stokes space direct detection for 1 #x03BB; #x00D7;320 Gb/s 10 km transmission at 8 bits/symbol," in *2015 European Conference on Optical Communication (ECOC)*, 2015, pp. 1–7.
- [24] D. Che, A. Li, X. Chen, Q. Hu, Y. Wang, and W. Shieh, "160-Gb/s stokes vector direct detection for short reach optical communication," in *OFC 2014*, 2014, pp. 1–3.
- [25] W. Shieh, H. Khodakarami, and D. Che, "Invited Article: Polarization diversity and modulation for high-speed optical communications: architectures and capacity," *APL Photonics*, vol. 1, no. 4, p. 040801, Jul. 2016.
- [26] M. Bass, C. Decusatis, and J. Enoch, *Handbook of Optics, Third Edition Volume I: Geometrical and Physical Optics, Polarized Light, Components and Instruments(set)*, Revised. New York: Mcgraw Hill Book Co, 2009.
- [27] F. Zernike and J. E. Midwinter, *Applied nonlinear optics*. Wiley, 1973.
- [28] R. P. Feynman, R. B. Leighton, and M. L. Sands, *The Feynman Lectures on Physics*. Addison-Wesley, 1963.
- [29] "Wiley: Polarization of Light - Serge Huard." [Online]. Available: <http://www.wiley.com/WileyCDA/WileyTitle/productCd-0471965367.html>. [Accessed: 26-Jun-2017].
- [30] R. C. Jones, "A New Calculus for the Treatment of Optical SystemsI. Description and Discussion of the Calculus," *JOSA*, vol. 31, no. 7, pp. 488–493, Jul. 1941.
- [31] A. Gerrard and J. M. Burch, *Introduction to Matrix Methods in Optics*. Courier Corporation, 1975.
- [32] R. M. A. Azzam and N. M. Bashara?, *Ellipsometry and Polarized Light*, 3rd reprint 1999 edition. Amsterdam: North Holland, 1988.
- [33] W. Glaser, *Photonik für Ingenieure*. Berlin: Huss-Medien, 1997.
- [34] G. G. Stokes, "On the Composition and Resolution of Streams of Polarized Light from different Sources," *Trans. Camb. Philos. Soc.*, vol. 9, p. 399, 1851.
- [35] R. C. Jones, "A New Calculus for the Treatment of Optical SystemsV. A More General Formulation, and Description of Another Calculus," *JOSA*, vol. 37, no. 2, pp. 107–110, Feb. 1947.
- [36] H. Poincaré, M. Lamotte, and D. Hurmuzescu, *Théorie mathématique de la lumière II. Nouvelles études sur la diffraction.--Théorie de la dispersion de Helmholtz. Leçons professées pendant le premier semestre 1891-1892*. Paris, G. Carré, 1892.
- [37] R. P. Feynman, F. L. Vernon, and R. W. Hellwarth, "Geometrical Representation of the Schrödinger Equation for Solving Maser Problems," *J. Appl. Phys.*, vol. 28, no. 1, pp. 49–52, Jan. 1957.
- [38] M. A. Nielsen and I. L. Chuang, *Quantum Computation and Quantum Information*. Cambridge: Cambridge University Press, 2000.
- [39] H. Müller, "Memorandum on the polarization optics of the photo-elastic shutter," Nov. 1943.
- [40] P. Soleillet, "Sur les paramètres caractérisant la polarisation partielle de la lumière dans les phénomènes de fluorescence," *Ann. Phys.*, vol. 10, no. 12, pp. 23–97, 1929.

- [41] “Lumerical Inc. | Innovative Photonic Design Tools.” [Online]. Available: <https://www.lumerical.com/>. [Accessed: 12-Jan-2018].
- [42] “Wiley: Physics of Photonic Devices, 2nd Edition - Shun Lien Chuang.” [Online]. Available: <http://www.wiley.com/WileyCDA/WileyTitle/productCd-0470293195.html>. [Accessed: 11-Sep-2017].
- [43] “Optical Waveguide Theory | A.W. Snyder | Springer.” [Online]. Available: <http://www.springer.com/de/book/9780412099502>. [Accessed: 12-Jan-2018].
- [44] L. A. Coldren, S. W. Corzine, and M. L. Mashanovitch, *Diode Lasers and Photonic Integrated Circuits*, 2 edition. Hoboken, N.J: Wiley, 2012.
- [45] D. O. Dzibrou, J. J. G. M. van der Tol, and M. K. Smit, “Tolerant polarization converter for InGaAsP-InP photonic integrated circuits,” *Opt. Lett.*, vol. 38, no. 18, pp. 3482–3484, Sep. 2013.
- [46] D. O. Dzibrou, J. J. G. M. van der Tol, and M. K. Smit, “Improved fabrication process of low-loss and efficient polarization converters in InP-based photonic integrated circuits,” *Opt. Lett.*, vol. 38, no. 7, p. 1061, Apr. 2013.
- [47] D. T. J. J. G. Van, “Increased tolerance polarization converters,” WO2013083493 A1, 13-Jun-2013.
- [48] “Welcome to Python.org,” *Python.org*. [Online]. Available: <https://www.python.org/>. [Accessed: 12-Jan-2018].
- [49] “SciPy.org — SciPy.org.” [Online]. Available: <https://www.scipy.org/>. [Accessed: 12-Jan-2018].
- [50] J. A. Nelder and R. Mead, *A Simplex Method for Function Minimization Comput*, vol. 7. 1965.
- [51] Augustin, L.M., “Polarization handling in photonic integrated circuits,” Technical University of Eindhoven, Eindhoven, 2008.
- [52] M. R. Paiam and R. I. MacDonald, “Design of phased-array wavelength division multiplexers using multimode interference couplers,” *Appl. Opt.*, vol. 36, no. 21, pp. 5097–5108, Jul. 1997.
- [53] M. Berger, *Geometry I*. Springer Science & Business Media, 2009.
- [54] M. Moehrle *et al.*, “InGaAlAs RW-based electro-absorption-modulated DFB-lasers for high-speed applications,” *Semicond. Lasers Laser Dyn. Vi*, vol. 9134, p. 913419, 2014.
- [55] S. L. Chuang, “Efficient band-structure calculations of strained quantum wells,” *Phys. Rev. B*, vol. 43, no. 12, pp. 9649–9661, 1991.
- [56] N. V. Kudryavtseva, “Effect of deformation on the electronic energy spectrum in crystals,” *Sov. Phys. J.*, vol. 15, no. 12, pp. 1740–1742, Dec. 1972.
- [57] H. Asai and K. Oe, “Energy band-gap shift with elastic strain in $GaxIn_{1-x}P$ epitaxial layers on (001) GaAs substrates,” *J. Appl. Phys.*, vol. 54, no. 4, pp. 2052–2056, Apr. 1983.
- [58] J. C. Yi and N. Dagli, “Finite-element analysis of valence band structure and optical properties of quantum-wire arrays on vicinal substrates,” *IEEE J. Quantum Electron.*, vol. 31, no. 2, pp. 208–218, Feb. 1995.
- [59] R. de L. Kronig, “On the Theory of Dispersion of X-Rays,” *JOSA*, vol. 12, no. 6, pp. 547–557, Jun. 1926.
- [60] H. A. Kramers, “La diffusion de la lumière par les atomes,” *Atti Congr. Internazionale Dei Fis.*, vol. Como-Pavia-Roma Vol. 2, pp. 545–57.
- [61] D. C. Hutchings, M. Sheik-Bahae, D. J. Hagan, and E. W. V. Stryland, “Kramers-Krönig relations in nonlinear optics,” *Opt. Quantum Electron.*, vol. 24, no. 1, pp. 1–30, Jan. 1992.

- [62] J. Singh, *Electronic and Optoelectronic Properties of Semiconductor Structures*. Cambridge University Press, 2007.
- [63] C. Tanguy, "Refractive index of direct bandgap semiconductors near the absorption threshold: influence of excitonic effects," *IEEE J. Quantum Electron.*, vol. 32, no. 10, pp. 1746–1751, Oct. 1996.
- [64] S. Seifert and P. Runge, "Refractive index of $\text{In}_{1-x}\text{Ga}_x\text{As}_y\text{P}_{1-y}$ lattice-matched to InP in IR-transparent and absorption region," in *26th International Conference on Indium Phosphide and Related Materials (IPRM)*, 2014, pp. 1–2.
- [65] J. P. van der Ziel, M. Ilegems, and R. M. Mikulyak, "Optical birefringence of thin GaAs-AlAs multilayer films," *Appl. Phys. Lett.*, vol. 28, no. 12, pp. 735–737, Jun. 1976.
- [66] T. H. Wood *et al.*, "High-Speed Optical Modulation with GaAs/GaAlAs Quantum Wells in a p-i-n Diode Structure," *Phys. Rev. Lett.*, vol. 44, pp. 16–18, 1984.
- [67] D. A. B. Miller *et al.*, "Band-Edge Electroabsorption in Quantum Well Structures: The Quantum-Confined Stark Effect," *Phys. Rev. Lett.*, vol. 53, no. 22, pp. 2173–2176, Nov. 1984.
- [68] G. Bastard, E. E. Mendez, L. L. Chang, and L. Esaki, "Variational calculations on a quantum well in an electric field," *Phys. Rev. B*, vol. 28, no. 6, pp. 3241–3245, Sep. 1983.
- [69] T. Hiroshima and R. Lang, "Well size dependence of Stark shifts for heavy-hole and light-hole levels in GaAs/AlGaAs quantum wells," *Appl. Phys. Lett.*, vol. 49, no. 11, pp. 639–641, Sep. 1986.
- [70] *Fibre Optic Communication - Key Devices | Herbert Venghaus | Springer*. .
- [71] H. Klein, "Integrated InP Mach-Zehnder Modulators for 100 Gbit/s Ethernet Applications using QPSK Modulation," Oct. 2010.
- [72] D. A. B. Miller *et al.*, "Electric field dependence of optical absorption near the band gap of quantum-well structures," *Phys. Rev. B*, vol. 32, no. 2, pp. 1043–1060, Jul. 1985.
- [73] A. Majumder, B. Shen, R. Polson, and R. Menon, "Ultra-compact polarization rotation in integrated silicon photonics using digital metamaterials," *Opt. Express*, vol. 25, no. 17, pp. 19721–19731, Aug. 2017.
- [74] M. A. Naeem, M. Haji, B. M. Holmes, D. C. Hutchings, J. H. Marsh, and A. E. Kelly, "Generation of High Speed Polarization Modulated Data Using a Monolithically Integrated Device," *IEEE J. Sel. Top. Quantum Electron.*, vol. 21, no. 4, pp. 207–211, Jul. 2015.
- [75] D. O. Dzibrou, "Building blocks for control of polarization in photonic integrated circuits / Dzmity O. Dzibrou," Technische Universiteit Eindhoven, Eindhoven, 2014.
- [76] R. M. Craig, S. L. Gilbert, and P. D. Hale, "High-resolution, nonmechanical approach to polarization-dependent transmission measurements," *J. Light. Technol.*, vol. 16, no. 7, pp. 1285–1294, Jul. 1998.
- [77] R. M. Craig, "Accurate spectral characterization of polarization-dependent loss," *J. Light. Technol.*, vol. 21, no. 2, pp. 432–437, Feb. 2003.
- [78] G. D. VanWiggeren, A. R. Motamedi, and D. M. Barley, "Single-scan interferometric component analyzer," *IEEE Photonics Technol. Lett.*, vol. 15, no. 2, pp. 263–265, Feb. 2003.
- [79] D. K. Gifford, B. J. Soller, M. S. Wolfe, and M. E. Froggatt, "Optical vector network analyzer for single-scan measurements of loss, group delay, and polarization mode dispersion," *Appl. Opt.*, vol. 44, no. 34, pp. 7282–7286, Dec. 2005.
- [80] N. K. Fontaine, "Characterization of space-division multiplexing fibers using swept-wavelength interferometry," in *2015 Optical Fiber Communications Conference and Exhibition (OFC)*, 2015, pp. 1–3.

- [81] H. Dong *et al.*, “Measurement of Mueller matrix for an optical fiber system with birefringence and polarization-dependent loss or gain,” *Opt. Commun.*, vol. 274, no. 1, pp. 116–123, Jun. 2007.
- [82] N. G. Walker and G. R. Walker, “Polarization control for coherent communications,” *J. Light. Technol.*, vol. 8, no. 3, pp. 438–458, Mar. 1990.
- [83] N. G. Walker and G. R. Walker, “Fibre-loop polarisation controllers,” *Br. Telecom TE Memo*, vol. TA5/008/87.
- [84] R. M. A. Azzam, “Photopolarimetric measurement of the Mueller matrix by Fourier analysis of a single detected signal,” *Opt. Lett.*, vol. 2, no. 6, pp. 148–150, Jun. 1978.
- [85] S.-Y. Lu and R. A. Chipman, “Interpretation of Mueller matrices based on polar decomposition,” *JOSA A*, vol. 13, no. 5, pp. 1106–1113, May 1996.
- [86] F. Boulvert, G. Le Brun, B. Le Jeune, J. Cariou, and L. Martin, “Decomposition algorithm of an experimental Mueller matrix,” *Opt. Commun.*, vol. 282, no. 5, pp. 692–704, Mar. 2009.
- [87] D. G. M. Anderson and R. Barakat, “Necessary and sufficient conditions for a Mueller matrix to be derivable from a Jones matrix,” *JOSA A*, vol. 11, no. 8, pp. 2305–2319, Aug. 1994.
- [88] J. Gil and E. Bernabeu, “Obtainment of the polarizing and retardation parameters of a non-depolarizing optical system from the polar decomposition of its Mueller matrix,” *Optik*, vol. 76, p. 67, Jan. 1987.
- [89] Z.-F. Xing, “On the Deterministic and Non-deterministic Mueller Matrix,” *J. Mod. Opt.*, vol. 39, no. 3, pp. 461–484, Mar. 1992.
- [90] “Welcome to Bokeh — Bokeh 0.12.13 documentation.” [Online]. Available: <https://bokeh.pydata.org/en/latest/>. [Accessed: 17-Jan-2018].
- [91] R. Elschner *et al.*, “Experimental demonstration of a format-flexible single-carrier coherent receiver using data-aided digital signal processing,” *Opt. Express*, vol. 20, no. 27, pp. 28786–28791, Dec. 2012.
- [92] “G.975.1 : Forward error correction for high bit-rate DWDM submarine systems.” [Online]. Available: <https://www.itu.int/rec/T-REC-G.975.1-200402-I/en>. [Accessed: 18-Jan-2018].
- [93] M. Baier and F. Soares, “Verfahren zum Herstellen eines Polarisationskonverters, Polarisationskonverter und Polarisationskonverterelement,” DE102016202634A1, 24-Aug-2017.
- [94] M. Baier, F. Soares, and M. Schell, “Modulatoranordnung und Verfahren zum Modulieren von Licht,” DE102016224615, 14-Jun-2018.
- [95] M. Baier *et al.*, “112-Gb/s PDM-PAM4 Generation and 80-km Transmission Using a Novel Monolithically Integrated Dual-Polarization Electro-Absorption Modulator InP PIC,” in *Proc. 43rd European Conference on Optical Communication (ECOC)*, 2017, p. Th.1.C.3.
- [95] M. Baier, F. M. Soares, T. Gaertner, A. Schoenau, M. Moehrle, and M. Schell, “New Polarization Multiplexed Externally Modulated Laser PIC,” submitted to *2018 European Conference on Optical Communication (ECOC)*, 2018
- [97] M. Kazi *et al.*, “High-Speed Carrier-Injection-Based Polarization Controller With InGaAlAs/InAlAs Multiple-Quantum Wells,” *IEEE Photonics Technol. Lett.*, vol. 29, no. 22, pp. 1951–1954, Nov. 2017.

- [98] M. Winter, C. A. Bunge, D. Setti, and K. Petermann, "A Statistical Treatment of Cross-Polarization Modulation in DWDM Systems," *J. Light. Technol.*, vol. 27, no. 17, pp. 3739–3751, Sep. 2009.
- [99] L. Vegard, "Die Konstitution der Mischkristalle und die Raumfüllung der Atome," *Z. Für Phys.*, vol. 5, no. 1, pp. 17–26, Jan. 1921.
- [100] E. H. Li, "Material parameters of InGaAsP and InAlGaAs systems for use in quantum well structures at low and room temperatures," *Phys. E Low-Dimens. Syst. Nanostructures*, vol. 5, no. 4, pp. 215–273, Mar. 2000.
- [101] B. Broberg and S. Lindgren, "Refractive index of $\text{In}_{1-x}\text{Ga}_x\text{As}_y\text{P}_{1-y}$ layers and InP in the transparent wavelength region," *J. Appl. Phys.*, vol. 55, no. 9, pp. 3376–3381, May 1984.